

HIGH TORSION EFFECTS ON FLUID FLOW IN A HELICAL PIPE

M.M. Alam^{*}, M. A. Masud and K. Yamamoto^a

Mathematics Discipline, Khulna University, Khulna-9208, Bangladesh

^aDepartment of Mechanical Engineering, Okayama University, Okayama, Japan

e-mail: alam_mahmud2000@yahoo.com

ABSTRACT

The incompressible viscous steady fluid flow through a helical pipe of circular cross-section rotating at a constant angular velocity about the center of curvature is investigated numerically to examine the combined effects of rotation (Coriolis force), torsion and curvature (centrifugal force) on the flow. The flow depends on the Taylor number $T_r = \frac{2a^2\Omega_T}{\nu} \sqrt{\frac{2}{\delta + 2\beta_0^2}}$, the Dean number $D_n = \frac{\sqrt{2\delta}a^3G}{\mu\nu}$, the torsion parameter $\beta_0 = \frac{\lambda}{\sqrt{2\delta}}$ and the dimensionless curvature of the duct δ , where a is the radius of the helical pipe, Ω_T the angular velocity, μ the viscosity, ν the kinematic viscosity, G the constant pressure gradient along the pipe axis and β_0 a parameter related to the torsion τ and curvature δ . The calculations are carried out for $-1000 \leq T_r \leq 1000$, $0 \leq \beta_0 \leq 1.2$ and $\delta = 0.01, 0.2$. The total fluid flow (flux) through the pipe has a peak at a negative T_r and bifurcation solution has been obtained for $\beta_0 = 0$.

Keywords: Helical pipe, Taylor number, Curvature, Torsion, Dean number.

1. INTRODUCTION

The flow through a helical pipe has attracted considerable attention not only because of its practical importance in chemical and mechanical engineering, but also because of the physically interesting features under the effect of curvature and torsion. Dean [1] was the pioneer to develop a mathematical model for the flow through a curved pipe under the fully developed flow conditions. Secondary flow consisting of pair of counter rotating vortices caused by centrifugal force have been found. The fluid flowing through a tube rotating at a constant angular velocity about an axis normal to a plane including the tube is subject to both Coriolis and Centrifugal forces. Such rotating passages are used in cooling systems for conductors of electric generators. Miyazaki [2] examined the solutions when the pressure-driven flow is in the same direction of rotation. This is called the co-rotating case. Ito and Motai [3] investigated both co-rotating and counter rotating cases with respect to the direction of pressure-driven flow. Daskopoulos and Lenhoff [4] showed the bifurcation study of the flow with curvature and rotation. The above mentioned works have been considered for a circular cross-section.

The curved geometry of helical pipe is important from both industrial and academic standpoint. The shape of a helical pipe, as shown in fig. 1(a), is determined by the dimensionless curvature δ and torsion λ . The torsion and curvature are defined, respectively, as $\lambda = \frac{ab'}{b'^2 + c'^2}$ and $\delta = \frac{ac'}{b'^2 + c'^2}$, where a is the radius of the cross section of the helical pipe, $2\pi b'$, the pitch of the helical pipe, and

^{*}Corresponding author.

c' , the radius of the helix of the center-line of the helical pipe. The curvature δ and the torsion λ of the helical pipe characterize the particular kind of a pipe. For example, for a toroidal pipe, δ is constant and λ is zero, and for helical pipe, both λ and δ are constant and nonzero. The torsion gives rise to the so-called pitch of the pipe, $2\pi b'$, as shown in fig. 1(a). Wang [5] for the first time handled the problem of flow in a helical pipe with circular cross-section using a non-orthogonal helical co-ordinate system. The flow in the helical pipe has been studied for circular (Manlapaz *et al.* [6]; Germano [7]; Chen and Fan [8]; Tuttle [9]) cross-sections for small curvature and torsion. Yamamoto *et al.* [10] investigated numerically the flow through a helical pipe for a wide range of the Dean number and small curvature as well as torsion. They employed the orthogonal coordinate system and solved the equations numerically by applying the spectral method. K.Yamamoto, M. M. Alam, Yasuhara and Arivowo [11] studied the helical pipe flow with rotation for a small range of Dean number. For high Dean number and a wide range of torsion, no work regarding the helical pipe flow with rotation has been done. In this respect, it is quite innovative to investigate the flow in a rotating helical pipe for a wide range of torsion to understand the flow behavior. This is the main objective of the paper.

2. GOVERNING EQUATIONS

The coordinate system (s', r', θ') as shown in fig. 1(b) has been considered for fully developed flow in a rotating helical circular pipe. Here, s' is the coordinate along the center-line of the duct, \mathbf{T} the unit tangent vector along s' , and \mathbf{N} and \mathbf{B} the normal and binormal vectors, respectively. The right-handed helix is considered in our work (see fig. 1(a)). The angle ϕ is defined by

$$\phi(s') = \int_{s'_0}^{s'} \tau'(s) ds, \quad (1)$$

where, τ' is the torsion of the center-line of the pipe and s'_0 is arbitrary as long as $s' \geq s'_0$. Variables are non-dimensionalised by using a the radius of the circular tube, ν the kinematic viscosity and ρ the density of the fluid. The non-dimensional variables are defined as:

$$r = \frac{r'}{a}, \quad u = \frac{a}{\nu} u', \quad v = \frac{a}{\nu} v', \quad w = \frac{a}{\nu} w' \sqrt{2\delta}, \quad \delta = \frac{a}{L}, \quad \lambda = a\tau', \quad p = \left(\frac{a}{\nu}\right)^2 \frac{p'}{\rho}, \quad s = \frac{s'}{a} \quad (2)$$

Here u, v and w are the velocity components in the r, α, s directions respectively, p is the pressure, δ the non-dimensional curvature, λ the non-dimensional torsion and the variables with

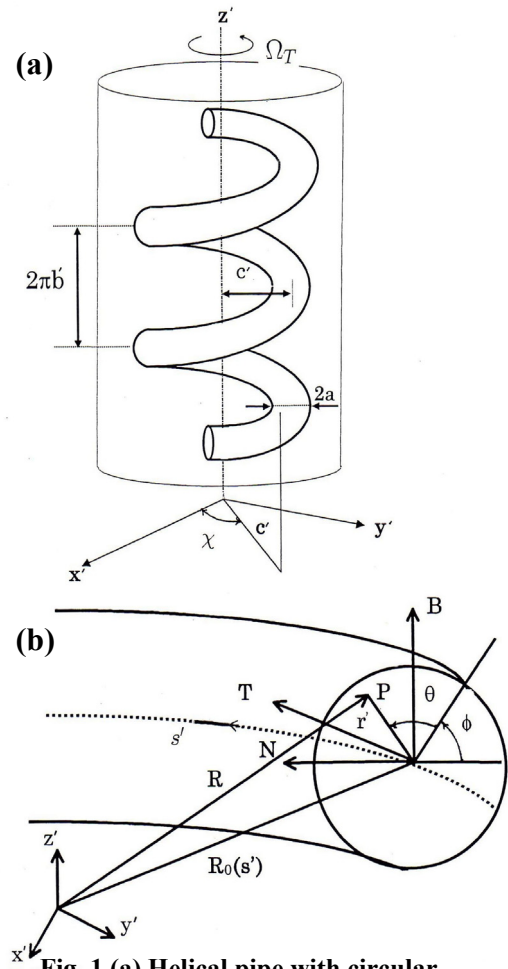


Fig. 1 (a) Helical pipe with circular cross-section and (b) Coordinate

prime are the dimensional quantities. With reference to the generalized equations, the Navier Stokes equations can be put mathematically in the following non-dimensional forms:

$$\frac{1}{r} \frac{\partial}{\partial r} (ru) + \frac{1}{r} \frac{\partial v}{\partial \alpha} + \frac{\beta_0}{\omega} \frac{\partial w}{\partial \alpha} + \frac{\delta}{\omega} (u \cos \alpha - v \sin \alpha) = 0 \quad (3)$$

$$Du - \frac{v^2}{r} - \frac{\cos \alpha}{\omega} \frac{w^2}{2} + \frac{1}{2} T_r (2\beta_0 v - w \cos \alpha) = -\frac{\partial p_1}{\partial r} - \left(\frac{1}{r} \frac{\partial}{\partial \alpha} - \frac{\delta \sin \alpha}{\omega} \right) \Omega + \frac{\beta_0}{\omega} \frac{\partial}{\partial \alpha} \left(\frac{2\delta\beta_0}{\omega} \frac{\partial u}{\partial \alpha} - \frac{\partial w}{\partial r} - \frac{\delta \cos \alpha}{\omega} w \right) \quad (4)$$

$$Dv + \frac{uv}{r} + \frac{\sin \alpha}{\omega} \frac{w^2}{2} + \frac{1}{2} T_r (w \sin \alpha - 2\beta_0 u) = -\frac{1}{r} \frac{\partial p_1}{\partial \alpha} + \left(\frac{\partial}{\partial r} + \frac{\delta \cos \alpha}{\omega} \right) \Omega + \frac{\beta_0}{\omega} \frac{\partial}{\partial \alpha} \left(\frac{2\delta\beta_0}{\omega} \frac{\partial v}{\partial \alpha} - \frac{1}{r} \frac{\partial w}{\partial \alpha} + \frac{\delta \sin \alpha}{\omega} w \right) \quad (5)$$

$$Dw + \frac{\delta \cos \alpha}{\omega} uw - \frac{\delta \sin \alpha}{\omega} vw + T_r \delta (u \cos \alpha - v \sin \alpha) = \frac{D_n}{\omega} - \frac{2\delta\beta_0}{\omega} \frac{\partial p_1}{\partial \alpha} + \frac{1}{r} \frac{\partial}{\partial r} r \left(\frac{\partial w}{\partial r} + \frac{\delta w \cos \alpha}{\omega} - \frac{2\delta\beta_0}{\omega} \frac{\partial u}{\partial \alpha} \right) - \frac{1}{r} \frac{\partial}{\partial \alpha} \left(\frac{2\delta\beta_0}{\omega} \frac{\partial v}{\partial \alpha} - \frac{1}{r} \frac{\partial w}{\partial \alpha} + \frac{\delta \sin \alpha}{\omega} w \right) \quad (6)$$

where Ω , ω , D and α are defined by

$$\Omega = \frac{\partial v}{\partial r} + \frac{v}{r} - \frac{1}{r} \frac{\partial u}{\partial \alpha}, \quad \omega = 1 + \delta r \cos \alpha, \quad D = u \frac{\partial}{\partial r} + \frac{v}{r} \frac{\partial}{\partial \alpha} + \frac{\beta_0}{\omega} w \frac{\partial}{\partial \alpha}, \quad \alpha = \theta + \phi \quad (7)$$

The pressure can be written in the following form

$$p = -\frac{D_n s}{\sqrt{2\delta}} + p_1(r, \alpha) + \frac{T_r^2}{16} (\delta + 2\beta_0^2) \left[\left(\frac{c}{a} + r \cos \alpha \right)^2 + 2\beta_0^2 \frac{c}{a} \sin^2 \alpha \right], \quad (8)$$

where, p_1 is the deviation of the pressure in a cross-section and G is a constant representing the pressure gradient along the pipe center-line. The non-dimensional parameters T_r (Taylor number), D_n (Dean number) and β_0 (torsion parameter) are defined earlier. Considering the continuity equation (3), we can introduce the modified stream function ψ which is related to u, v and w by

$$u = \frac{1}{r\omega} \frac{\partial \psi}{\partial \alpha}, \quad v = -\frac{1}{\omega} \frac{\partial \psi}{\partial r} - \frac{\beta_0 r}{\omega} w \quad (9)$$

Putting this equation into equations (4)-(6) and eliminating p_1 in the resulting equations, we get the equations for w and ψ . The equations for w and ψ are actually used for numerical computations and these are not shown for brevity. The boundary conditions at the wall surface are given by

$$w = u = v = 0, \text{ or } w = \psi = \frac{\partial \psi}{\partial r} = 0 \text{ at } r = 1 \quad (10)$$

$$\text{The dimensionless flux is given by, } k = \frac{\sqrt{2}}{\pi} \int_0^1 r dr \int_0^{2\pi} w d\alpha \quad (11)$$

3. METHOD OF NUMERICAL CALCULATION

The numerical calculation technique exactly corresponds to those of Yamamoto, M. M. Alam, Yasuhara and Arivowo [11] and so their description are not reproduced here for brevity. Only we will produce the basic concept of numerical calculation technique. The spectral method is applied for numerical calculations. The Fourier series is used for the circumferential direction α and the series of the Chebyshev polynomials in the radial direction r . That is, we expand ψ and w as

$$w(r, \alpha) = \sum_{n=1}^N w_n^s(r) \sin(n\alpha) + \sum_{n=0}^N w_n^c(r) \cos(n\alpha)$$

$$\psi(r, \alpha) = \sum_{n=1}^N f_n^s(r) \sin(n\alpha) + \sum_{n=0}^N f_n^c(r) \cos(n\alpha) \quad (12)$$

where, N is the truncation number of the Fourier series. The collocation points are taken as

$$R = \cos\left\{\frac{M+2-i}{M+2}\right\}\pi \quad (1 \leq i \leq M+1). \quad (13)$$

The obtained algebraic non-linear equations are solved by an iteration method with under-relaxation. Convergence of the solution is assured by taking $\epsilon_p < 10^{-5}$ where subscript p denotes the iteration number.

4. RESULTS AND DISCUSSION

A helical pipe with circular cross-section has been considered which is rotating at a constant angular velocity. The main flow is due to the pressure gradient force applied along the centre line of the pipe. As the pipe is curved the flow is also subjected to centrifugal force, which results in a two vortex secondary flow which remain symmetric about the horizontal line passing through the centre of the cross-section. But in case of helical pipe, pitch affects the size of the vortices and they no longer remain symmetric. There introduce another force due to the rotation which is termed as coriolis force, which also affects the position, shape and size of the vortices in great deal. If the effects of rotation and curvature are in the same direction, the rotation is called co-rotation, if not, it is called counter

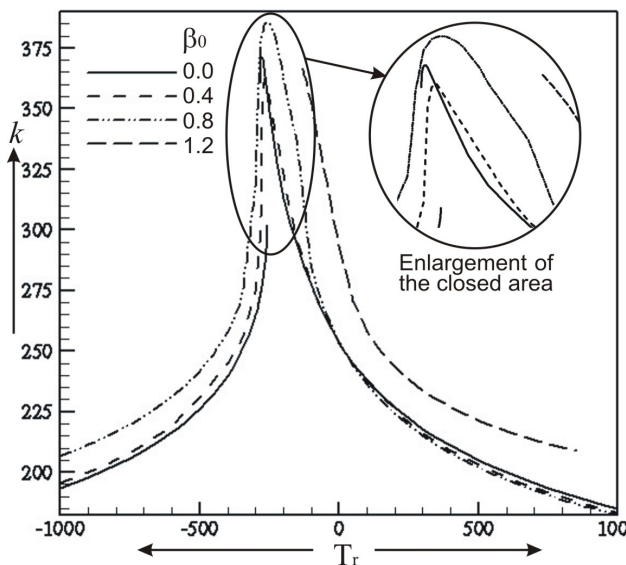


Fig.2 State diagram in terms of Flux k versus Taylor number T_r for different values of β_0 at $D_n=1000$ and $\delta = 0.01$

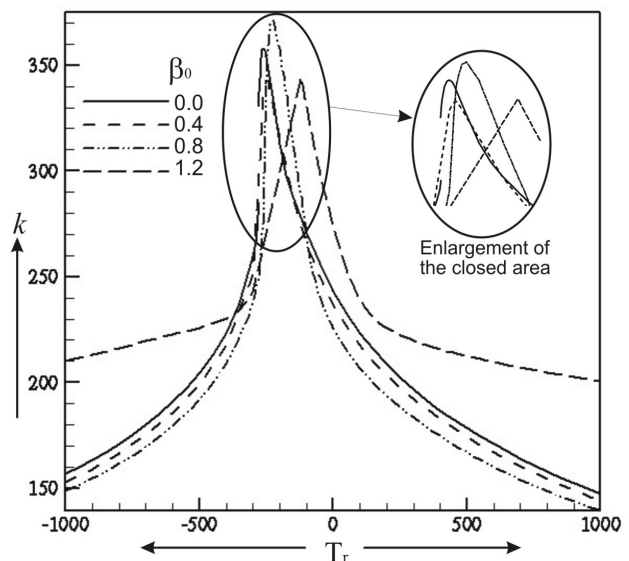


Fig.3 State diagram in terms of Flux k versus Taylor number T_r for different values of β_0 at $D_n=1000$ and $\delta = 0.2$

rotation. K.Yamamoto, M. M. Alam, Yasuhara and Arivowo [11] have studied the present problem for a small range of Dean number and Taylor number. In the present problem numerical calculations have been made at Dean number $D_n = 1000$ with two cases of curvature $\delta = 0.01$ and 0.2 , and the Taylor number T_r ranging from -1000 to 1000 , and a wide range of torsion parameter, $0.0 \leq \beta_0 \leq 1.2$.

The change of flux k with rotation T_r have been shown in fig. 2 and fig. 3 for curvature $\delta = 0.01$ and $\delta = 0.2$ respectively. The flux k decreases as Taylor number T_r decreases for all the cases and the flux reach a highest value at a negative T_r , which may be termed as critical Taylor number. At critical T_r we either get 4-vortex solution or 1-vortex solution. After reaching this point, k decrease for any further decrease in T_r . The critical T_r increases with the increase of β_0 and δ . Though there is no clear correspondence between flux k and torsion parameter β_0 , the maximum flux occurs at $\beta_0 = 0.8$ for both curvature.

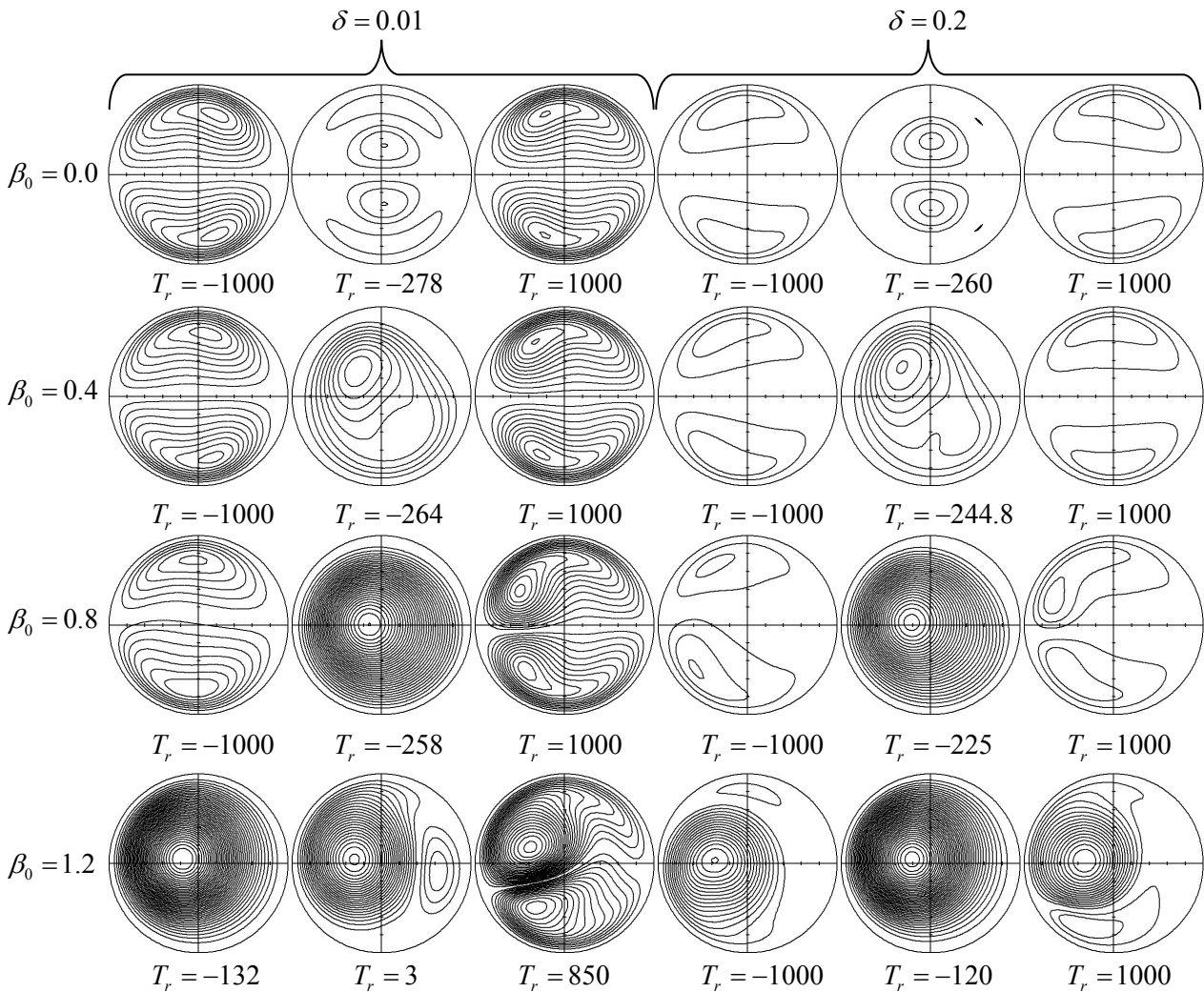


Fig. 4 Variation of the constant ψ – lines with T_r and β_0

The constant ψ – lines of the secondary velocity are shown in fig.4 for different values of T_r, β_0, δ . The left side is the inner wall of the cross-section and the right side is the outer wall of the cross-section. The difference between two consecutive constant ψ – lines is 1.35.

For $\beta_0=0.0$ we have obtained bifurcation solution. For $\beta_0 \neq 0.0$ we have not obtained bifurcation. The 4-vortex and 2-vortex solutions have been shown in Fig. 5 at $T_r = -278$ and $\beta_0 = 0.0$ for both the curvatures $\delta = 0.01, 0.2$. In case of 4-vortex solution there appears two strong vortices near the centre of the cross-section. With the increase of curvature these two vortices are shifted towards the inner wall of the cross-section. The flux is higher for 4-vortex solution than that in 2-vortex solution.

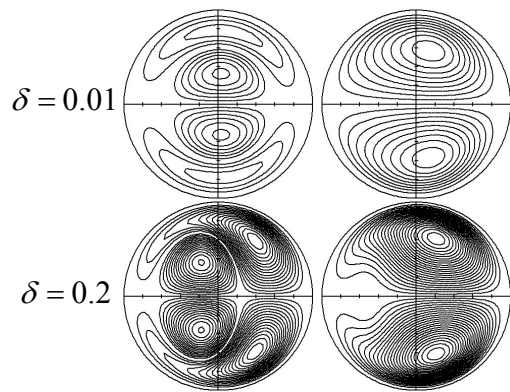


Fig. 5 Dual solution for $T_r = -278$ and $\beta_0 = 0$

For $\delta = 0.01$ and $\beta = 1.2$ we got solution within the range $-132 \leq T_r \leq 850$. Further calculation is under processing.

5. CONCLUSIONS

The upper vortex is stronger than the lower vortex at high T_r . With the decrease of T_r the two vortices changes their position in anti-clock wise rotating manner for the effect of curvature and rotation. When the effect of curvature and rotation balance each other, the maximum flux is found. At this point 4-vortex solution (i.e., bifurcation solution) is found for very low torsion and single vortex solution is found for high torsion. When the effect of rotation exceeds the effect of curvature, again two vortex solutions appears and the small vortex reaches the upper half.

6. REFERENCES

- [1] Dean, W. R., Note on the Motion of Fluid in a Curved Pipe, *Philosophical Magazine and Journal of Science*, 4 (1927), 20, pp. 208-223.
- [2] Miyazaki, H., Combined free- and forced-convective heat transfer and fluid flow in rotating curved circular tube, *International Journal of heat mass transfer*, 14 (1971), pp. 1295-1309.
- [3] Ito, H., Motai, T., Secondary flow in rotating curved pipe, *The reports of the Institute of high speed Mechanics, Tohoku University, Sendai, Japan*, 29, NO. 270 (1974), pp. 33-57.
- [4] Daskopoulos, P., Lenhoff, A. M., Flow in curved ducts: Part 2. Rotating ducts, *Journal of Fluid Mechanics*, 217 (1990), pp. 575-593.
- [5] Wang, C. Y. On the low-Reynolds-number flow in a helical pipe, *Journal of Fluid Mechanics*, 108 (1981), pp. 185-194.
- [6] Manlapaz, R. L., Churchill, S. W., Fully developed laminar flow in a helically coiled tube of finite pitch, *Chemical Engineering Communications*, 7 (1980), 5, pp. 7-78.
- [7] Germano, M., On the effect of torsion on a helical pipe flow, *Journal of Fluid Mechanics*, 125 (1982), pp. 1-8.
- [8] Chen, W. H., Fan, C. N., Finite element analysis of incompressible viscous flow in a helical pipe, *Computational Mechanics*, 1 (1986), pp. 281-292.
- [9] Tuttle, E. R., Laminar flow in twisted pipes, *Journal of Fluid Mechanics*, 219 (1990), pp. 545-570.
- [10] Yamamoto, K., Yanase, S., Yoshida, T., Torsion effect on the flow in a helical pipe, *Fluid Dynamics Research*, 14 (1994), pp. 259-273.
- [11] Yamamoto, K., Mahmud Alam, Junich Yasuhara, Agus Aribowo, Flow through a rotating helical pipe with circular cross-section, *International Journal of Heat and Fluid Flow*, 21 (2000), pp. 213-220.

AN INTEGRAL ANALYSIS OF BOUNDARY LAYER AND SKIN FRICTION OF MOVING VEHICLE

A. Motin, M. A. T. Ali

Department of Mechanical Engineering
Bangladesh University of Engineering and Technology (BUET)
Dhaka-1000, Bangladesh
E-mail: motinme@gmail.com

ABSTRACT

The present work deals with the study of aerodynamic behaviors of flow around car models. The integral analysis of boundary layer is used to quantify the effects of speed on the boundary layer characteristics and skin friction. The experimental data are utilized for characterization of stream wise velocity contour, boundary layer and momentum thicknesses, shape factor, skin friction drag and friction coefficient as a function of vehicle speed. The zone of flow separation approaching laminar-turbulent transition is also investigated. A 1/32 scale car model TOYOTA RAV-4, 2008 is used for this investigation. The experiment is conducted in the 300x300 mm wind tunnel facility of the Department of Mechanical Engineering of BUET at different speed ranges.

KEYWORDS: *Aerodynamics; Boundary layer; Integral analysis; Friction drag; Friction coefficient.*

1. INTRODUCTION

In characterizing the aerodynamic behavior of road vehicles, a drag is one of the most important factors from the viewpoint of fuel economy as found by Hedrick et.al.[2]. From control and stability point of view, however, the side force and yawing moment are the most crucial aerodynamic characteristics of a vehicle [2]. Lift force and pitch movement is especially important to light weight and high speed vehicles like racing car [3] and roll movement are critical in some specific circumstances where strong gust occurs [4]. Earlier publications dealing with the fundamentals of various automobile designs related to vehicle aerodynamics can be found in Scibor Rylski[4], Hucho & Sovran [5] and Sovran et.al.[6]. The integral analysis of boundary layer was originally proposed by Theodore Von Karman and K. Pohlhausen in separate papers in 1921 [1]. The displacement thickness indicates how far the streamlines of the outer flow are displaced by the boundary layer. The flow separation is quite sensitive to small changes in the body shape, particularly if the pressure distribution is strongly affected by the change of the shape of the body as found by H.schlichting [1]. Separation often occurs in regions where the pressure increases and its occurrence becomes more prominent with the magnitude of pressure difference, for example, in bodies with blunt rear sides where the backflow close to the wall causes thickening of the boundary layer and later this boundary layer mass is transported away into the outer flow as produces a stagnation zone in the flow field. At the point of separation the streamlines leaves the wall at a certain angle. The position of separation is given by the condition where the velocity gradient perpendicular to the wall vanishes at the wall, i.e. the wall shear stress, τ_w vanishes. It will be seen that separation occurs in the region of adverse pressure gradient. Whereas, in the outer flow a pressure increase corresponds to a drop in the kinetic

energy. But this phenomenon does happen within the boundary layer where the fluid is retarded by friction. This fluid from the high pressure zone deviates away from the wall and is drawn right into the main flow causing flow separation. This phenomenon in extreme causes leads to a condition where the fluid close to the wall flows in the opposite direction from the downstream side and then to the outer flow forming wakes. The separation point is defined as the boundary between the forward and backward flow in the region close to the wall.

2. EXPERIMENTAL PROCEDURE AND EQUIPMENT

The experiment was carried out in the 300x300 mm open circuit wind tunnel facility in the department of mechanical engineering, BUET using a 1/32 scale car model Toyota RAV-4 2008. The flow in the wind tunnel is produced by two 482 mm axial flow Wood Aerofoil (U.K.) fans. The test section is 1.22 m long with a maximum air speed of 80 km/hr (22 m/s). The schematic diagram of the wind tunnel is shown in figure 1. The fans are placed at the tail end side of the wind tunnel and flow is through the air filter and flow nozzle and is discharged through a silencer and flow regulating butterfly valve. Out of two fans, speed of one fan can be controlled by motor speed controller. Thus the flow is controlled both by controlling the butterfly valve and/or by controlling the fan motor speed. The fan with its discharge unit is separated from the entry unit by a damper to minimize the propagation of vibration, generated in the fan, to the upstream side of the wind tunnel. In upstream side of the damper there are air filter box, flow nozzle, flow nets, entry section, test section, delivery section and diffuser.

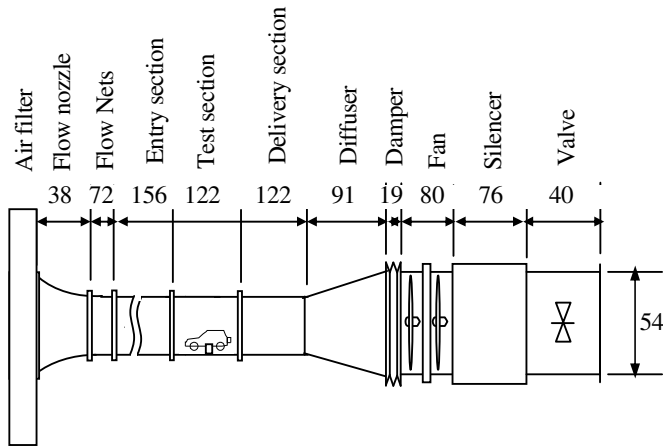


Fig.1: Schematic of wind tunnel (dimensions are in cm)

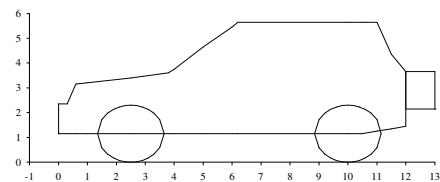


Fig. 2: Model Car dimension

To determine the characteristics of the boundary layer, velocity profiles are measured at several points in the stream wise directions. The profiles are taken with a 3 mm Pitot-static tube (United Sensor, U.S.A.) traversed by a computer controlled 3-axes co-ordinate positioning device. Dynamic pressure at different points around the model is sensed by the Pitot-static tube and transformed into voltage by the pressure transducer interfaced with computer. The Pitot-static tube traversing machine used in this work has the measuring range of 600 mm along X-axis, 500 mm along Y-axis and 250 mm along Z-axis. Three 2-phase stepper motors are mounted on the traversing machine at three different positions. All of the three motors are 12 V and give a stepping angle of 1.8 degree per step. The machine can travel 20 mm by a complete revolution (200 steps) of stepper motor shaft. So, the precision of traversing machine is 0.1 mm. In a wind tunnel test, all possible care is taken to establish conditions consistent with full scale operation. In principle, the model test should satisfy both dynamic as well as geometrical similarity. Dynamic similarity requires that the Reynolds number of the model flow be made to match the Reynolds number in the full scale operation. The characteristic length scale of our model is 1/32 th that of

the full scale vehicle. Since the test is conducted with air as the fluid, the viscosity ν is the same for both cases. To keep Re number constant, the free stream velocity in the test case must be 32 times higher than the full-scale vehicle velocity. This, of course, is not possible. An automobile traveling at highway speed may correspond to $Re = O(10^6-10^7)$, while in this wind tunnel tests are conducted at Reynolds numbers at $Re = O(10^5)$. To see the effect of change of Reynolds number on the velocity profile around the model, flow measurements are taken at different Reynolds number and their results are analyzed. To attain the actual flow condition, simulation technique stated by M. Zabat et. al.[7], is to utilize a series of small roughness elements to artificially “trip” the boundary layer on the model. Tripping insures a turbulent boundary layer more nearly in character with a boundary layer at higher Reynolds number. Two limitations exist for conducting road vehicle experiment in the wind tunnel. First, if one uses a bottom wall of the wind tunnel to model the road surface in it, a layer of slow moving fluid (the ground plane boundary layer) grows continuously in the downstream direction. This layer does not exist on the actual road surface since it is the vehicle that is in motion and not the medium (air). Hucho and Sovran [5] suggest that for a passenger car model affixed to a ground plane, the displacement thickness, δ_1 should be less than 10% of the model ground clearance, h (in this experiment h is about 25 mm). In this experiment, the displacement thickness at the model length of 0.13 m at 21.5 m/s wind speed is found to be 0.13 mm which is much less than the 10% of model ground clearance (2.5 mm). Another limitation exists for conducting road vehicle experiment in the wind tunnel is the blockage effect. The blockage ration, ϕ a factor that is usually used to determine the severity of the disturbance is defined as

$$\phi = \frac{A}{A_n} \quad (1)$$

Where A is the frontal area of the vehicle model, and A_n is the cross section area of the wind tunnel. In this study, the blockage ratio measures about 3% which is much lower than the well accepted limit of 5% for the aerodynamic testing of cars [5]. Therefore the blockage effect is neglected in this investigation. In this experiment the car model is placed in the test section shown in figure-1 and its dimension is shown in figure-2.

3. INTEGRAL ANALYSIS OF BOUNDARY LAYER

The displacement thickness is calculated by using the expression,

$$\delta_1 = \int_0^{\infty} \left(1 - \frac{U}{U_{\infty}}\right) dy \quad (2)$$

The loss of momentum flux for the mass flux $\rho U dy$ between adjacent streamlines is $(U_{\infty} - U)\rho U dy$. Hence the total loss of momentum flux is equivalent to the removal of momentum through a distance δ_2 , called momentum thickness. The integral momentum flux deficit:

$$\rho_{\infty} U_{\infty}^2 \delta_2 = \int_0^{\infty} (U_{\infty} - U) \rho U dy \quad (3)$$

Differentiating with respect to x and substituting the differential operators by using continuity and boundary-layer momentum equation, it is found that U_{∞} is independent of y ,

$$\frac{d}{dx} (\rho_{\infty} U_{\infty}^2 \delta_2) = -[\rho V(U_{\infty} U) + \tau]_0^{\infty} - \frac{dU_{\infty}}{dx} (\rho_{\infty} U_{\infty} \delta_1) \quad (4)$$

Since $U_{\infty} - U$ and τ both vanish at $y = \infty$, whilst $U=0$, $V=V_w$ and $\tau=\tau_w$ at $y=0$,

$$\frac{d}{dx} (\rho_{\infty} U_{\infty}^2 \delta_2) + \rho_{\infty} U_{\infty} \frac{dU_{\infty}}{dx} \delta_1 = \tau_w + \rho_w V_w U_{\infty} \quad (5)$$

This equation is known as Karman’s integral relation. For constant density flow, the most compact form comes by expanding the first differential and dividing by ρU_{∞}^2 :

$$\frac{d\delta_2}{dx} + (2+H) \frac{\delta_2}{U_\infty} \frac{dU_\infty}{dx} = \frac{c_f}{2} + \frac{V_w}{U_\infty} \quad (6)$$

$$\text{Where, } c_f = \frac{\tau_w}{\frac{1}{2}\rho U_\infty^2} = \text{skin friction coefficient} \quad (7)$$

$$H = \frac{\delta_1}{\delta_2} = \text{shape factor} \quad (8)$$

Shape factor is always greater than 1. A large shape factor is an indicator of a boundary layer separation. For the case of zero pressure gradient boundary layer with no wall transpiration, equation (6) takes the simple form

$$\frac{d\delta_2}{dx} = \frac{c_f}{2} \quad (9)$$

Integrating the equation (9) gives the total friction drag coefficient over length L.

$$c_D = \frac{2\delta_2(L)}{L} \quad (10)$$

The drag coefficient can be deduced entirely from the downstream velocity profile.

4. RESULTS AND DISCUSSION

The stream wise velocity contours for different vehicle speed are shown in figure 3, 4 and 5. A wake is generated behind the car and it is found that the wake zone becomes larger as the vehicle speed increases. As a result, it can be said that the pressure drag behind the car is proportional to the car speed. It is also observed that flow separation is occurred from near the frontal area of the top wall and reattached at near the rear area of the top wall. From figure 6 and 7 it is seen that at the leading and trailing zone of the top surface of car, the displacement thickness and momentum thickness is higher at the low speed. As a result, the mass flux deficit is greater. And at the remaining zone i.e.; from 2 cm to 10 cm from the leading edge of the vehicle, no significant effect of speed variation is noticed on the displacement thickness and momentum thickness. The variation of shape factor (ration of displacement thickness to momentum thickness) is shown in figure-8. A large shape factor is an indication of a boundary layer near separation. From the figure 9, it is observed that at the front wind shield of the car the friction coefficient is negative which indicates that back flow or circulation is generated at the front wind shield. At the point of flow separation, the shear stress i.e. friction coefficient becomes zero [1]. Hence, it can be said that at the leading edge of the front wind shield, the flow is separated and reattached at the trailing edge of the front wind shield. It is also observed that the speed variation in the range of measurement has little influence on friction coefficient.

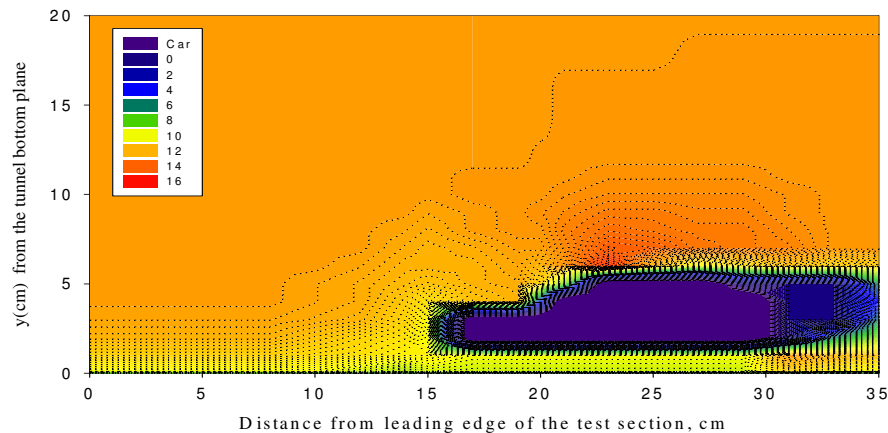


Fig. 3: Contour plot of velocity for single car at free stream velocity of $U_\infty = 12.5$ m/s

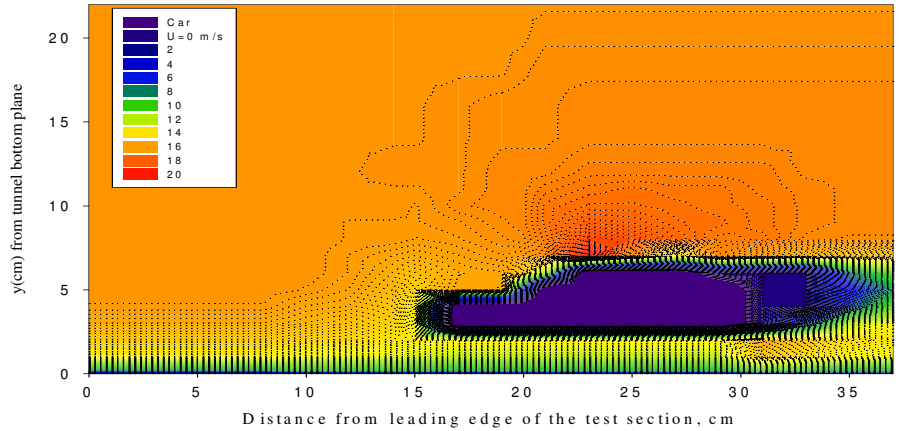


Fig. 4: Contour plot of velocity for single car at free stream velocity of $U_\infty = 16.5$ m/s

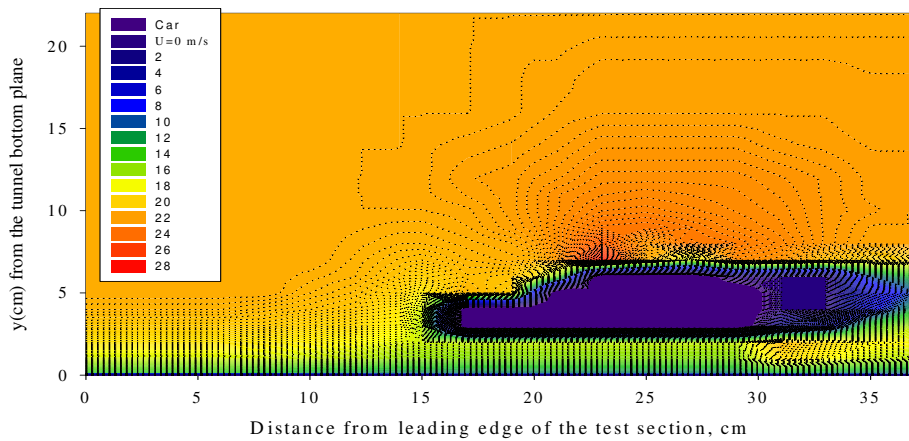


Fig. 5: Contour plot of velocity for single car at free stream velocity of $U_\infty = 21.5$ m/s

In figure 10, it is shown that at the leading edge of the car the friction drag is high and dramatically reduces to a point at 2 cm downward from the leading edge. This is because the flow is separated at the leading edge of the car and reattached immediately after that point it (figure 9). At 3.5 cm to 6 cm downward from the leading edge, friction drag coefficient is reduced again due to the flow separation as shown in figure 9. It is also observed from figure 10 that low speed exhibits higher friction drag than that of higher speed up to a distance of 4 cm from the leading edge of the car and speed variation has no noticeable effect on friction drag after that point.

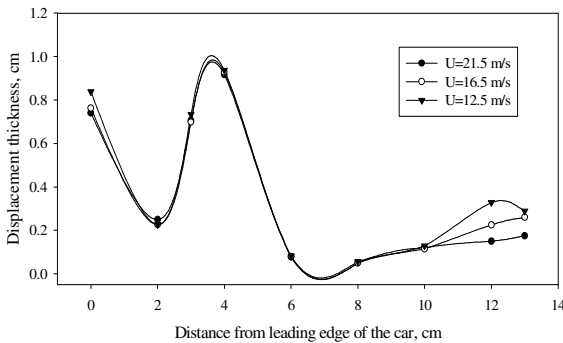


Fig. 6: Variation of displacement thickness on the top wall ($Z=0$) of vehicle.

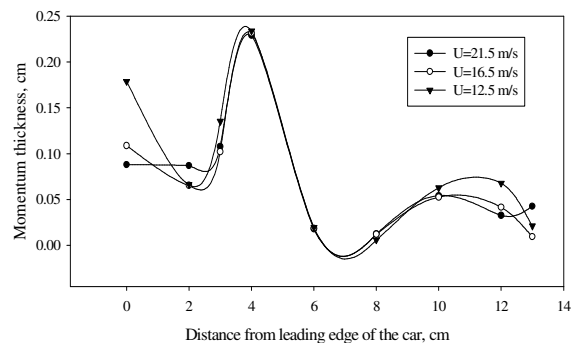


Fig. 7: Variation of Momentum thickness on the top wall ($Z=0$) of vehicle.

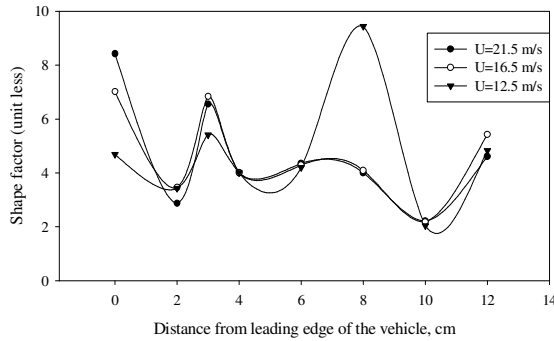


Fig. 8: Variation of Shape factor on the top wall (Z=0) of vehicle.

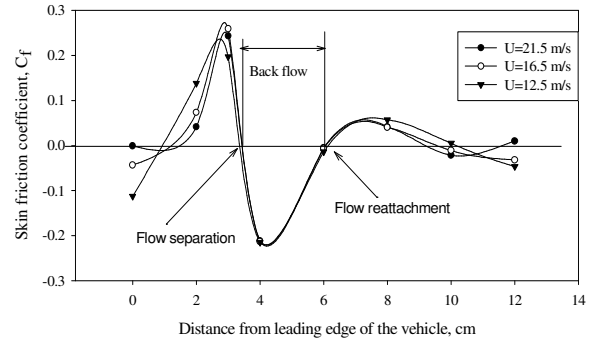


Fig. 9: Variation of friction coefficient on the top wall (Z=0) of vehicle.

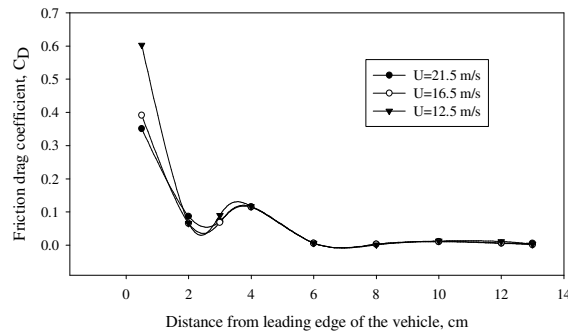


Fig. 10: Variation of friction drag coefficient on the top wall (Z=0) of vehicle.

5. CONCLUSION

In this study, all the parameters studied for characterization of moving vehicle aerodynamics are found well defined. The skin friction drag and friction coefficient are found higher for low vehicle speed and after the leading edge of the front wind shield, vehicle speed variation has no significant influence on skin friction drag. At the leading and trailing zone of the vehicle, the displacement thickness and momentum thickness vary with the car speed. In the rear side of the vehicle, wake is generated which is also a function of vehicle speed.

6. REFERENCES

- [1] H. Schlichting, K. Gersten, "Boundary Layer Theory", Springer, New York, 8th Revised and Enlarged Edition, Reprint-2003, P. 145-194 and 377-411.
- [2] J.K. Hedrick, J.L. Tsuei, Ö. Savas, "Transient Platoon Aerodynamics during Passing Maneuvers and In-line Oscillations", California PATH Research Report, UCB-ITS-PRR-2000-26
- [3] Howell, J., "Catastrophic lift force on Racing cars", J. Wind Eng. Ind. Aerodyn., Vol. 9, 1981.
- [4] Skibor-Rylski A.J. "Road vehicle aerodynamics", Pentech press, London, 1975
- [5] Hucho, W-H., Sovran, G.; "Aerodynamics of Road Vehicles", Annu. Rev. Fluid Mech.; 2.No. 25; 1993, p. 485-537
- [6] Sovran, G., Morel, T., Mason, W. T., Jr. (ed), "Aerodynamics drag mechanisms of bluff bodies and road vehicles", Plenum press, New York, 1978.
- [7] M. Zabat, S. Frascaroli, F. Browand, "Drag Measurements on a Platoon of Vehicles California PATH Research Paper", UCB-ITS-PRR-93-27

FREE SURFACE FLOW OVER A BUMP WITH HYDRAULIC JUMP

N. Dewangan, A. K. Das and P. K. Das

Department of Mechanical Engineering, Indian Institute of Technology, Kharagpur- 721302, India
Phone: 03222-282916, Fax: 03222-282278, Email: arup@mech.iitkgp.ernet.in

ABSTRACT:

Flow pattern in a rectangular open channel flow over a semi circular bump is investigated numerically. Mass conservation equation for the mixture phase and Reynolds-Averaged Navier-Stokes equation is employed for the present simulation. For turbulence modeling $k - \epsilon$ model is adopted along with the appropriate closure law. At the down stream of the bump different shapes of hydraulic jumps were observed. Systematic studies have been made to correlate type of hydraulic jump with water depth at the inlet and stream velocity. It has been observed that dominant hydraulic jump is occurred at low and high water depth for a high and low range of water velocity respectively.

Key words: Free surface flow, Hydraulic jump, Bump, Reynolds-Averaged Navier-Stokes equation, $k - \epsilon$ model.

1. INTRODUCTION

Free surface flows over an obstacle in a rectangular channel of constant width are of great interest for various mechanical and civil engineering systems. In nature also several situations arises like flow in a river bed, debris flow over drainage network, where open channel flow over a bump becomes significant. Fluid flow phenomena after the obstruction take different shapes depending on the upcoming stream velocity and obstruction height. If the stream height is large enough it surpasses the obstruction but in case of shallow liquid level fluid stream climbs the obstruction and then jumps from its top position. After passing the obstruction the stream can follow its upstream texture or make a hydraulic jump immediately downstream the obstruction. Hydraulic jump is a phenomenon in which flow with high velocity and small depth is rapidly changed to flow with low velocity and large depth. This type of flow phenomena is common in nature starting from kitchen sink to sea bed. Due to its practical importance and engineering interest several researchers tried to analyze the flow situation either experimentally or using analytic techniques.

Pratt [1] reported two different types of situation arise when a stratified liquid passes over a bump. In case of sub-critical flow ($Fr < 1$) stream cannot progress forward surmounting the bump. For $Fr > 1$ at the apex of the bump the flow becomes supercritical at the downstream of the bump and a hydraulic jump occurs immediately to make the flow sub-critical again. Analytically this is first established by Faltas et al. [2] when they studied inviscid, incompressible and steady flow over a trapezoidal bump. Taking queue from their observation Baines and Whitehead [3] made an elaborate study of flow configuration after the jump at various operating condition and investigated about the

stability of hydraulic jump. Similar analysis for free surface flow with hydraulic jump in an open channel flow was performed by Steinruck et al. [4] considering Reynolds numbers and Froude Number to be approaching towards the critical value, with fully developed turbulent intensity for upstream. But still voidage is there which needs to be filled up with systematic in detail study of the phenomena.

In the present paper we have observed the flow configuration after the bump in fluid stream by numerical simulation. Among different types of configuration hydraulic jumps are also observed at different location, depending on the upstream height (i.e. water depth) and the velocity of flow. The analysis is performed in steady state and $k - \epsilon$ turbulence model by using commercial software, Ansys- CFX for simulation and ICEM for geometry generation.

2. THEORITICAL MODEL

In multiphase flow, individual phase characteristics can be obtained via ensemble averaging of the exact conservation equations for each phase with appropriate closure law between them. In this work, *mixture* equations are integrated, which are obtained through the addition of the mass and momentum conservation equations for the liquid and gas. Eventually mixture model solves the conservation equation in one phase accounting a bleak contribution of the other phase. At the interface both the phases become competent with each other and property of the interface depends over the grasp of one phase near the interface. For a *dilute* mixture, following equations can describe the situations:

Conservation of mass for the mixture:

$$\frac{\partial(\rho_m)}{\partial t} + \nabla \cdot (\rho_m \bar{v}_m) = 0 \quad (1)$$

Conservation of momentum for the mixture:

$$\frac{\partial(\bar{v}_m \rho_m)}{\partial t} + \nabla \cdot (\rho_m \bar{v}_m \otimes \bar{v}_m) + \nabla p_m = \nabla \cdot T_m + \rho_m \bar{g} \quad (2)$$

where the subscript m indicates mixture variable, ρ is the density, v is the velocity vector, p is pressure, \otimes is the tensorial product, and g is indicates the vector related to the acceleration of gravity. The simulation of turbulence effects in the perspective of conservation of momentum substantiates a second averaging (or filtering) process.

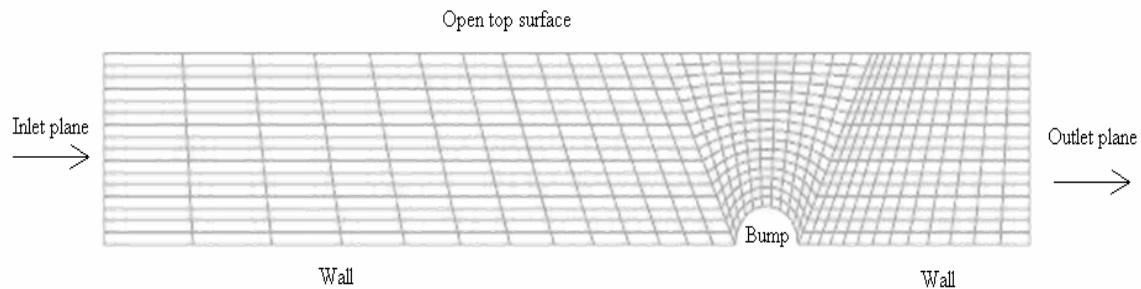


Figure 1. A typical mesh of the problem domain

In the present methodology we have used $k-\varepsilon$ turbulence model for calculation of Reynolds stress tensor T_m in the above mentioned Reynolds-Averaged Navier-Stokes (RANS) environment. The free surface location is computed using the very efficient Volume fraction method. Above-mentioned system of equation is solved using commercial software Ansys-CFX which uses a structured finite-volume numerical methodology.

3. NUMERICAL SIMULATION

3.a. MESH GENERATION

For the present simulation a 2D channel of 1 m length and 0.15 m height is considered. At the middle of the channel one semicircular bump of 0.03m radius is kept. Ansys-ICEM software is used to generate the geometry and meshing. Block topology technique is used for accurate meshing of the domain with hexahedral control volumes. As the flow phenomena near the bump holds the key of the downstream flow configuration special care has been given for meshing near the bump. Mesh adaption technique is used to refine grids at bump.

After the grid generation 2D domain of interest is extruded for a very small width and converted into 3D geometry for proper adaptation in CFX. A typical pictorial view of the domain and generated mesh (exaggerated mesh length) is shown in fig. 1. Left hand plane is denoted as entry of the channel and right hand side is the exit. For the present simulation it is assumed that top of the geometry is opened to atmosphere and bump is attached with the bottom wall of the geometry.

3.b. SIMULATION PROCEDURE:

At first boundary conditions are specified using CFX-Pre and control parameters are defined for setting up proper iteration and mesh adaptation value. At inlet free surface is defined above which volume fraction of air is 1. At the inlet velocity of water is specified. At the outlet pressure is specified which governs the fluid height at the exit plane. Pressure above the free surface is kept constant and pressure below the free surface follows hydrostatic distribution assuming an arbitrary stream depth. The simulation near the bump is not sensitive to the exact outlet fluid height, so a crude approximation during initialization is sufficient. Air and water at atmospheric pressure is used as test fluid in the simulation. Buoyancy force is taken into account in the momentum equation.

At the top pressure is specified and volume fraction is 1 for air and 0 for water. Zero gradient of turbulence intensity and zero relative pressure are also assumed at the top. At the bottom smooth wall boundary condition with no slip and no penetration is assumed. For the third dimensional planes symmetry boundary conditions are applied.

Mesh adaptation is set up by giving number of steps of iterations. Within the first round of iteration is completed, the first step of adaption is performed. It contains the number of elements refined and size of the new mesh. After mesh refinement there is a jump in the residual level. This is because the solution from the old mesh is interpolated on to the new mesh. Coupled volume fraction solver is used which converges faster than the other segregated algorithm for buoyancy driven problems.

4. RESULTS AND DISCUSSIONS:

Simulations have been made for different water depth at the inlet and inlet velocity. Contours of different volume fraction is plotted to identify various types of flow configurations after the jump. It is observed that at low liquid height at the inlet water stream surpasses the bump but shows no hydraulic jump at the downstream (Sl. No. 1 and 3 in fig. 2). Downstream liquid height (H_1) is more or less comparable with upstream jet height (H_2). But when the stream velocity is increased at a very high value H_2 starts creeping up (Sl. No. 2 and 4 in fig. 2). It shows a phenomenon which is similar to traveling jump.

As the inlet height of the liquid jet is increased and it crosses the height of the bump in the channel hydraulic jump can occur even at a very low speed. In fig. 2 it has been shown that for an inlet height of 0.04 m (greater than bump height) jump starts at 0.1m/s water velocity. But minute observation of the jump configuration reveals that start of jump does not occur immediately after the bump as in case of Sl. No. 2 and 4. Here, flow takes some time to stabilize after crossing the bump. As a result jump occurs but at a certain distance after the bump. This is evidence in even higher water level (0.05 m) at the inlet. But at higher level of inlet stream height increase of stream velocity shows a different picture. As the velocity increases stream never gets time to stabilize after crossing the bump. It surpasses the bump and due to restriction it increase its downstream height ($H_2 > H_1$). At liquid height of 0.04 and 0.05 m similar things have been observed. It can also been observed from Sl. No. 5 and 7 that stabilizing distance required for jump is higher at high depth of stream. Investigation has also been made to study the transition of jump to no jump condition at high liquid level at the inlet. It has been seen that after jump in one situation downstream liquid height becomes smaller compared to upstream liquid height. In Sl. No. 10 of fig. 2 pictorial view of the volume fraction contour shows a similar phenomenon. Accordingly we have tried to identify different types of flow configurations and categorize them into five categories. Following table shows the categorization of downstream configuration of different types.

Table 1: Definition of different types of jump

Type I	No jump, thin water layer at upstream as well as downstream
Type II	Jump at downstream, at high speed
Type III	Jump at the downstream, at low speed
Type IV	No jump, thick layer at downstream as compared to upstream
Type V	No jump, thick layer at upstream and thin layer at downstream

Finally it can be observed from fig. 2 that hydraulic jump is visible at two locations, first when there is a low velocity and high depth, and second at high velocity and low depth. Effort has also been made to quantify the jump and no jump condition in terms of liquid height at the inlet and stream velocity. It has been seen from fig. 3 that at low stream height jump starts at a very high jet speed and continues as the velocity increases. But for high stream height jump occurs at a very low speed and most of the position of the map is occupied by no jump situation.





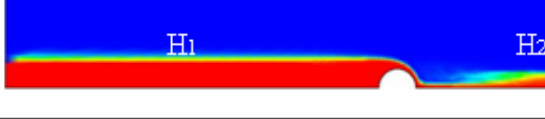
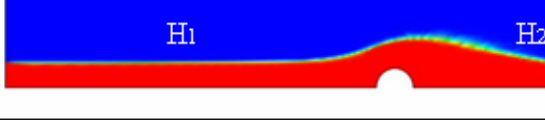



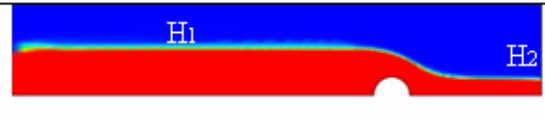
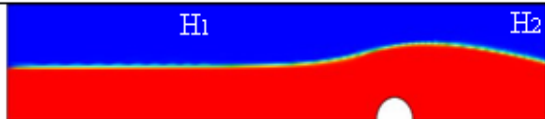
Sl. No.	Depth of water h [m]	Velocity V [m/s]	Pictorial View	Type of flow
1	0.01	1.5		I ($H_1 \approx H_2$) No Jump
2		8.0		II ($H_1 < H_2$) Jump
3	0.02	4		I ($H_1 \approx H_2$) No Jump
4		12		II ($H_1 < H_2$) Jump
5	0.04	0.12		III ($H_1 > H_2$) Jump
6		1.5		IV ($H_1 \approx H_2$) No Jump
7	0.05	0.1		III ($H_1 > H_2$) Jump
8		3.0		IV ($H_1 \approx H_2$) No Jump
9	0.07	0.08		III ($H_1 > H_2$) Jump
10		0.7		V ($H_1 > H_2$) No Jump
11		3.0		IV ($H_1 \approx H_2$) No Jump

Figure 2. Different types of flow configurations for various stream height and velocity

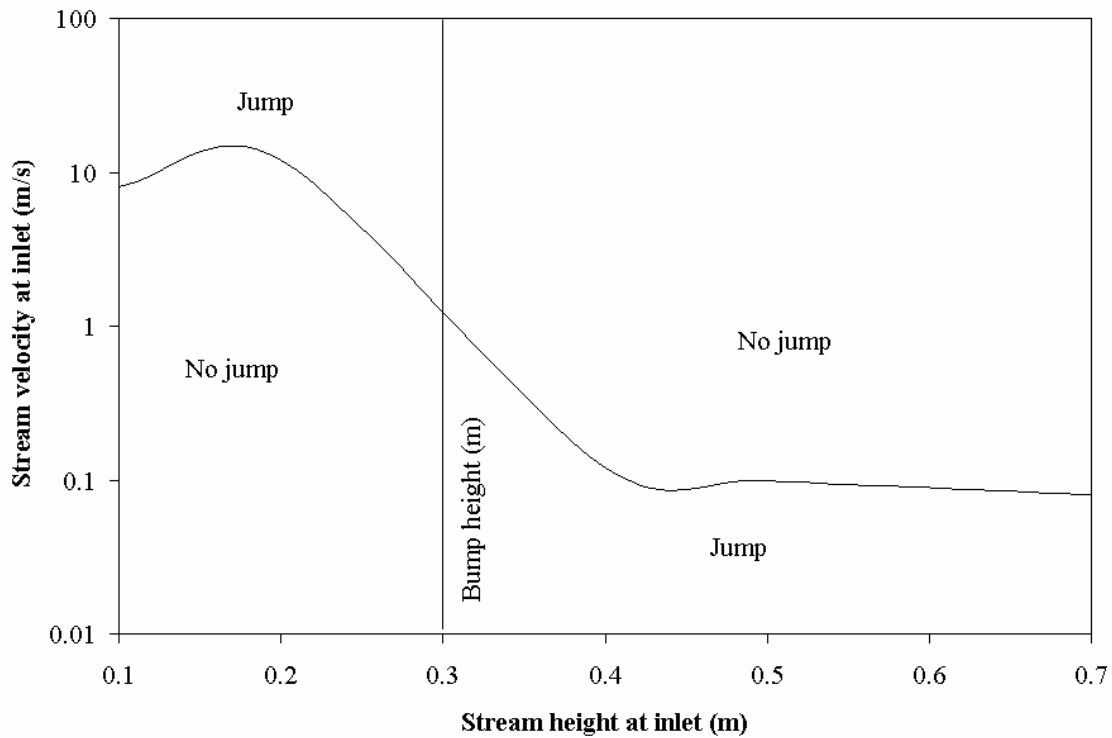


Figure 3. Map for jump location in terms of stream height and velocity at inlet

5. CONCLUSIONS:

A detailed investigation of water flow past a semi circular bump in a rectangular channel is made. Homogeneous equations with appropriate volume fraction correction have been used for simulation. Appropriate turbulence closure relationship is incorporated in the basic model. Qualitative studies of downstream configuration have been made by varying inlet liquid height and water velocity. It has been observed that hydraulic jump occurs at high liquid velocity for low liquid level and low liquid velocity at high liquid level. In other cases, fluid stream bypasses the bump and continues to flow at the downstream depending on the stream height at the inlet.

REFERENCE

- [1] Pratt, L. J., A note on nonlinear flow over obstacles, *Geophys. Astrophys. Fluid Dyn.*, 24 (1983), pp. 63-68.
- [2] Faltas, M. S., Hanna, S. N., Abd-el-Malek M. B., Linearised solution of a free-surface flow over a trapezoidal obstacle, *Acta Mechanica*, 78 (1989), pp. 219-233.
- [3] Baines P. J., Whitehead J. A., On multiple states in single- layer flows, *Physics of Fluid*, 15 (2003), pp. 298-307.
- [4] Steinruck H., Schneider, W., Grillhofer, W., A multiple scales analysis of the undular hydraulic jump in turbulent open channel flow, *Fluid Dynamics Research*, 33 (2003), pp. 41-55.

HIGH CURVATURE EFFECTS ON FLUID FLOW THROUGH CURVED PIPE WITH CIRCULAR CROSS-SECTION

M. A. Masud, Md. Rabiul Islam, Md. Rasel Sheikh and Md. Mahmud Alam*

Mathematics Discipline, Khulna University, Khulna-9208, Bangladesh
e-mail: alam_mahmud2000@yahoo.com

ABSTRACT

Numerical study is performed to investigate the fluid flow through a curved pipe with circular cross-section under various conditions. Spectral method is applied as a main tool for the numerical technique; where, Fourier series, Chebyshev polynomials, Collocation methods, and Iteration method are used as secondary tools. The incompressible viscous steady flow through a curved pipe with circular cross-section is investigated numerically to examine the combined effects of high Dean Number D_n and curvature δ . The flow patterns have been shown graphically for large Dean Numbers and a wide range of curvature, $0.01 \leq \delta \leq 0.9$. Two vortex solutions have been found for secondary flow. Axial velocity has been found to increase with the increase of Dean number and decrease with the increase of curvature. For high Dean number and low curvature almost all the fluid particle leave the inner half of the cross-section.

Keyword: Curved pipe, High curvature, Dean number, Circular cross-section.

1. INTRODUCTION

Fluid flow through curved duct has been studied at different times because of its importance in various purposes e.g. chemical, mechanical and biological engineering. Curved ducts are used as parts of pipe line, heat exchangers, cooling systems, chemical reactors, gas turbines, centrifugal pumps, etc. Uses of curved ducts are also found in human arterial system. The first experimental work on curved duct flow was done before about more than one century ago in 1876. Again such type of flow was studied by Williams *et al.* [1], Eustice [2,3,4]. But Dean [5,6] was the first author to formulate the problem mathematically. Here incompressible viscous fluid flow under constant pressure gradient force has been investigated and the flow is found to be dependent on a parameter termed as Dean number D_n given by $D_n = \frac{a^3}{\mu v} \sqrt{\frac{2a}{L}} G$; where, μ is the coefficient of viscosity, v is the kinematic viscosity, G is the pressure gradient force, L is the radius of curvature and a is the radius of the cross-section. This type of flow is called Dean flow.

In addition to pressure gradient force, because of the centrifugal force resulting from the curvature of the pipe curved duct flow exerts interesting flow features. One of these interesting features is the bifurcation of the flow in case of Dean number higher than a critical value. The bifurcation of the flow was first observed by Dennis and Ng [7] and Fourier finite difference method was used. Dual solution was found for small curvature and Dean number larger than 956. Below this value only two vortex solutions was found. They used the same Dean number as Dean [5,6] used. Nandakumar and Masliyah [8] also found the bifurcation structure applying the finite difference method. Daskopoulos and Lenhoff [9] found dual solution in Dean flow. Cheng and Mok [10] performed an experimental study on the bifurcation of the flow in a curved circular tube using visualization technique and showed that

*Corresponding author

the critical Dean number decreases as curvature increases. Nandakumar and Masliyah [8] and Kao [11] studied the bifurcation numerically to show that the critical Dean number increases with increase of curvature which contradicts the experimental result of Cheng and Mok [10]. So the effect of curvature on bifurcation was not clearly understood. Yanase *et al.*[12] studied the Dean flow for $0 \leq \delta \leq 0.8$, $D_n \leq 10,000$.

Hence, our aim is to obtain a detail result on the Dean flow at curvature $0.01 \leq \delta \leq 0.9$ and Dean number $D_n \leq 15,000$.

2. GOVERNING EQUATIONS

For the curved pipe flow we take the coordinate system as shown in the Fig. 1 where, O is the centre of curvature, L is the radius of the pipe, a is the radius of the cross-section, α is the circumferential angle, θ is the axial variable and r is the radial variable. The variables are nondimensionalized as,

$$u' = \frac{q_r}{\frac{\nu}{a}} \quad v' = \frac{q_\alpha}{\frac{\nu}{a}} \quad w' = \frac{q_\theta}{\frac{\nu}{a}} \sqrt{\frac{2a}{L}} \quad r' = \frac{r}{a} \quad S' = \frac{L\theta}{a} \quad \frac{a}{L} = \delta \quad p' = \frac{p}{\rho \left(\frac{\nu}{a}\right)^2}$$

Here, u', v', w' are non-dimensional velocities along the radial, circumferential and axial direction respectively. r' is non-dimensional radius, S' is the nondimensional axial variable, δ is non-dimensional curvature and p' non-dimensional pressure. The other variables without primes are dimensional variables. Constant pressure gradient force is applied along the axial direction through the centre of cross section. At the centre of the cross-section $r=0$ and at the boundary of the cross-section $r=a$, where all the velocity components are zero. In dimensionless form this reduces to $r'=0$ at the centre of cross-section and $r'=1$ at the boundary of the cross-section. With the help of the above dimensionless variables and the boundary conditions the equation of motion reduces to the following form,

$$\frac{1}{r'} \left\{ \frac{\partial \psi}{\partial r'} \frac{\partial (\Delta \psi)}{\partial \alpha} - \frac{\partial \psi}{\partial \alpha} \frac{\partial (\Delta \psi)}{\partial r'} \right\} + \Delta^2 \psi + w' \left(\sin \alpha \frac{\partial w'}{\partial r'} + \frac{\cos \alpha}{r'} \frac{\partial w'}{\partial \alpha} \right) = 0 \quad (1)$$

$$\text{And, } \frac{1}{r'} \left(\frac{\partial \psi}{\partial r'} \frac{\partial w'}{\partial \alpha} - \frac{\partial \psi}{\partial \alpha} \frac{\partial w'}{\partial r'} \right) + \Delta w' + D_n = 0 \quad (2)$$

$$\text{where, } \Delta \equiv \frac{\partial^2}{\partial r'^2} + \frac{1}{r'} \frac{\partial}{\partial r'} + \frac{1}{r'^2} \frac{\partial^2}{\partial \alpha^2}, \quad G = -\frac{\partial p}{\partial S} \quad \text{and} \quad D_n = \frac{a^3}{\mu \nu} \sqrt{\frac{2a}{L}} G.$$

Here, ψ is the stream function defined by, $u' = \frac{1}{r'} \frac{\partial \psi}{\partial \alpha}$, $v' = -\frac{\partial \psi}{\partial r'}$. G is the constant pressure gradient force, μ is the viscosity, ν is the kinematic viscosity and D_n is the Dean number.

$$\text{The dimensionless flux } \kappa \text{ is given by, } \kappa = \frac{\sqrt{2}}{\pi} \int_0^1 r' \int_0^{2\pi} w' d\alpha dr'$$

3. NUMERICAL TECHNIQUE

The Spectral method has been used to solve the equations (1) and (2). Fourier series and Chebyshev polynomials are used in circumferential and radial directions respectively. Assuming that steady solution is symmetric with respect to the horizontal line of the cross-section, ψ and w' are expanded as,

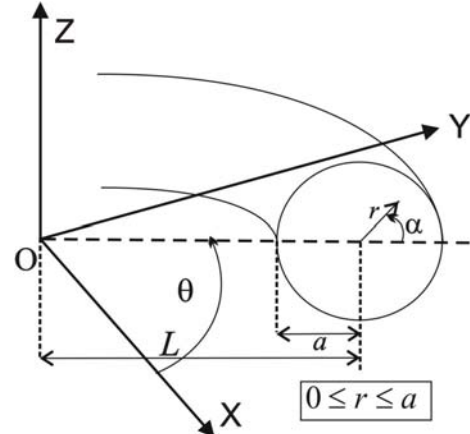


Fig.1 Coordinate system for curved pipe

$$\psi(r', \alpha) = \sum_{n=1}^N f_n^s(r') \sin n\alpha + \sum_{n=0}^N f_n^c(r') \cos n\alpha$$

and

$$w'(r', \alpha) = \sum_{n=1}^N w_n^s(r') \sin n\alpha + \sum_{n=0}^N w_n^c(r') \cos n\alpha$$

where, N is the truncation number of the Fourier series.

The collocation points are taken to be, $R = \cos\left\{\frac{N+2-i}{N+2}\right\}\pi$ [$1 \leq i \leq N+1$]. Then we get non-linear equations for $W_{nm}^s, W_{nm}^c, F_{nm}^s, F_{nm}^c$. The obtained non-linear algebraic equations are solved under by an iteration method with under-relaxation. Convergence of this solution is taken up to five decimal places by taking $\varepsilon_p < 10^{-5}$, where

$$\varepsilon_p = \sum_{n=1}^N \sum_{m=0}^M \left[\left(F_{nm}^{s(p)} - F_{nm}^{s(p+1)} \right)^2 + \left(W_{nm}^{s(p)} - W_{nm}^{s(p+1)} \right)^2 \right] + \sum_{n=0}^N \sum_{m=0}^M \left[\left(F_{nm}^{c(p)} - F_{nm}^{c(p+1)} \right)^2 + \left(W_{nm}^{c(p)} - W_{nm}^{c(p+1)} \right)^2 \right]$$

Here, p is the iteration number. The values of M and N are taken to be 60 and 35 respectively for better accuracy.

4. RESULTS AND DISCUSSION

Steady laminar flow for viscous incompressible fluid has been analyzed under the action high pressure gradient force applied along the centre line of the cross-section for a wide range of curvature $0.01 \leq \delta \leq 0.9$. The total flow is found to decreases as the curvature increases which have been shown in fig. 2. From fig. 3 it is clear that the rate of decrease of flux diminishes as curvature increase.

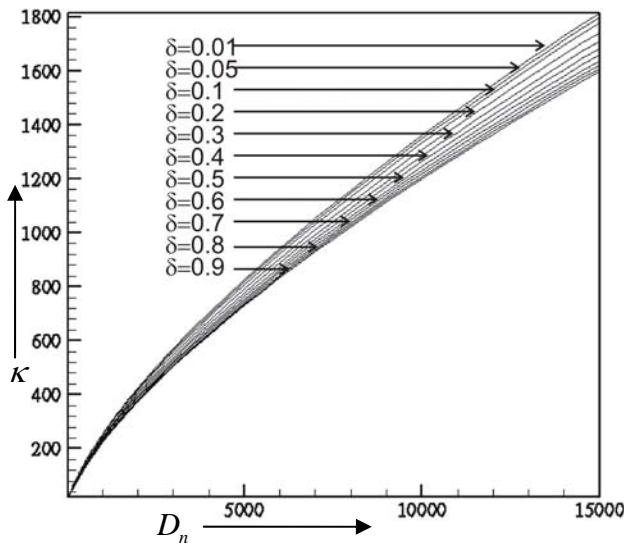


Fig.2 Dean number D_n versus flux κ for different values of curvature

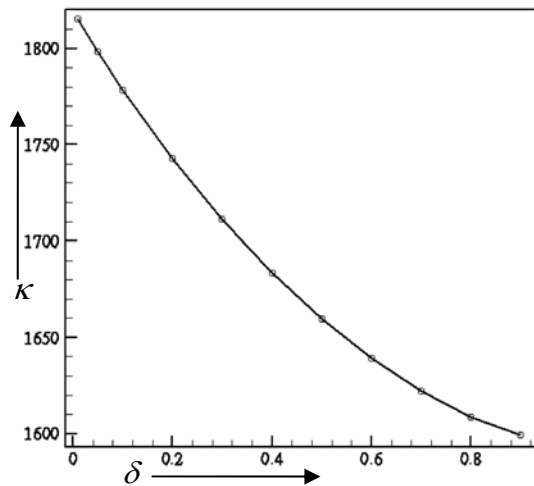


Fig. 3 Flux κ versus curvature δ for Dean number $D_n = 15,000$

In fig. 4 the left side is the inner wall and the right side is the outer wall of the cross-section. As curvature increases there originate a secondary flow and only 2-vortex solution has been found for the secondary flow. The increment in the constant ψ -lines of the secondary flow is taken to be 1.6 and is shown in fig. 4.

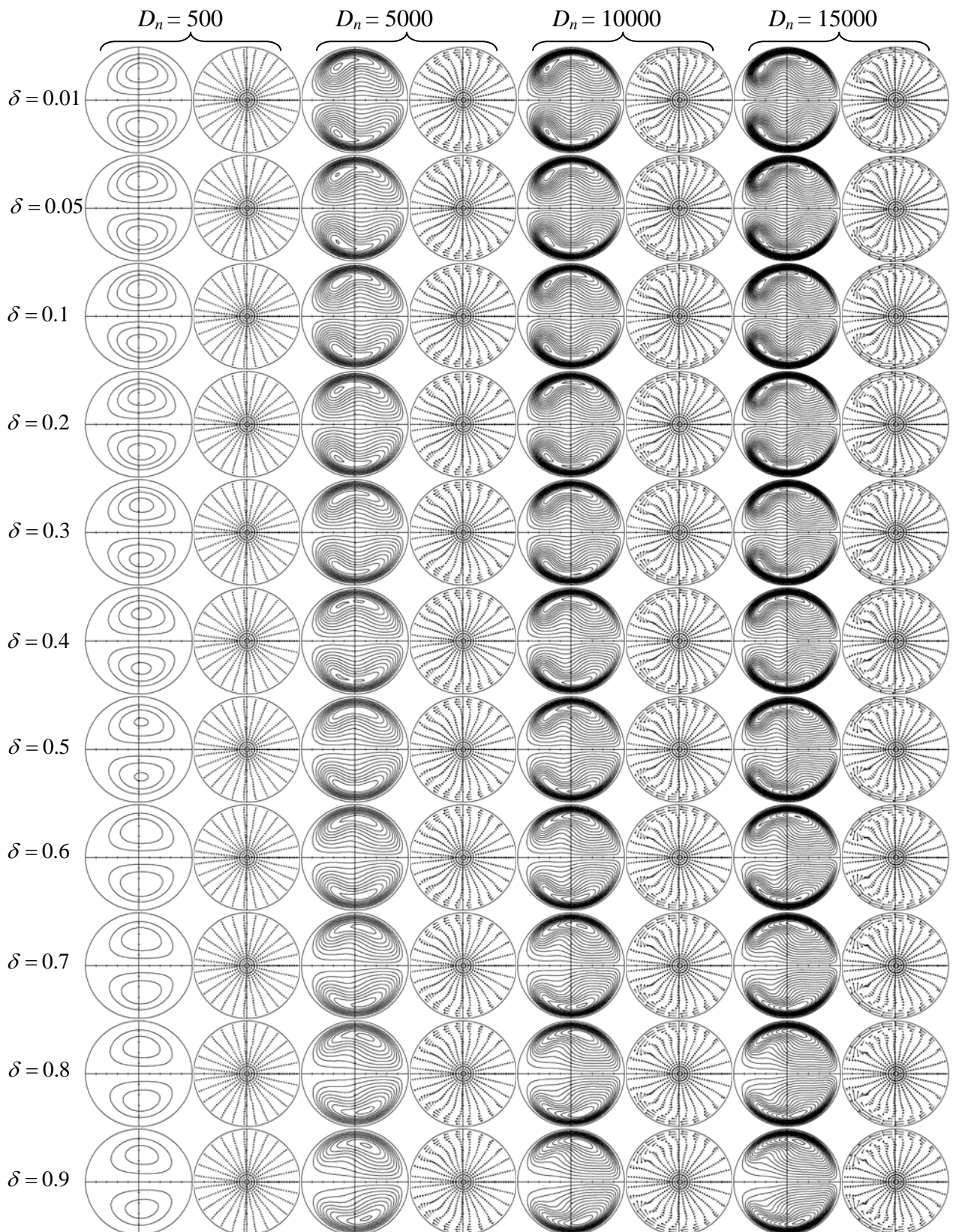


Fig.4 Stream lines and vector plots of the secondary flow at different values curvature $\delta = 0.01, 0.05, 0.1, 0.2, 0.3, 0.4, 0.5, 0.6, 0.7, 0.8, 0.9$ and Dean number $D_n = 500, 5000, 10000, 15000$

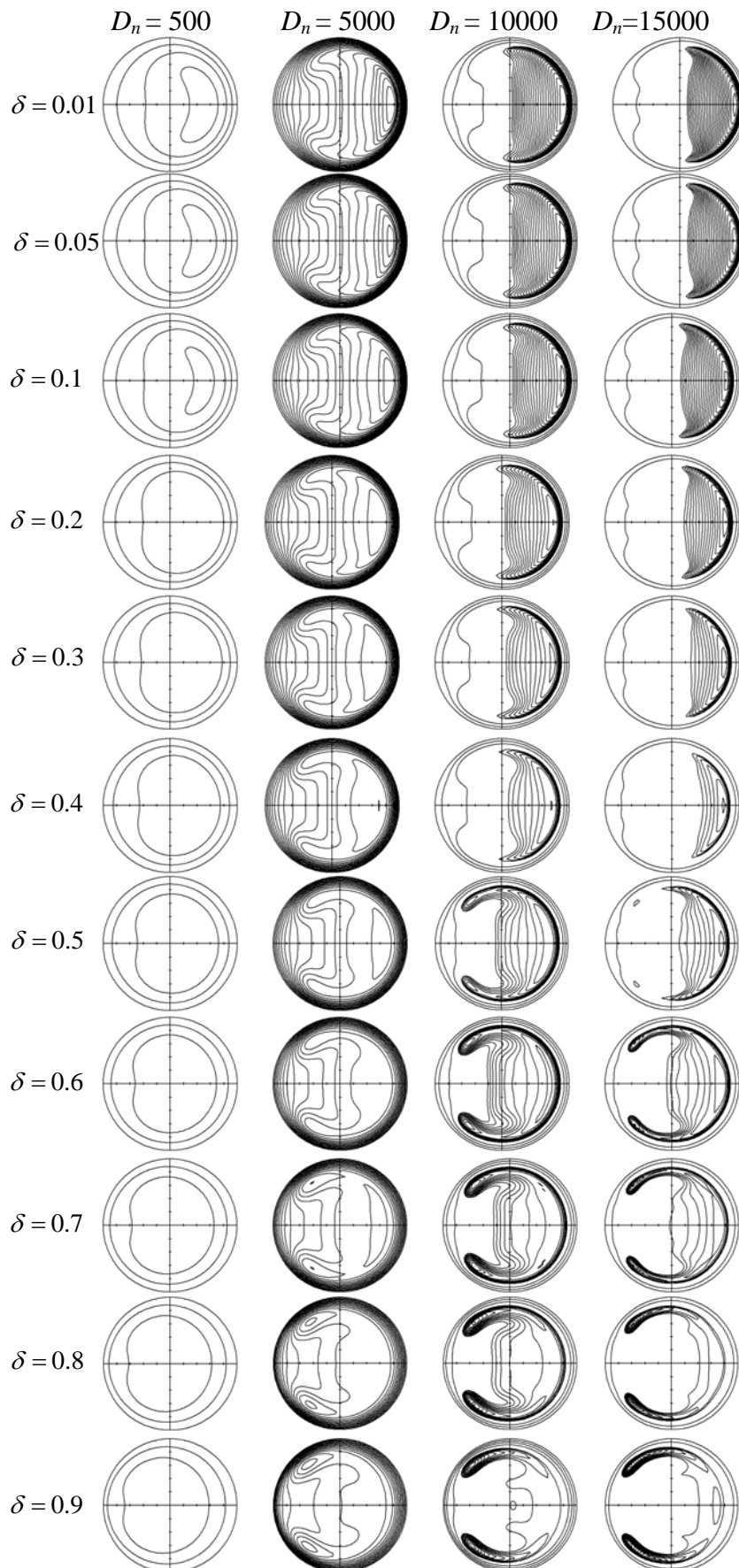


Fig. 5 Contour plots of the axial flow at different values of curvature $\delta = 0.01, 0.05, 0.1, 0.2, 0.3, 0.4, 0.5, 0.6, 0.7, 0.8, 0.9$ and Dean numbers $D_n = 500, 5000, 10000, 15000$

The two vortices are of same strength but rotating in opposite direction. The vector plots of the secondary flow show the direction of the fluid particles and the strength of the vortex is shifted towards outer half of the cross-section as curvature increases.

The axial flow is greater in magnitude than secondary flow and it varies a great deal with curvature. As a result the difference between two consecutive contours of the axial flow has been taken different for different curvatures and different Dean numbers, which are given in the tab. 1. In case of axial flow, the fluid particles are shifted towards the outer wall of the cross section and form a *high velocity band* inside the outer wall of the cross-section. As curvature decreases the magnitude of the axial flow gets higher. The axial flow increase with the increase of Dean number. The maximum flux is found for the highest Dean number $D_n = 15000$ and lowest curvature $\delta = 0.01$; and in this case contour plot of the axial flow reveals that almost all the particles have been shifted towards the outer half of the cross-section. With the increase

of curvature the particles having maximum axial velocity tends to shift towards the middle of the outer wall of the cross-section and for further increase of curvature some particles with higher velocity is found in the up-left and down-left portion of the cross-section.

The effect of continuous change of curvature on the flow will be shown in our further study.

Table 1: Difference between the contours for various values of Dean number and curvature

	$D_n = 500$	$D_n = 5000$	$D_n = 10000$	$D_n = 15000$
$\delta = 0.01$	25	25	165	350
$\delta = 0.05$	25	25	165	350
$\delta = 0.1$	25	25	165	350
$\delta = 0.2$	25	25	165	350
$\delta = 0.3$	25	25	165	350
$\delta = 0.4$	25	25	165	350
$\delta = 0.5$	25	25	150	320
$\delta = 0.6$	25	25	140	300
$\delta = 0.7$	25	25	140	300
$\delta = 0.8$	25	25	140	300
$\delta = 0.9$	25	25	110	290

5. CONCLUSIONS

Two vortex solutions have been found and the strength of the vortices is shifted to the outer half from the inner half with the increase of curvature. The axial flow is shifted towards the outer wall and for high Dean number a high velocity band is formed which gradually gets stronger with the increase of Dean number and due to increase of curvature it is divided into two parts, which are shifted in the upper and lower portion of the inner half.

6. REFERENCES

- [1] Williams, G. S., Hubbell, C. W., Finkell, G. H., Experiments at Detroit, Michigan on the effect of curvature on the flow of water in pipes, *Trans. ASCE*, 47 (1902), pp. 1-196.
- [2] Eustice, J., Flow of water in curved pipes, *Proceeding of Royal Society of London A*. 1910, Vol. 84, pp. 107-118.
- [3] Eustice, J., Experiments on stream-line motion in curved pipes, *Proceeding of Royal Society of London A*. 1911, Vol. 85, pp. 109-131.
- [4] Eustice, J., Flow of fluids in curved passages, *Engineering*, Nov. 13 (1925), pp. 604-605.
- [5] Dean, W. R., Note on the Motion of Fluid in a Curved Pipe, *Philosophical Magazine and Journal of Science*, 4 (1927), 20, pp. 208-223.
- [6] Dean, W. R., The Stream-line Motion of Fluid in a Curved Pipe, *Philosophical Magazine and Journal of Science*, 5 (1928), 30, pp. 673-695.
- [7] Dennis, S. C. R., Ng, M., Dual solutions for steady laminar flow through a curved tube, *Quarterly Journal of Mechanics and Applied Mathematics*, 35 (1982), pp. 305-324.
- [8] Nandakumar, K., Masliyah, J. H., Bifurcation in steady laminar flow through curved tubes, *Journal of Fluid Mechanics*, 119 (1982), pp. 475-490.
- [9] Daskopoulos, P., Lenhoff, A.M., Flow in curved ducts: bifurcation structure for stationary ducts, *Journal of Fluid Mechanics*, 203 (1989), pp. 125-148.
- [10] Cheng, K. C., Mok, S. Y., Flow visualization studies on secondary flow patterns and centrifugal instability phenomena in curved tubes, *Fluid Control Measurement*, 2 (1986), pp. 756-773. *Quarterly Journal of Mechanics and Applied Mathematics*, 35 (1982), pp. 305-324.
- [11] Kao, H. C., Some aspects of bifurcation structure of laminar flow in curved ducts, *Journal of Fluid Mechanics*, 243 (1992), pp. 519-539.
- [12] Yanse, S., Goto, N., Yamamoto K., Stability of dual solutions of the flow in a curved circular tube, *Journal of the Physical Society of Japan*, 57 (1988), pp. 2602-2604.

AN EXPERIMENTAL STUDY OF TEMPERATURE FIELD OF NON-ISOTHERMAL CO-AXIAL FREE JETS

Mohammad Nasim Hasan¹ and M. A. Taher Ali²

¹ Assistant Professor, Department of Mechanical Engineering, BUET, Dhaka-1000

² Professor, Department of Mechanical Engineering, BUET, Dhaka-1000

nasim@me.buet.ac.bd

ABSTRACT

The present study is concerned with the experimental investigations of mean temperature field that develops in the mixing zone of non-isothermal co-axial free jets. Non-isothermal co-axial jet flows have been developed by issuing two air jets with different unidirectional velocities and temperature from a concentric compound nozzle. The hot central air jet comes out from a 29 mm central nozzle while the annular ambient air jet is emitted through the annular space between the 80 mm. outer nozzle and the central nozzle. The annular to central jet area ratio of co-axial jets is 6.6. Four outer to inner jet velocity ratios ranging from 0.0 to 0.75 have been considered and for each flow configuration two different values of the inner jet temperature were used. Measurements of temperature are made in the mixing zone of the compound jets with the help of thermocouple embedded at the tip of a 3 mm OD pitot static tube for two different Reynolds numbers of 3.72×10^4 and 4.80×10^4 based on the velocity and diameter of the inner jet. From the measurements, the thermal field associated with the of mixing non-isothermal jets is ascertained and many of its aspects like exit temperature profile, centerline temperature profile, streamwise temperature profile as well as the spread of jet thermal field have been analyzed for different upstream conditions of the jets. The results indicate that thermal diffusion from the hot central jet occurs more rapidly at lower velocity ratios of co-axial jets. With the increase of velocity ratio, the thermal potential core is noted to be transversely shrunk but longitudinally elongated. The thermal field of non-isothermal jets is observed to spread more at higher temperature gradient while its presence is noticed to extend in further downstream locations at higher Reynolds number of the jet.

Keywords: *Non-isothermal co-axial free jets, Thermal potential core, Thermal half-width, Spread of jets temperature field.*

1. INTRODUCTION

Fluid Jets constitute omnipresent phenomena in nature as well as in different industrial applications. Some of these are obvious to even the most casual observer— like the jets which exit from one's mouth when exhaling in a cold morning, while others may require extraordinary efforts to be seen—like astrophysical jets at distances of light years away visible only through telescopes. The jet technology

dominate our lives from propelling the aircrafts which move us across the continents to providing the simple air hoses of the machine shop, from the stacks which spew the waste products of the industry to the diffuser arrays which disperse effluent into our streams and rivers.

The extensive use of turbulent jets in different engineering arena attracts the attention of the researchers from 1950's. Frostal [1], Stark [2] and Chigier [3] made their study on the mixing of a circular jet with an annular co-axial jet for various area ratios as well as velocity ratios of the jets. For measurement they used Pitot tube and their result proved that the nozzle diameters i.e. area ratios and velocity ratios were the most important parameters which determined the jet configuration and average velocity profile of the flow. Champagne and Wygnanaski [4] were the first to use hot wire anemometer in their study of turbulent co-axial jet's research. In their study, two different nozzle configurations having outer to central area ratios of 0.94 and 1.28 have been used for various velocity ratios ranging from 0 to 10. In contrast to what Frostal and Shapiro [1] announced, Champagne and Wygnanaski showed that jet half width ($y_{0.5}$) is not very sensitive to velocity ratio and area ratio. According to them, the length of inner potential core of co-axial jets is strongly dependent on both the velocity ratio as well as area ratio while that of the outer potential core is more or less independent of velocity ratio.

Using hot wire anemometry, Ko and Kwan [5] found out pressure fluctuations and velocity fluctuations in the initial and developed regions of co-axial jets. From their results, they concluded that co-axial and simple jet's structures are coherent and physically similar in the developed region of the flow field. Based on experimental study, Ko and Au [6] divided the whole flow field of co-axial jets in to three separate regions: the initial region, the intermediate region and the developed region. The initial region is located between the nozzles and the end of outer potential core, immediately downstream is the intermediate region which ends at the reattachment point. From this point the flow behaves like a single jet resulting from only one nozzle and essentially it is the developed region of jet flow field where the flow variables attain a self-preservation state.

Ribeiro [7] experimentally studied mean velocity, Reynolds stresses and probability density distribution of fluctuating velocity of axisymmetric turbulent co-axial jets, with or without swirl. According to his findings, the presence of swirl in co-axial jets results in earlier attainment of self-preservation state of jets. Rehab et al. [8] used hot-wire anemometry to study the structure of turbulent co-axial jets with outer to central jet velocity ratios (r) greater than 1. Two flow regimes were identified depending on whether the velocity ratio (r) is greater than a critical value (r_c). When $r < r_c$ the faster annular jet periodically pinches the central jet and the pinching frequency corresponds to the outer jet mode. When $r > r_c$ the inner potential core is truncated and followed by an unsteady recirculation zone.

This bibliographical review of co-axial jets shows that almost all the earlier experimental research works have been done with isothermal consideration. But mixing of fluids at different temperature in the form of co-axial jets is also very common in many technical applications. For example, mixing of hot combustion products with secondary cooling air in the combustion chamber of gas turbine basically represents a flow case similar to non-isothermal co-axial jets. Similar type of flow is also found in different chemical process industries and Effluent Treatment Plant (ETP) where fluid reactants at different temperature get mixed essentially in the form of co-axial jets. The present research work is aimed to determine the temperature field that results in due to the interaction of non-isothermal co-axial jets as well as its dependency over different dynamical conditions of jets.

2. EXPERIMENTAL METHOD

2.1 Co-axial Jet Flow Facility

A schematic diagram of the co-axial jet flow system is illustrated in Figures [1-2]. The co-axial jet flow system has been developed by adding a central circular air flow system in the existing jet flow facility in the laboratory. The jet flow facility has overall length of 8.1 m having 80 mm diameter exit nozzle. In the delivery side of the flow facility the diameter of pipe is reduced in two stages from 475 mm to 80 mm where the experimental nozzle is fitted. A centrifugal blower is placed below the main flow system to supply air to the central nozzle. The 100 mm discharge line of this blower is connected to a 3.5 kW air heating system. A 62 mm PVC pipe is connected to the delivery side of the air heating system that enters radially in to the 2nd settling chamber of the main flow system. In order to place the central nozzle along the

central axis of 80 mm nozzle 3 sets of centralizers have been placed in three different locations. Finally, the exit diameter of the central nozzle is reduced to 29 mm through 100 mm×29 mm reducer. The flow straightener and wire screens are present in both jets to straighten the flow as well as to break down large eddies present in the air flow. To minimize the effect of any boundary on the jet flow, the nozzle centerline is set at 1400 mm above the ground.

Throughout the study, nozzle exit center is taken as the origin. The center line of the nozzle in the direction of flow is taken as positive x-axis and radial distance pointing upwards as positive y-axis and the axis 90° anticlockwise from positive x-axis is considered as the positive z-axis as shown in Fig. [3].

2.2 Instrumentation

The experiments involve measurements of temperature at different grid points of the jet flow field. Measurements of temperature in different locations of the jet flow field is made by using a T-type thermocouple embedded at the tip of a 3 mm OD Pitot-static tube [United Sensor]. The thermo-electric signal of the thermocouple is recorded by using a temperature controller. The the Pitot -static tube as well as the thermocouple is traversed in the jet field with the help of a Mitutoyo (Japan) coordinate measuring machine (type: CS 652). This traversing mechanism is placed on a hydraulically operated table, which 900 mm away from the nozzle axis to avoid any possible disturbances.

2.3 Data Analysis and Calculation

All the measurements points are made non-dimensional by dividing the distances along y-axis (y) with either inner nozzle diameter (d) or axial distance (x). The local temperature of jet field T (K) is also made non-dimensional temperature variable (θ) according to the relation:

$$\theta = \frac{T - T_2}{T_1 - T_2}$$

Where T (K) is the local temperature of jet flow field, T_1 (K) is the mean temperature of hot central jet and T_2 (K) is that of ambient annular jet or surroundings. The growth of jet thermal field is analyzed in terms of thermal half width ($y_{0.5}$). To get a better understanding of the evolution of temperature field in streamwise direction, a special form of graphs is plotted in the axes of θ vs. y/x .

3. RESULTS AND DISCUSSION

Mean temperature field of non-isothermal co-axial jets have been investigated for different upstream conditions in the present investigation. The annular to central jet velocity ratio (U_2/U_1) is varied as 0.0, 0.25, 0.50 and 0.75 for nozzle configuration having annular to central area ratio of 6.6. Two different annular to central jet temperature ratios (T_2/T_1) have been considered in each case as 0.974 and 0.925 on the basis of absolute temperature scale. Considering the central jet as the primary one, the Reynolds number has been calculated on the basis of the velocity and diameter of the central jet. Two different values of Reynolds number are taken in to consideration as 3.72×10^4 and 4.80×10^4 . The summary of this experimental work are explained below.

3.1 Exit Temperature Profile

Exit temperature profiles of a non-isothermal 29 mmD single jet ($U_2/U_1 = 0.0$) and thermally stratified co-axial jets ($A_2/A_1 = 6.6$, $U_2/U_1 = 0.25$) are shown in Figure 3 for temperature ratio (T_2/T_1) of 0.925 and Reynolds number $Re = 3.72 \times 10^4$. In case of co-axial jets, the temperature near the boundary of the central jet is found to decrease more rapidly than that of single jet. This is due to the fact that, the flow of the annular jet in case of co-axial jets takes away larger amount of heat from the hot central jet during its journey from the heating chamber to the nozzle exit. Thereby the size of the thermal potential core at the nozzle exit reduces in non-isothermal co-axial jets.

3.2 Centerline Temperature Profile

The centerline mean temperature of non-isothermal jet flows is one of the most important parameters that reveal different important aspects of the thermal field of non-isothermal jets like thermal core length,

diffusion mixing amongst the fluid streams etc. In the current investigation the centerline temperature of the jet is expressed as:

$$\theta_c = \frac{T_c - T_2}{T_1 - T_2}$$

Where, θ_c = Non-dimensional temperature variable, T_c = Centerline temperature (K), T_1 = Mean temperature of the central/ inner jet (K), T_2 = Mean temperature of annular jet/ surroundings (K).

Figure 4 illustrates the centerline temperature profiles of a non-isothermal single jet and that of co-axial jets ($A_2/A_1 = 6.6$, $U_2/U_1 = 0.25$) with $T_2/T_1 = 0.974$ and $Re = 3.72 \times 10^4$. In this figure non-isothermal co-axial jets are found to have a relatively longer thermal potential core than that of the single jet. This is because the presence of annular jet in the case of co-axial jets not only retards the growth of shear layer to provide a relatively longer dynamical potential core of the central jet but also suppresses the diffusion activities of the central hot jet thereby resulting in longer thermal potential core in the downstream direction.

The effect of Reynolds number (Re) on the centerline temperature decay of non-isothermal single jet is shown in Figure 5 for temperature ratio of 0.974. In both the cases, the length of thermal potential core is found to be the same but rapid decay of the centerline temperature is noted at lower Reynolds number. This indicates that high inner jet velocity carries its temperature field further downstream from the nozzle exit.

The velocity ratio of co-axial jets (U_2/U_1) also plays an important role in determining the centerline temperature decay in the developed zone of the jet field as shown in Figure 6. From this figure it is found that, the length of thermal potential core is more or less insensitive to the velocity ratio (U_2/U_1). However, beyond the thermal potential core the centerline temperature is found to decrease faster at lower velocity ratios. This may be due to rapid mixing of the fluid streams at lower velocity ratios of co-axial jets in the developed zone.

3.3 Streamwise Temperature Profile

Figure 7 and 8 illustrate the streamwise temperature profiles of a non-isothermal single jet at $Re = 3.72 \times 10^4$ for $T_2/T_1 = 0.974$ and 0.925 respectively. As a result of thermal diffusion and mixing of hot jet with the surrounding ambient fluid, the thermal potential core is found to shrink gradually in the downstream direction. In both the cases the thermal potential core is found to extend up to $x/d = 4.0$. The streamwise temperature profiles of the single jet at $T_2/T_1 = 0.925$ (figure 9) is found to be smooth while that for $T_2/T_1 = 0.974$ (figure 8) is found to show some sort of thermal stratification. This may be due to irregular thermal diffusion at low temperature ratio as well as the thermal lag of the temperature measurement system.

A comparison of streamwise temperature distributions between non-isothermal single jet and co-axial jets ($A_2/A_1 = 6.6$, $U_2/U_1 = 0.25$) can be made from Figure 9. In case of non-isothermal single jet the heat diffuses to the surroundings more rapidly than co-axial jets thereby causing the temperature of the fluid in the vicinity of the nozzle boundary to increase more rapidly as compared to co-axial jets. Moreover, the temperature near the jet axis is found to diminish more rapidly in case of the single jet than that of the co-axial jets. This phenomenon may be the consequence of rapid diffusion and mixing that takes place in case of single jet. From the distributions of isotherms, it becomes evident that a narrow and relatively longer potential core is found in non-isothermal or thermally stratified co-axial jets while that of non-isothermal single jet is found to be thick and shorter.

The effect of velocity ratio (U_2/U_1) on the streamwise temperature distribution of non-isothermal co-axial jets ($A_2/A_1 = 6.6$, $U_2/U_1 = 0.50$ and $T_2/T_1 = 0.925$) is presented in Figure 10 for Reynolds number of 3.72×10^4 . With the increase of velocity ratio, the thermal field of the jets is found to be squeezed as shown in this figure. As the velocity ratio increases, the momentum flux through the annular jet also increases which in turn suppresses the thermal diffusion activities of the central hot jet thereby decreasing the width of the thermal field. At higher temperature gradient, the thermal field of non-isothermal jets is found to be large, well shaped and less distorted as shown in Figure 11. This is due to the enhanced heat transfer from the hot jet at higher temperature gradient which also results in enlarged thermal field.

3.4 Isothermal Lines

A comparison of the propagation of isotherms ($\theta = 0.1, 0.3, 0.5, 0.7$ and 0.9) of a non-isothermal single jet and co-axial jets ($A_2/A_1 = 6.6, U_2/U_1 = 0.50$) is made in Figure 12 for a temperature ratio $T_2/T_1 = 0.925$ at $Re = 3.72 \times 10^4$. From this figure it is clear that the thermal field of a non-isothermal single jet spreads more rapidly than that of co-axial jets. This is due to the fact that the annular flow of co-axial jets impedes the thermal diffusion from the hot central jet and the thermal field is found to reside within the confines of the central jet. This results in the flatter isothermal curves in case of non-isothermal co-axial jets as compared to that of the single jet.

3.5 Spread of Jet Thermal Field

The term thermal half-width is used to characterize the growth of the thermal field of non-isothermal jets in the present study. It is defined as the distance ($y_{10.5}$) measured from the centerline of the jet, where the local mean temperature (T) is equal to half of the local centerline mean temperature (T_c).

Figure 13 describes the effect of temperature ratio (T_2/T_1) on the growth of thermal half-width of a non-isothermal single jet at Reynolds number 3.72×10^4 . A higher value of thermal half-width ($y_{10.5}$) is obtained in all axial locations for larger temperature gradient i.e. lower value of T_2/T_1 . This is due to more thermal diffusion that occurs at higher temperature gradient between the hot jet and cold surroundings.

A comparison of the propagation of thermal half-width ($y_{10.5}$) of non-isothermal single jet and that of non-isothermal co-axial jets ($A_2/A_1 = 6.6$) at different velocity ratios can be made from Figure 14. For single jet, the thermal diffusion and bulk mixing of hot jet with the surroundings causes the thermal half-width to grow up in the developed zone of the jet just after the potential core ($x/d > 4.0$). But in the case of co-axial jets, the flow of the annular jet suppresses the diffusion activities from the hot central jet thereby retards the growth of thermal half-width. With the increase of velocity ratio, the degree of suppression of thermal diffusion also increases. As a result, the thermal half-width is found to assume lower value in any particular downstream location at higher velocity ratio of co-axial jets.

4. CONCLUSION

From this experimental work regarding non-isothermal co-axial jets the following conclusions can be drawn:

- i. Similar to dynamic potential core, the flow field of non-isothermal jets also possesses a thermal potential core. The length of this thermal potential core is found to be larger in co-axial jets than that in single jet.
- ii. The centerline temperature of non-isothermal single jet is found to decrease faster than that of non-isothermal co-axial jets. With the increase of velocity ratio of non-isothermal co-axial jets, the centerline temperature is found to decay at slower rate.
- iii. Thermal diffusion of non-isothermal single jets occurs more rapidly than that of co-axial jets. With the increase of velocity ratio of non-isothermal co-axial jets, the associated thermal field is found to shrink. Higher temperature gradient amongst the fluid streams results in an enlarged thermal field.

5. NOMENCLATURE

Symbol	Meaning	Symbol	Meaning
d	Diameter of inner nozzle	T_c	Centerline jet temperature
d_o	Diameter of outer nozzle	$\theta = \frac{T - T_2}{T_1 - T_2}$	Non-dimensional local temperature
Re	Reynolds number	$\theta_c = \frac{T_c - T_2}{T_1 - T_2}$	Non-dimensional centerline temperature
U_1	Mean velocity of central jet	$A_1 = \pi d^2/4$	Area of the central nozzle
U_2	Mean velocity of annular jet	$A_2 = \pi (d_o^2 - d^2)/4$	Area of the annular nozzle

T_1	Mean temperature of central jet	L_{tp}	Length of thermal potential core
T_2	Mean temperature of annular jet/ surrounding	$y_{0.5}$	Thermal half width
T	Local temperature		

6. REFERENCE

1. Frostall, W. and Shapiro, A. H., "Momentum and Mass Transfer in Co-axial Gas Jets", Trans. ASME Vol. 73, pp. 219, 1951.
2. Stark, S. B., "Mixing of Gas Stream in a Flame", Zh Tech Vol. 23, pp.1802-1819
3. Chigier, N. A. and Beer, J. M., "The Flow Region near the Nozzle in Double Concentric Jets", Journal of Basic Engineering, pp. 797-804, 1964.
4. Champagne, F. H., and Wygnanski, I. J., "An Experimental Study of Co-axial Turbulent Jet", International Journal of Heat and Mass Transfer, Vol. 14, pp. 1445-1464, 1971.
5. Ko, N. W. M and Kwan A. S. H "The Initial Regions of Subsonic Co-axial Jets", Journal of Fluid Mechanics, Vol. 73, pp. 305-322, 1976.
6. Ko, N. W. M and Au. H., "The Initial Regions of Subsonic Co-axial Jets of High Mean Velocity Ratio", Journal of Fluid Mechanics, Vol. 73, pp. 305-322, 1976.
7. Ribeiro, M. M. and Whitelaw, J. H., H "Co-axial Jets with or without Swirl", Journal of Fluid Mechanics, Vol. 96 Part 4, pp. 769-795, 1980.
8. Rehab, H., Villermaux, E. and Hopfinger, E. J., "Flow Regimes of Large Velocity Ratio Co-axial Jet", Journal of Fluid Mechanics, Vol. 345, pp. 357-381, 1997.

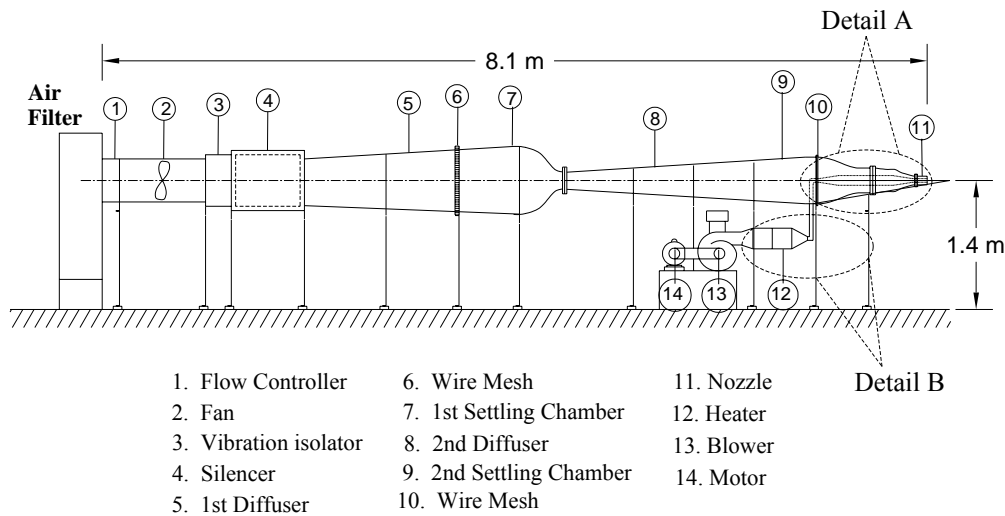


Figure 1: Schematic Diagram of the Jet Flow Facility

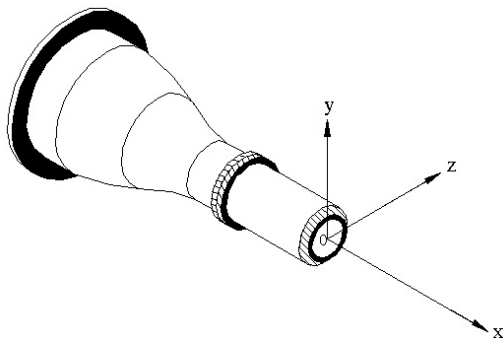


Figure 2: Co-ordinate System of Nozzle

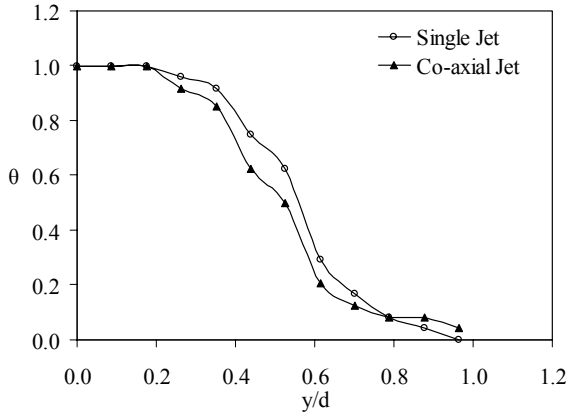


Figure 3: Exit ($x/d = 0.0$) Temperature profiles of Non-isothermal Single Jet ($U_2/U_1 = 0.0$) and Co-axial Jets with $T_2/T_1 = 0.925$ at $Re = 3.72 \times 10^4$.

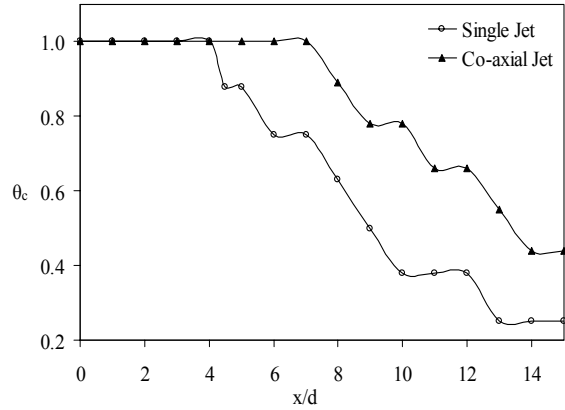


Figure 4: Centerline Temperature Profiles of Non-isothermal Single Jet ($U_2/U_1 = 0.0$) and Co-axial Jets at with $T_2/T_1 = 0.974$ at $Re = 3.72 \times 10^4$.

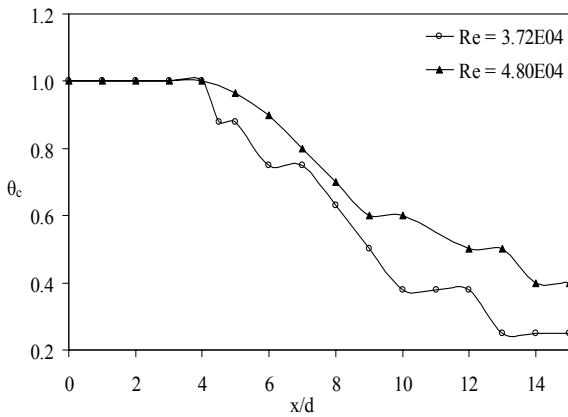


Figure 5: Effect of Reynolds No. on Centerline Temperature Profile of Non-isothermal Single Jet at $T_2/T_1 = 0.974$.

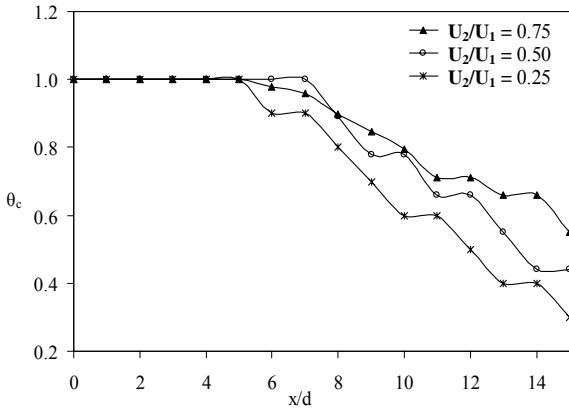


Figure 6: Effect of Velocity Ratio on Centerline Temperature Profiles of Non-isothermal Co-axial Jets at $Re = 3.72 \times 10^4$ with $T_2/T_1 = 0.974$.

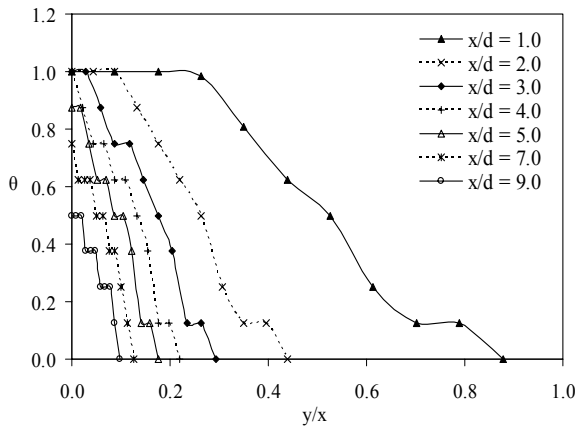


Figure 7: Streamwise Temperature Profiles of a Non-isothermal Single Jet at $Re = 3.72 \times 10^4$ with $T_2/T_1 = 0.974$.

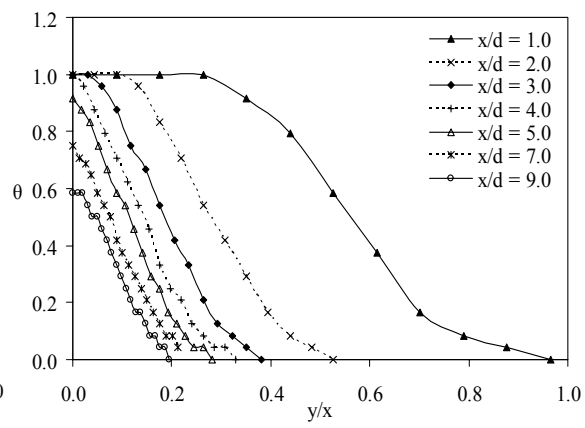


Figure 8: Streamwise Temperature Profiles of a Non-isothermal Single Jet at $Re = 3.72 \times 10^4$ with $T_2/T_1 = 0.925$.

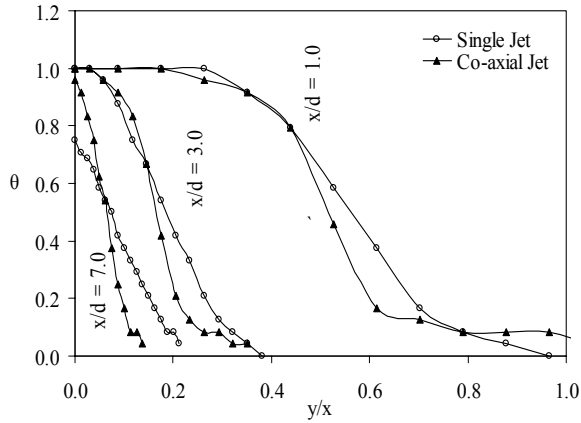


Figure 9: Comparison of Streamwise Temperature Profiles of Non-isothermal Single Jet and Co-axial Jets ($A_2/A_1 = 6.6$, $U_2/U_1 = 0.50$) at $Re = 3.72 \times 10^4$ with $T_2/T_1 = 0.925$.

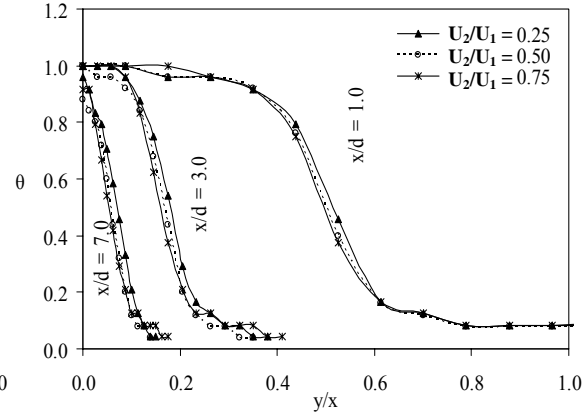


Figure 10: Effect of Velocity Ratios on Streamwise Temperature Profiles of Non-isothermal Co-axial ($A_2/A_1 = 6.6$) at $Re = 3.72 \times 10^4$ with $T_2/T_1 = 0.925$.

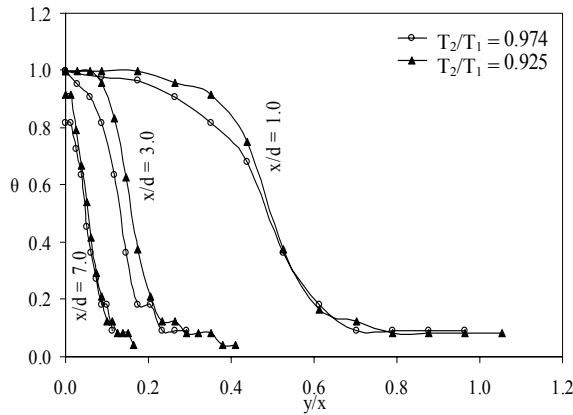


Figure 11: Effect of Temperature Ratios on Streamwise Temperature Profiles of Non-isothermal Co-axial Jets ($A_2/A_1 = 6.6$, $U_2/U_1 = 0.75$) at $Re = 3.72 \times 10^4$.

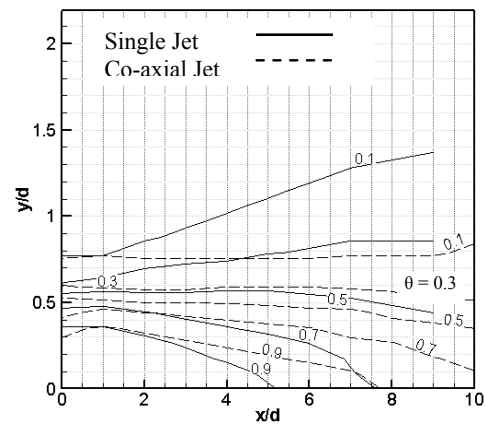


Figure 12: Comparison of Isotherms of a Non-isothermal Single jet and Co-axial Jets ($A_2/A_1 = 6.6$, $U_2/U_1 = 0.50$) at $Re = 3.72 \times 10^4$ with $T_2/T_1 = 0.925$.

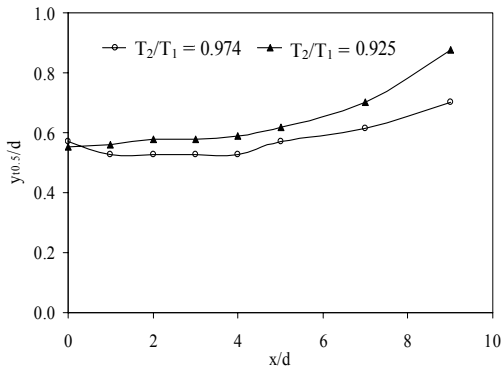


Figure 13: Effect of Temperature Ratio on the Propagation of Thermal Half-width ($y_{0.5}$) of a 29 mmD Non-isothermal Single Jet at $Re = 3.72 \times 10^4$.

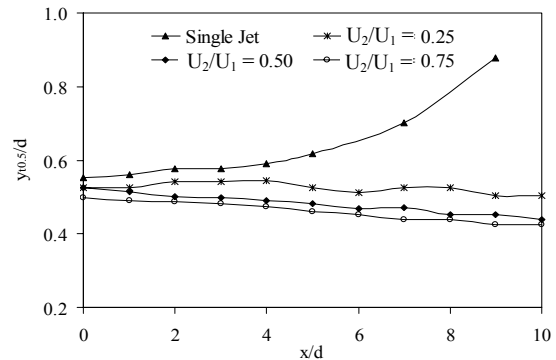


Figure 14: Effect of Velocity Ratio on the Propagation of Thermal Half-width ($y_{0.5}$) of Non-isothermal Co-axial Jets ($A_2/A_1 = 6.6$) with $T_2/T_1 = 0.925$ at $Re = 3.72 \times 10^4$.

PREDICTION OF FRICTION FACTORS FOR U-TYPE WAVY TUBES

Salah Uddin Ahmed Hamim, Ashif Khan and M. Mahbubur Razzaque

Department of Mechanical Engineering, BUET
Dhaka – 1000, Bangladesh.
Email: hamim.buet@gmail.com

ABSTRACT

Experiments are done with water to determine friction factors for small diameter copper tubes of U-type wavy configuration. In one set of tests, the number of bends is varied (9, 11, 13 and 15) and in the other set, the inner diameter is varied (3.9, 4.85 and 7.9 mm). In these tests, the range of Reynolds number is 4000 to 30,000. The range of the dimensionless curvature ratio ($2R/D$) is 6.43 - 13.03 and of the dimensionless spacer length (L/D) is 3.16 - 6.41. An equivalent bend friction factor is defined considering only the pressure drop due to a bend. A generalized correlation considering the effects of dimensionless curvature ratio, dimensionless spacer length and number of bends has been developed, which, in the limiting condition, reduces to Blasius equation for straight smooth tubes. Predicted friction factors are in good agreement with the experimental data.

Key words: Bend friction factor, Relative friction factor, U-type wavy tubes, Single phase flow.

1. INTRODUCTION

U-Type wavy tubes are utilized in a great number of heat transfer equipment and flow transmitting devices such as shell and tube heat exchangers in domestic and industrial water heating systems, plate solar collectors, steam generators and superheaters in nuclear power plants and continuous chemical reactors in chemical industries. U-Type wavy tubes usually consist of 180° bends with the end of a bend connected to the starting of another bend through a straight section known as spacer forming a periodic pattern. The dynamic similarity of the flow through a bend depends on a non-dimensional parameter, D_n called the “Dean Number” [1-3]

$$D_n = \frac{2rV}{\nu} \sqrt{\frac{r}{R}} = Re \sqrt{\frac{r}{R}} \quad (1)$$

Here ‘Re’ is the Reynolds number, ‘V’ is the mean velocity along the tube, ‘ ν ’ is the coefficient of kinematic viscosity, and ‘ $2r$ ’ is the diameter of the tube which is bent into an arc of radius ‘R’. The relative friction factor defined as the ratio of bend friction factor to straight friction factor depends only on ‘ D_n ’, as long as the flow is laminar.

Flow in a wavy tube approaching a consecutive bend is much more complex. Pressure losses in the flow are a result of the very complex velocity gradient distribution and friction at the tube wall and of the dissipation of energy of the vortex pairs produced by each consecutive bend. Popiel and Wojtkowiak [4] studied this type of flow in the laminar regime and proposed the following correlation for Darcy friction factor, f_D for bend.

$$\ln\left(\frac{f_D Re}{64}\right) = 0.021796 + 0.0413356(\ln D_n)^2 \quad (2)$$

Later, Wojtkowiak studied the effects of the length of the straight section or the spacer between two consecutive 180° bends and proposed a new correlation as given below.

$$f_D = a + b \ln D_n + \frac{c}{D_n} \quad (3)$$

Where, $a = 0.121433 - 0.00182313(L/D)$, $b = -0.010311 + 0.0001936(L/D)$ and $c = 16.68855 - 0.16757(L/D)$. However, Chen et al. [5] reported that the two correlations mentioned above do not match with some new experimental data. They proposed a better correlation shown in equation (4), which is able to predict their own experimental data as well as the data of Popiel and Wojtkowiak [4] for Fanning friction factor, f_B for bend.

$$\frac{Re}{16} f_B = \left[1 + 29e^{\left(\frac{-2R}{D}\right)} \right] \times \exp \left\{ 0.07 + 0.04 \ln(Dn)^2 + \left(\frac{L}{D}\right) \left[0.36 - 0.035 \ln(Re)^{0.9} - 0.145 \left(\frac{L}{D}\right)^{2.5} + 0.005 \left(\frac{L}{D}\right)^3 \right] \right\} \quad (4)$$

All the above-mentioned studies of flows through U-type wavy tubes are in the range of $Re = 200 \sim 18000$, which covers mostly laminar and transition regimes of flow. None of them considered the case of fully turbulent flow and the effect of number of bends. Moreover, as the spacer length is increased the prediction becomes poor and in the limiting case of straight tubes ($L/D = \infty$), the friction factor predicted by equation (4) is infinite, which is completely unacceptable.

Therefore, the purpose of this paper is report the progress of an ongoing work to develop a correlation considering the effects of number of bends (n), curvature ratio ($2R/D$) and dimensionless spacer length (L/D) on single-phase turbulent flow inside U-type wavy tubes, which reduces to Blasius Equation, in the limiting case of straight tubes.

2. TEST FACILITY AND EXPERIMENTAL METHOD

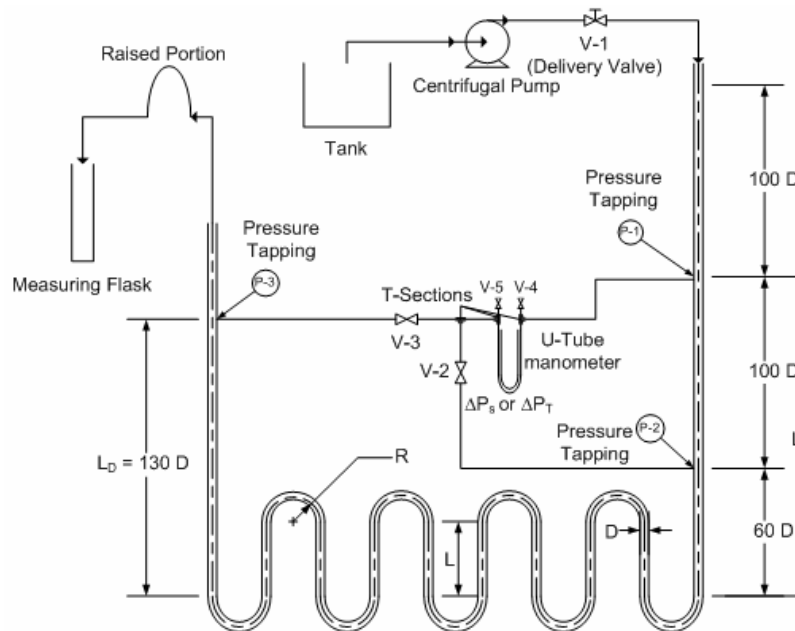


Fig – 1. Schematic Diagram of the setup

The schematic diagram of the setup is shown in Fig.1. The test sections made of copper tubes were carefully checked to ensure that they have uniform diameter along the length. The tests were carried out in two sets. In one set, the tube diameters were varied ($D = 3.9, 4.85$ and 7.9 mm) and the number of bends ($n = 15$), bend radius ($R = 25.4$ mm) and spacer length ($L = 25$ mm) were kept constant. The corresponding curvature ratio and the Dimensionless Spacer Length are shown in Table 1.

Table 1: Test section details for the effects of $2R/D$ and L/D

Tube diameter, D , mm	Curvature ratio, $2R/D$	Dimensionless spacer length, L/D
3.9 ± 0.01	13.026	6.41
4.85 ± 0.01	10.47	5.15
7.9 ± 0.01	6.43	3.16

To investigate the effect of number of bends, four different bend numbers ($n = 9, 11, 13$ and 15) are tested, while keeping other parameters constant, namely, tube diameter, $D = 7.9 \pm 0.01$ mm, bend radius, $R = 25.4$ mm, spacer length, $L = 25$ mm, curvature ratio, $2R/D = 6.43$ and dimensionless spacer length, $L/D = 3.16$.

In each of the test sections, the entry length is kept greater than $100D$ to ensure a fully developed flow before it reaches the first pressure tapping, P-1. At $100D$ downstream of the pressure tapping P-1 the second pressure tapping P-2 is provided. The fanning friction factor for the straight section is determined from the pressure drop between P-1 and P-2. Downstream of the bends the distorted flow condition persists for some distance beyond which the pressure gradient becomes steady and presumably the same as that of the upstream. For this reason, the third pressure tapping, P-3 is located at a distance of about $130D$ downstream of the bend. The pressure drop between P-1 and P-3 is composed of the pressure drops both in the straight and bent sections.

2.1. Bend friction factor, f_B

The pressure drop due to a single bend is calculated by subtracting the straight section pressure drop from the measured total pressure drop. Then the equivalent bend friction factor, f_B is defined as

$$f_B = \frac{\Delta P - 2f_p V^2 \frac{L_t}{D}}{2\rho V^2 \frac{L_c}{D}} \quad (5)$$

Here, f is the Fanning friction factor for the straight section, ' V ' is the mean axial velocity and L_t = length of the total straight portion in the test section, i.e. straight portion in the upstream, L_U + straight portion in spacer, L_L + straight portion in the downstream, L_D . If ' n ' is the number of bends and L is the length of a single spacer then, $L_L = (n-1)L$ and $L_c = n\pi R$.

The maximum overall uncertainty [6] in the measurement of bend friction factor f_B is $\pm 7\%$ for $Re \approx 20000$ and $\pm 4.3\%$ for $Re \approx 2000$.

3. RESULTS AND DISCUSSION

In Fig. 2, the experimentally determined values of the Fanning friction factor, f are plotted against Reynolds number, Re for tube diameter, $D = 7.9$ mm with three different values of number of bends. The curvature ratio, $2R/D$ and the dimensionless spacer length, L/D are kept fixed at 6.43 and 3.16 , respectively. The solid line is the plot of the Blasius equation for turbulent flow through a hydrodynamically smooth tube. The black symbols are

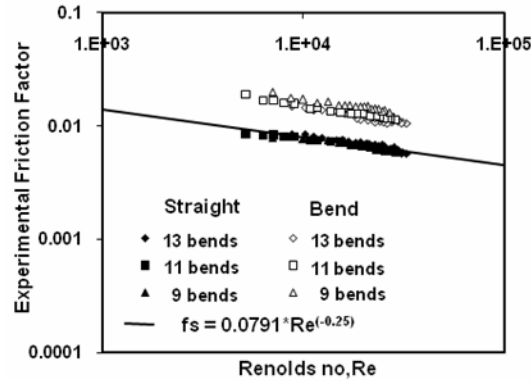


Fig 2: Variation of Fanning friction factor for straight tubes and Bend friction factor for wavy tubes with Reynolds number, Re ($D = 7.9$ mm, $2R/D = 6.43$ and $L/D = 3.16$).

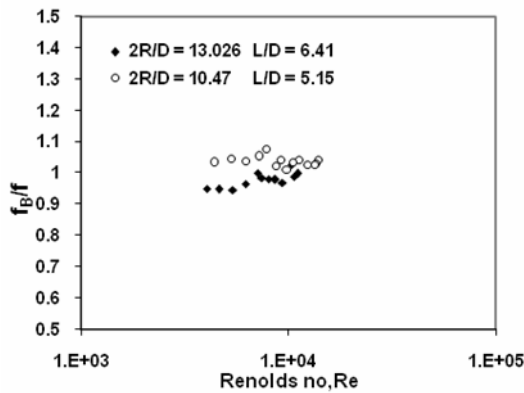


Fig 3: The relative friction factor, f_B/f vs Reynolds number, Re. (for 15 bends and large $2R/D$ and L/D).

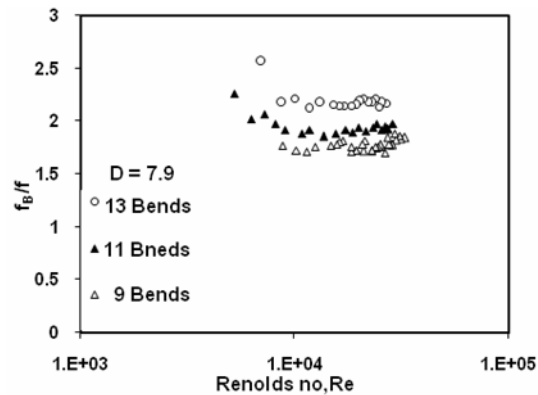


Fig 4: The relative friction factor, f_B/f for different number of bends. ($2R/D = 6.43$ and small $L/D = 3.16$)

the experimental Fanning friction factor for the straight sections whereas the white symbols are the bend friction factors for the bends. It is evident that the experimental Fanning friction factor, f for the straight sections agrees favorably with the Blasius line. This good agreement illustrates the accuracy of the experimental setup and procedure. Bend friction factor, f_B is significantly higher than the corresponding Fanning friction factor and depends weakly on the number of bends (n).

The relative friction factors f_B/f for 15 bends are shown in Fig. 3 for the tube diameters of 3.9 mm and 4.85 mm. It is evident that the relative friction factor is considerably higher with smaller curvature ratio and smaller dimensionless spacer length. This is mostly caused by the secondary flow, which increases the disturbance in flow in the curved tubes. However, the influence of the curvature ratio and dimensionless spacer length seems to minimize with the increase of Reynolds number and for $Re \geq 4000$, the relative friction factors for both curvature ratios are approximately close to 1.0. However, throughout the range of Reynolds number investigated, with the smaller curvature ratio and the smaller dimensionless spacer length, the relative friction factor is higher. With further decrease in the curvature ratio and spacer length, the relative friction factor increases and shows strong dependence on the number of bends as shown in Fig. 4.

According to Popiel and Wojtkowiak [4], the effect of laminar secondary flow and the developing Dean vortices on the pressure losses is gradually replaced by the turbulent secondary flow as the Reynolds number is increased. Larger spacer length may relax the

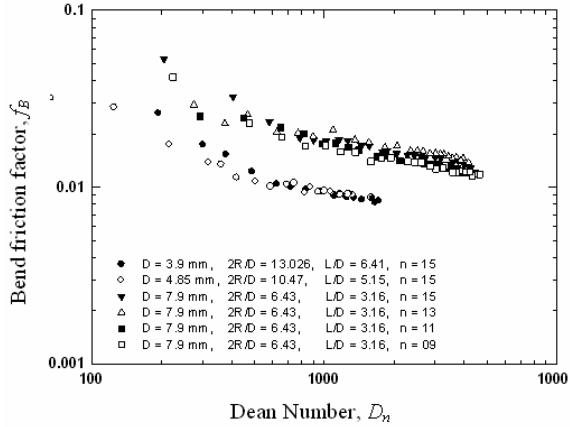


Fig 5: Bend friction factor, f_B vs Dean No., D_n for all experimental data.

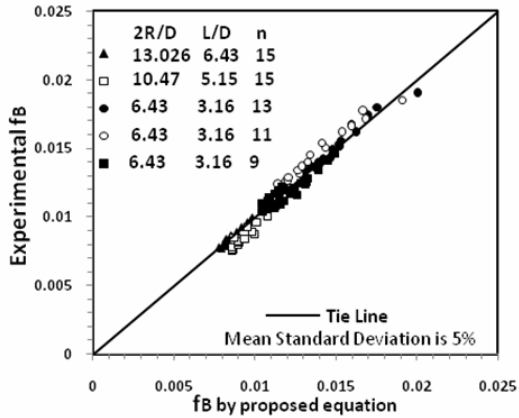


Fig. 6: Bend friction factor, f_B Experimental data and Predictions by the proposed correlation.

strength of vortical motion of the swirled flow passing the bend. Therefore when the dimensionless spacer length increases, the overall flow in the recovery region becomes more uniform leading to a lower friction factor in the system.

In Fig. 5, the bend friction factor, f_B is plotted against Dean number, D_n , which shows that for Dean Number >1000 , the data maintain a linear relationship. Based on this observation, a correlation is proposed which includes the effect of Dean number (D_n), dimensionless spacer length (L/D) and number of bends (n), which will give identical results to Blasius equation when $L/D = \infty$. The correlation is given below.

$$f_B = f \left[1 - A n^{1.13} e^{-B \frac{L}{D}} \left\{ D_n - C \left(\frac{L}{D} \right)^{-2.47} \right\} \right] \quad (6)$$

$A=0.000086$, $B=1.2$ and $C=595300$. In this correlation, the curvature is not considered a separate parameter as it is closely related to Dean number. Figure 6 shows that the predictions of f_B by the proposed correlation are in good agreement with the experimental data. The correlation is valid for Reynolds number, $Re= 4000-32000$, Curvature ratio, $2R/D = 6.43-13.026$, Dimensionless spacer length, $L/D = 3.16-6.41$ and number of bends, $n = 9-15$.

4. CONCLUSIONS

The salient points of this study may be recapitulated as follows:

i) The relative friction factor, f_B/f increases considerably with the decrease of curvature ratio ($2R/D$) and dimensionless spacer length (L/D) and increases slightly with number of bends.

ii) Existing correlations are unable to predict acceptable friction factor for large values of the dimensionless spacer length and for turbulent flow. The effects of number of bends were not considered in those correlations.

iii) The proposed correlation agrees with the present experimental data within $\pm 5\%$ variation. It considers the effect of Dean number (D_n), dimensionless spacer length (L/D) and number of bends. The correlation is valid in turbulent regime and for $L/D = \infty$, it reduces to Blasius equation.

The work is going on to generate more data with different fluids and different flow conditions so that a universal correlation can be developed.

5. REFERENCES

- [1] Ito, H., Pressure Losses in Smooth Pipe Bends, *ASME Journal of Basic Eng.*, 82(1960), pp. 131–143.
- [2] Barua, S. N., On Secondary Flow in Stationary Curved Pipes, *Quarterly Journal of Applied Mathematics*, 16(1962), pp. 61-77.
- [3] Popiel, C. O., and van der Merwe, D. F., Friction Factor in Sine-Pipe Flow, *ASME Journal of Fluids Engineering*, 118(1996), pp. 341–345.
- [4] Popiel, C. O. and Wojtkowiak, J., Friction Factor in U-type Undulated Pipe Flow, *ASME Journal of Fluids Engineering*, 122(2000), pp. 260-263.
- [5] Chen, I. Y., Lai, Y. K. and Wang, C. C., Frictional Performance of U-type Wavy Tubes, *ASME Journal of Fluids Engineering*, 125(2003), pp. 880-886.
- [6] Moffat, R. J., Describing the Uncertainties in Experimental Results, *Exp. Thermal Fluid Science*, 1(1988), pp. 3-17.

Acknowledgment: The authors gratefully acknowledge the financial and technical support provided by Bangladesh University of Engineering and Technology (BUET) in the course of this work.

NUMERICAL INVESTIGATION OF FLUID FLOW INSIDE A DIVERGING DUCT

Mohammad Mashud, Imtiaz Ahmed Faride, Mohammad Rizwen Ur Rahman and D.M.Asaduzzaman

Department of Mechanical Engineering
Khulna University of Engineering & Technology (KUET)
Khulna-9203, Bangladesh
(E-mail: mdmashud@yahoo.com)

ABSTRACT

Flow characteristics were investigated theoretically and numerically, inside a diverging duct through which a periodically fully developed flow of fluid is passed as working fluid. The governing differential equations along with boundary conditions were solved by finite difference method. The discretized equations with proper boundary conditions of numerical solutions were sought by obtaining Leibmann's Successive under Relaxation (SUR) method. It has been done on the basis of stream function and vorticity formula of the two dimensional Navier-Stoke's equation and continuity equation for all nodes. Computations were performed for different values of the Reynolds Number and the geometric parameters. If the divergence angle is sufficiently high and for high Reynolds number the flow become unsteady. The current study is ended only for steady laminar flow. Numerical results obtained were analyzed for the effectiveness of different values of duct length and outlet diameter for a fixed inlet diameter.

Key words: *Numerical Investigation, Diverging Duct and Inside Flow.*

1. INTRODUCTION

A divergent duct can be used when it becomes necessary to expand a fluid to increase the pressure and thereby decrease the velocity. Our current investigation aimed at analyzing the flow patterns and the variation of velocity inside the divergent duct along the centerline region. Study of the flow characteristics inside the diverging duct is of great importance if it is necessary to increase the velocity along core flow region, as flow is always affected to some extent by the length, inlet diameter, outlet diameter and other boundary conditions. If it is possible to increase the velocity along the centerline region by flowing fluid through a divergent duct, it can be used as a wind accelerator for a wind turbine. Because if it is possible to increase the velocity of the approaching wind to a wind turbine the power generated by turbine could be increased as wind power generation is proportional to the wind speed cubed. By placing a turbine into a divergent duct can accelerate the approaching wind velocity along the center line and can increase the power output.

In the case of internal duct flow the boundary layer thickness is considerably affected by the pressure gradient in the direction of flow. When a flat plate placed in a stream of velocity, the pressure may assumed to be uniform i.e. the pressure gradient is zero. But in the case of divergent flow i.e. the flow through diverging duct the pressure gradient is positive; the fluid in the boundary layer is further decelerated and hence assists in thickening of the boundary layer. The adverse pressure gradient plus the boundary shear decreases the momentum in the boundary layer and if they both act over a sufficient distance they cause the fluid in the boundary layer to come rest i.e. the retarded fluid particles, cannot, in general penetrate too far into the region of increased pressure owing to their small kinetic energy. Thus, the boundary layer is deflected sideways from the boundary, separates from it and moves into the main stream. This phenomenon is called separation [1]. Separation of the boundary layer greatly affects the

flow as a whole. The separation of fluid in a divergent channel depends upon the angle of divergence, Reynolds number and inlet velocity [2]. The separation of the flowing fluid is from the boundary first occurs at a point where the velocity gradient become zero, this point is known as separation point. On downstream of the separation point, a farther retardation of the fluid close the boundary can even have reverse or back flow near to the boundary. At the edge of the separated boundary layer, the velocities change direction. As a result of the reverse flow large irregular eddies are formed. The flow in eddies causes circulation of fluid [1], which produces, a line of vortices (known as a vortex sheet) [3]. Experimental investigations were carried out by Mohammad Mashud, Md. Mahfuz Sarwar and Md. Nafiur Rahman [4]; they developed a diffuser-type structure that is capable of collecting and accelerating the approaching wind. They devised a diffuser shroud with a brim that is able to increase the wind speed of approaching wind substantially by utilizing various flow characteristics (e.g., the generation of a very-low-pressure region by vortex formation, flow entrainment by vortices and so on) of the inner or peripheral flows of a diffuser shroud equipped with a brim. They showed that the velocity could be increased 1.6 to 2.4 times that of inlet by directing the air through a divergent duct, with attaching a brim of proper height to the outer periphery at the duct exit. In this investigation we consider only a diverging duct without brim or shroud.

The present study, however deals with systematically investigate the laminar flow through diverging duct for variation of parameters affecting the flow field. This study will enable the creation of a knowledge base for more effective and efficient design of diverging duct encountered in engineering applications. Such a knowledge base will also be helpful in avoiding costly experimentation to study the performance of diverging duct.

2. GOVERNING EQUATIONS

We considered a divergent channel of length L, inlet diameter d and outlet diameter D. A parabolic velocity profile is used at the inlet. Fig. 1 shows the geometry of the flow domain. The flow is considered to be two dimensional, steady state, incompressible, laminar and the physical properties are assumed to be constant through the divergent channel. The body force is neglected (F_x & F_y) here. The equation of motion for incompressible flow with constant transport properties, namely the Navier-stoke's equation and the continuity equation are used here as the governing equation. The governing equations in the non-dimensional form are-

Continuity equation

$$\frac{\partial U^*}{\partial X} + \frac{\partial V^*}{\partial Y} = 0 \dots\dots\dots (i)$$

Navier-Stokes equation

$$U^* \frac{\partial U^*}{\partial X} + V^* \frac{\partial U^*}{\partial Y} = -\frac{\partial P^*}{\partial X} + \frac{1}{Re} \left(\frac{\partial^2 U^*}{\partial X^2} + \frac{\partial^2 U^*}{\partial Y^2} \right) \dots\dots\dots (ii)$$

$$U^* \frac{\partial V^*}{\partial X} + V^* \frac{\partial V^*}{\partial Y} = -\frac{\partial P^*}{\partial Y} + \frac{1}{Re} \left(\frac{\partial^2 V^*}{\partial X^2} + \frac{\partial^2 V^*}{\partial Y^2} \right) \dots\dots\dots (iii)$$

The reference conditions are as, the inlet diameter is considered as the characteristics length and the corresponding maximum horizontal component of the velocity is considered as characteristics velocity. The dimensionless parameters in the equations above are defined as follows

$$X = \frac{x}{d}; \quad Y = \frac{y}{d}; \quad U^* = \frac{u}{u_{max}}; \quad V^* = \frac{v}{u_{max}};$$

And Reynolds number is defined as

$$Re = \frac{u_{max} d}{\nu}$$

The general boundary conditions in the flow domain are-

Boundary Condition for Inlet section:

Applying fully developed parabolic inlet profile,

$$U^* = \frac{u}{u_{\max}} = 4 \left(\frac{y}{d} - \frac{y^2}{d^2} \right) = 4(Y - Y^2)$$

In normal form, $u = 4y(1 - y)$

Stream function is obtained

$$\Psi = \left(2y^2 - \frac{4}{3}y^3 \right) + \Psi_0$$

Here $\Psi_0 = \text{Constant}$

The vorticity at inlet section,

$$\zeta = \left(-\frac{\partial u}{\partial y} \right) = -\frac{\partial^2 \Psi}{\partial y^2} = 4(2y - 1) \text{ (at the inlet } v=0)$$

Boundary Condition for outlet section:

Assuming fully developed flow conditions,

$$\begin{aligned} \frac{\partial u}{\partial x} &= 0 & \frac{\partial \Psi}{\partial x} &= 0 \\ \frac{\partial v}{\partial x} &= 0 & \frac{\partial \zeta}{\partial x} &= 0 \end{aligned}$$

At the Bottom Boundary:

We know that the velocity components are-

$$u = \frac{\partial \Psi}{\partial y} \quad \text{and} \quad v = -\frac{\partial \Psi}{\partial x}$$

Applying no-slip conditions,

$$u=0 \quad \text{and} \quad v=0$$

∴ Stream function $\Psi = c$, Assume $c = \text{constant}$

At The Top Boundary:

At top boundary the velocity components,

$$u=0 \quad \text{and} \quad v=0$$

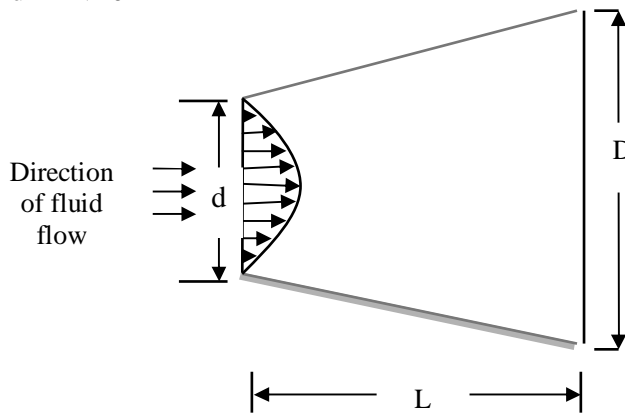


Figure 1 Geometry of the flow domain

3.0 NUMERICAL METHODOLOGY

The governing equations along with boundary conditions are solved using a numerical code written in FORTRAN language to get stream function, vorticity and velocities at every nodal point. Finite difference method is used to describe the equations. The conventional Gauss-Seidel method is used for iteration technique to solve the equations along with boundary conditions. The successive under relaxation (SUR) method is employed to accelerate the rate of convergence after each iteration. The inlet diameter and inlet velocity was fixed. The flow domain is solved for length 2.0 and 3.0 and the outer diameters vary from 1.2 to 3.0 with an interval of 0.2 for both of the length. The effect of Reynolds number on the flow field was studied for Reynolds numbers 200, 400, 600, 800, 1000, and 1200. But for both length 2.0 and 3.0, when outer diameter greater than 1.4 for Reynolds number greater than 400 the flow became complex and we are not analyzed that kind of flow.

4.0 RESULTS AND DISCUSSION

The results obtained by numerical (finite difference method) solution of the Navier-Stokes and continuity equations for expanding axis symmetric laminar flow is presented. A typical geometry for this study and boundary conditions have already been discussed above. The parameters affecting the performance of a diverging duct are the Reynolds numbers, angles of expansion (D/d) and lengths. The results presented here show the effect of varying Reynolds number on the flow domain for constant geometrical properties; for a length of 3.0, inlet diameter 1.0 and outlet diameter 1.60. It is found that the centerline velocities of the parabolic profiles are almost 1.08 to 1.99 times of the inlet for different Reynolds numbers at the outlet.

Figure 2 and 3 shows the streamline plots for two different values of Reynolds number. It can be seen that there are two different flow regions, namely the core flow region and the recirculation region. The recirculation region is indicated by the separating streamlines. The recirculating zone increases in size as Re increases. The recirculation region is the result of the pressure gradients normal to the streamlines. The effect of increasing Reynolds number strengthens and widens the recirculating zone and the overall flow intensifies. Dead flow reserve regions are created at the vicinity of the boundaries. The analysis of the flow field in the preceding sections can be better envisioned by the velocity vector field provided in Figure 4 and 5. A greater shaft length of the arrows near the wall and along the centerline near the outlet gives the indication of higher velocities in that region. It is well evidenced from the velocity vector field that at higher Reynolds number and greater angles of expansion significant recirculating bubbles are formed near boundaries. These bubbles are produced by a significant reduction in fluid momentum and adverse pressure gradient caused by area expansion.

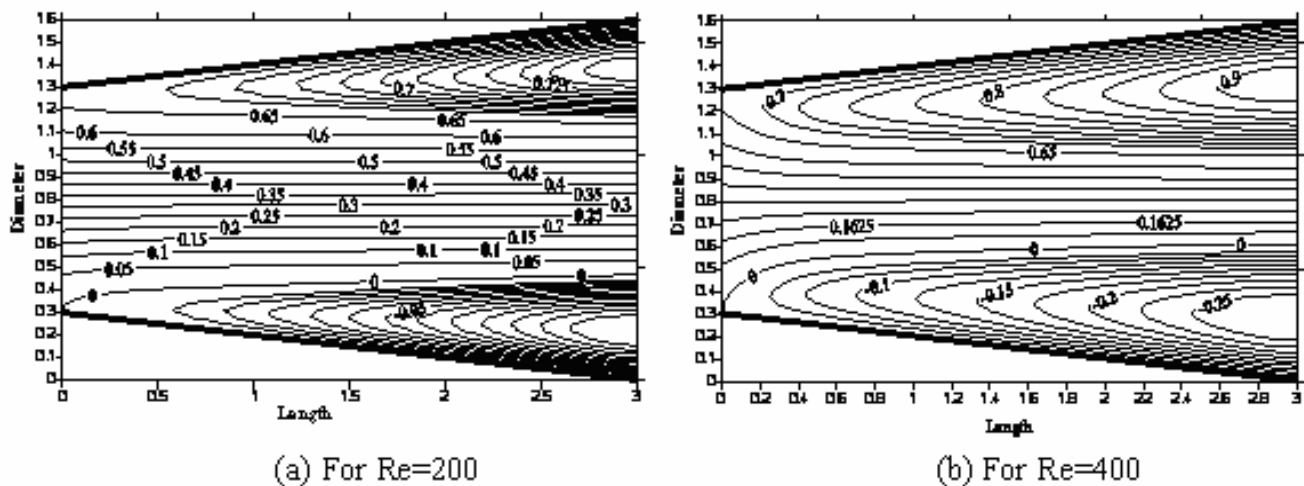


Figure 2 Streamlines and Velocity vectors at different Reynolds number

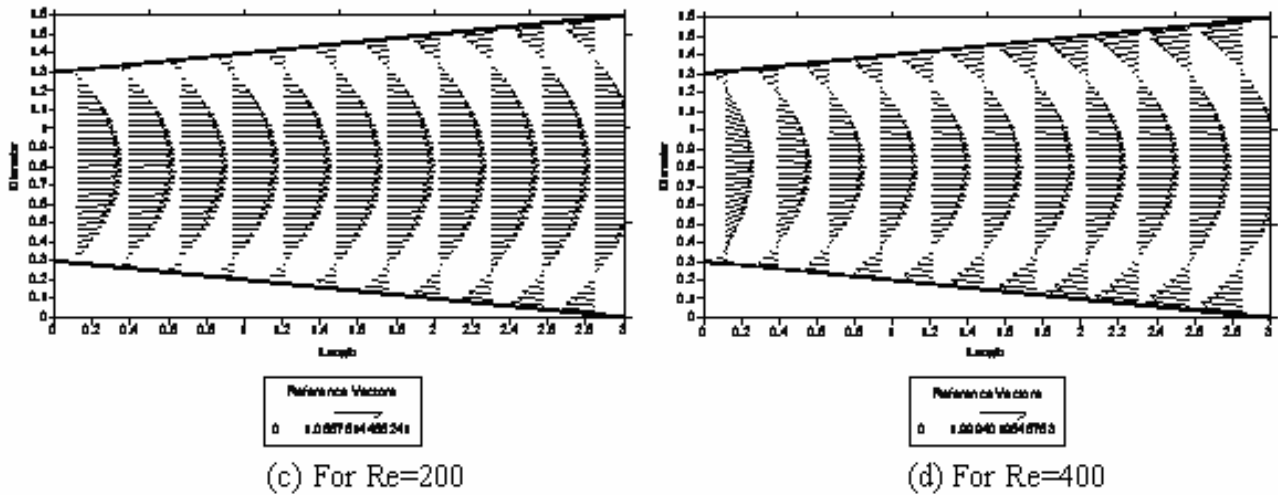


Figure 3 Streamlines and Velocity vectors at different Reynolds number (cont.)

The axial velocity distributions through the divergent duct for varying Reynolds number are plotted in Figure 4.2. The velocity profile at the entrance to the channel is parabolic with a maximum axial velocity of unity in accordance to the boundary condition. Figure 4.2 show that the peak of the horizontal velocity component increases and its location shifts toward right with the increasing Reynolds number. Near the wall, a large velocity area with negative axial velocity develops which indicates the existence of significantly large recirculation region. Near the outlet, for Reynolds number ranging from 200 to 400, the cross-sectional maximal axial velocities are at least 1.08 times larger than the entrance. Figure 4.3 shows the variation of U/U_{max} at the centerline for different Reynolds number. It showed that increase in the velocity along the centerline is more for higher Reynolds number. It also showed a good agreement with the velocity profile showed in Figure 4.2.

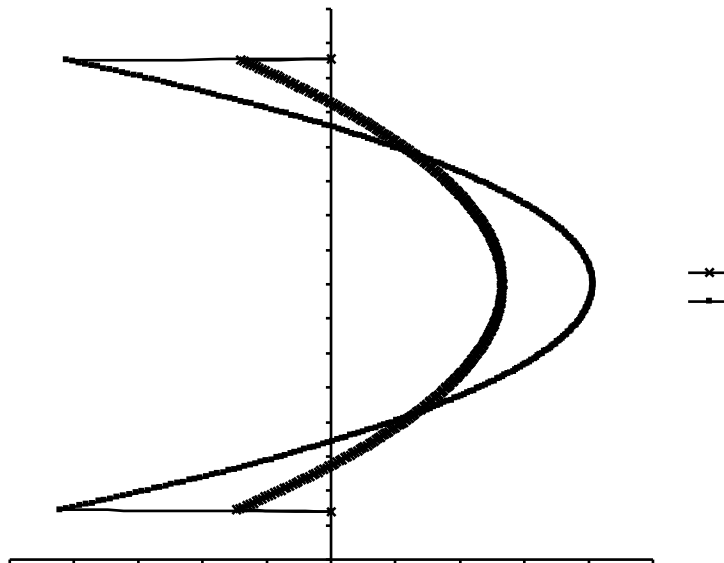
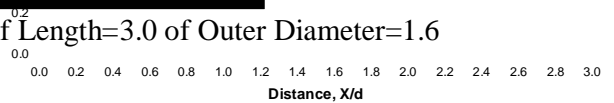


Figure 4 Velocity profile at channel of Length=3.0 of Outer Diameter=1.6



Figure 5 Variation of centerline velocity at channel of Length=3.0 of Outer Diameter=1.6



Re=200
Re=400

5.0 CONCLUSION

The present numerical study throws some light on flow inside a diverging duct. The extent of recirculation near the boundary helps in increasing the velocity in the centerline region. The study also reveals the effect of change in Reynolds number and geometrical parameters on flow domain. This kind of study will definitely help to design diverging duct for flow accelerator like within the wind turbine.

NOMENCLATURE

L	Length of the domain	ω	Vorticity
d	Inlet diameter of the domain	ω^*	Dimensionless Vorticity
D	Outlet diameter of the domain	ψ	Stream function
ψ_0	Initial value of Stream function	ρ	Density of fluid
ψ^*	Dimensionless Stream function	u_∞	Free stream velocity
μ	Dynamic viscosity of fluid	ν	Kinematic viscosity of fluid
Re	Reynolds number = $\frac{u_\infty d}{\nu}$	u,v	Velocity components

REFERENCES

- [1] Modi, P. N.; Seth, S. M.; "Hydraulics And Fluid mechanics Including Hydraulic Machines" Fourteenth Edition, 2002, pp. 238, 239, 518, 519, 531, 930.
- [2] Cockrell, D.J., and Markland, E., 1963, "A Review of Incompressible Diffuser Flow," Aircraft Engineering, October, pp. 286-292.
- [3] Douglas J F, Gasiorek J. M. and Swaffield J. A., "Fluid Mechanics", Longman publishers, pp 327-332.
- [4] Mashud, Mohammad, Sarwar, Md. Mahfuz and Rahman, Md. Nafiur, "Development of a High-Performance Wind Turbine with a Diffuser", Paper ID 146, 12th Annual Paper Meet, February, 2008, Dhaka.
- [5] Karasudani, T. and Ohya, Y. "Wind Velocity Acceleration by Hollow Bodies" J. Japan Soc. of Fluid Mechanics Nagara, 22, 2003, pp 337-343.

AN EXPERIMENTAL STUDY OF CO-AXIAL FREE JETS

Mohammad Nasim Hasan¹ and M. A. Taher Ali²

¹ Assistant Professor, Department of Mechanical Engineering, BUET, Dhaka-1000

² Professor, Department of Mechanical Engineering, BUET, Dhaka-1000
nasim@me.buet.ac.bd

ABSTRACT

The present study deals with the experimental investigations of the mean flow characteristics in the velocity field of co-axial free jets. Co-axial jet flows have been developed by issuing two air jets with different unidirectional velocities from a concentric compound nozzle. The central air jet comes out from a 29 mmD central nozzle while the annular air jet is emitted through the annular space between the outer and the central nozzle. Two outer nozzles of 63 mm and 80 mm diameter have been used that results in two annular to central jet area ratios as 3.57 and 6.6 respectively. Four annular to central jet velocity ratios up to 0.75 have been considered for each nozzle configuration. Measurements of velocity is made in the mixing zone of these two jets with the help of a 3 mm OD Pitot-static tube for Reynolds number of 3.72×10^4 based on the exit centerline velocity and diameter of the inner jet. From the measurements, centerline and streamwise velocity profiles and virtual origin of the co-axial jets have been explored for different upstream conditions. The results show that momentum transfer amongst fluid streams in the developed region of co-axial jets takes place more rapidly both at lower velocity and area ratios of its. Its virtual origin is found to move in upstream locations as both of its velocity and area ratios increase. For larger annular to central jet area ratios of co-axial jets, the dominancy of the annular jet on overall jet field is found to be prominent even at low velocity ratios.

Keywords: *Turbulent co-axial free jets, Potential core, Virtual origin, Jet half-width.*

1. INTRODUCTION

Co-axial jet type flows are present in many industrial applications such as the combustion chambers of the rocket engines, the jet pumps, the mixing tanks, the cooling systems etc. For this reason, the study of mean and turbulent jet field has been a subject of great interest for many researchers over the past decades.

Experimental work on co-axial jets has begun since 1950's. Frostal [1], Stark [2] and Chigier [3] studied the mixing of a circular jet with an annular co-axial jet for various nozzle diameters and velocity ratios. Measurements were taken by using a Pitot tube. They found that the nozzle diameters and velocity ratios were the most significant parameters which determined the jet configuration and average velocity profile of the flow. The common characteristic of all these investigations is that they were concerned only by the mean velocity field rather than the turbulent flow field structure. Champagne and Wygnanski [4] were the

first who used a hot wire anemometer in their turbulent co-axial jet's research. In contrast to what Frostal and Shapiro [1] announced, Champagne and Wygnanaski showed that change of both velocity and area ratios have little effect on jet half-width ($y_{0.5}$). According to them, the length of inner potential core of co-axial jets is strongly dependent on both the velocity as well as area ratios while that of the outer potential core is more or less independent of velocity ratio.

Using hot wire anemometry, Ko and Kwan [5] determined pressure fluctuations and velocity fluctuations in the initial and developed regions of co-axial jets. From their result they concluded that co-axial and simple jet's structures are coherent and physically similar in the developed region of the flow field. Ko and Au [6] showed that the flow field of co-axial jets can be divided into three separate regions: the initial region, the intermediate region and the developed region. The initial region is located between the nozzle exit and the end of outer potential core, immediately downstream is the intermediate region which ends at the reattachment point. From this point the flow behaves like a single jet resulting from only one nozzle and essentially it is the developed region of jet flow field where the flow variables attain a self-preservation state. This type of flow is characterized by the presence of two mixing layers; the outer mixing layer contiguous to the ambient air and the inner mixing layer confined between the outer and central jet.

Ribeiro [7] experimentally studied mean velocity, Reynolds stresses and probability density distribution of fluctuating velocity of axisymmetric turbulent co-axial jets, with or without swirl. According to his findings, the presence of swirl in co-axial jets results in earlier attainment of self-preservation state of jets. Rehab et al. [8] used hot-wire anemometry to study the structure of turbulent co-axial jets with outer to central jet velocity ratios (r) greater than 1. Two flow regimes were identified depending on whether the velocity ratio (r) is greater than a critical value (r_c). When $r < r_c$ the faster annular jet periodically pinches the central jet and the pinching frequency corresponds to the outer jet mode. When $r > r_c$ the inner potential core is truncated and followed by an unsteady recirculation zone. Begum et al. [9] studied turbulent co-axial jets of different area ratios and velocity ratios. According to them the attainment of self-similarity state of co-axial jets flow field depends on both the velocity ratio and area ratio. Chowdhury [10] studied co-axial jets with and without swirl and she found that addition of swirl either in the central jet or outer jet enhances mixing in co-axial jets.

2. EXPERIMENTAL METHOD

A schematic diagram of the co-axial jet flow system is illustrated in Figures [1-2]. The co-axial jet flow system has been developed by adding a central circular air flow system in the existing jet flow facility in the laboratory. The jet flow facility has overall length of 8.1 m having 80 mm diameter exit nozzle. In the delivery side of the flow facility the diameter of the pipe is reduced in two stages from 475 mm to 80 mm where the experimental nozzle is fitted. A centrifugal blower is placed below the main flow system to supply air to the central nozzle. The 100 mm discharge line of this blower is connected to a 3.5 kW air heating system. A 62 mm PVC pipe is connected to the delivery side of the air heating system that enters radially in to the 2nd settling chamber of the main flow system. In order to place the central nozzle along the central axis of 80 mm nozzle 3 sets of centralizers have been placed in three different locations. Finally, the exit diameter of the central nozzle is reduced to 29 mm through 100 mm×29 mm reducer. The flow straightener and wire screens are present in both jets to straighten the flow as well as to break down large eddies present in the air flow. To minimize the effect of any boundary on the jet flow, the nozzle centerline is set at 1400 mm above the ground. Throughout the study, nozzle exit center is taken as the origin. The center line of the nozzle in the direction of flow is taken as positive x-axis and radial distance pointing upwards as positive y-axis and the axis 90° anticlockwise from positive x-axis is considered as the positive z-axis as shown in Fig. [3].

The experiments involve measurements of velocity at different grid points of the jet flow field. Measurement of velocity in different locations of the jet flow field is made by using a 3 mm OD Pitot-static tube [United Sensor] with an embedded thermocouple at the tip. The pressure signal of the Pitot-static tube is recorded by using a Furnace Control Pressure Transducer [Model: FC012]. The Pitot -static tube is traversed in the air stream with the help of a Mitutoyo (Japan) coordinate measuring machine (type: CS 652). This traversing mechanism is placed on a hydraulically operated table, which 900 mm away from the nozzle axis to avoid any possible disturbances. During the experiment the heating system remains inoperative.

All the measurement points are made non-dimensional by dividing the distances along y-axis (y) with either inner nozzle diameter (d) or axial distance (x). The local velocity (U) is made non-dimensional by dividing it with exit centerline velocity denoted as U_{co} . The growth of jet field is analyzed in terms of jet half width ($y_{0.5}$). To get a better understanding of the evolution of velocity in streamwise direction, a special form of graphs are plotted in the axes of U/U_{co} vs. y/x .

3. RESULTS AND DISCUSSION

Mean flow characteristics in the velocity field of turbulent co-axial jets have been investigated for different upstream conditions. The annular to central jet velocity ratio (U_2/U_1) is varied as 0.0, 0.25, 0.50 and 0.75 for two different values of annular to central jet area ratios as 3.57 and 6.6. Considering the 29 mm diameter central jet as the primary one, the Reynolds number has been calculated as 3.72×10^4 for central jet velocity of 19.90 m/s.

3.1 Centerline velocity

Figure [4] presents the centerline velocity profiles (U/U_{co}) of a 29 mmD single jet ($U_2/U_1 = 0.0$) and that of co-axial jets ($A_2/A_1 = 3.57$, $U_2/U_1 = 0.25$). The length of potential core L_p , for single jet is found to be $4d$ whereas it is found to be $6.5d$ for co-axial jets. The longer potential core of co-axial jets is because of the fact that the presence of annular jet enhances mixing process with much less interaction thereby with less energy dissipation which retards the growth of the shear layer towards the axis of the jets from the surroundings. From this figure it is also clear that the decay of centerline velocity occurs relatively at a faster rate in the single jet than that of the co-axial jets. This shows the augmented momentum transfer in the developed zone of the single jet as compared to the co-axial jets.

The effect of velocity ratio (U_2/U_1) on the centerline velocity decay of co-axial jets ($A_2/A_1 = 3.57$) are manifested in figure [5] for Reynolds number $Re = 3.72 \times 10^4$. In all the cases, the centerline velocity seems to be almost constant up to $x/d \approx 6.5$ for all velocity ratios. Afterwards, the centerline velocity starts to decrease monotonically in the downstream direction. However it is found that at lower velocity ratio, the centerline velocity of co-axial jets decreases at faster rate along the jet axis. This happens because lower velocity ratio presents larger velocity gradient between the central jet and adjacent annular jet creating more resistance to the flow of the central jet by the annular jet. As a result, the velocity along the axis of the central jet is found to decay quickly at low velocity ratio.

Figure [6] is presented to show the effect of area ratio (A_2/A_1) on the centerline velocity profile of co-axial jets ($U_2/U_1 = 0.25$) at $Re = 3.72 \times 10^4$. This figure reveals that the effect of area ratio on the centerline velocity within the potential core as well as on the length of potential core is insignificant i.e. the length of potential core is found to be $6.5d$ for both of the nozzle configurations. Begum [11] worked with co-axial jets of different area ratios (A_2/A_1) ranging from 0.56 to 2.61. In her study, she found the length of potential core to be $4.5d$, $5.25d$ and $6.5d$ for area ratio of 0.56, 1.25 and 2.61 respectively with velocity ratio (U_2/U_1) ranging from 0.10 to 0.90. Thus it can be concluded that the effect of area ratio on potential core length (L_p) becomes insignificant at higher values of area ratio. However the effect of area ratio on the decay of centerline velocity is found still to be prominent in the developed zone of co-axial jets as was found by Begum [11]. Just after the potential core, the centerline velocity is found to decline rapidly for smaller area ratio. This fact is an indication of the rapid mixing as well as momentum transfer amongst the fluid streams of co-axial jets at low area ratio.

3.2 Virtual Origin

The origin of the co-ordinate system of a jet has been taken as the geometric origin. But practically it has been observed by many researchers that the jet seems to be discharged from either downstream or upstream of the lip of jet producing component. Thus the virtual origin comes in defining jet characteristics instead of geometric origin and is classified as: (1) Kinematic virtual origin (2) Geometric virtual origin

The Kinematic virtual origin is determined from the decay of the centerline mean velocity, U_c while the geometric virtual origin is determined from the growth of the jet half width ($y_{0.5}$). As found in figures [5-6] both the velocity ratio (U_2/U_1) and area ratio (A_2/A_1) of co-axial jets determine the centerline velocity

decay of the jets. That means the location of kinematic virtual origin (C_k) of co-axial jets depends on both the velocity ratio and area ratio of co-axial jets. With the increase of velocity ratio of co-axial jets, the kinematic origin of the jets is found to move in the upstream direction as shown in Figure [7]. Figure [8] shows that as the annular to central area ratio (A_2/A_1) of co-axial jets increases, the kinematic virtual origin (C_k) of co-axial jets moves in the upstream locations. This is because, decay of centerline velocity of co-axial jets takes place rapidly at low velocity ratios as well as low area ratios of the jets.

A commonly used measure to characterize the growth of the jet is the jet half width ($y_{0.5}$). It is defined as the distance (y) measured from the centerline of the jet, where the local mean velocity (U) is equal to half of the local centerline mean velocity (U_c). Figure [9] shows the propagation of dynamical half width ($y_{0.5}$) of co-axial jets ($A_2/A_1 = 3.57$) with different outer to inner velocity ratio. As shown in the figure, the location of geometric virtual origin moves in the upstream location of the jet axis as the velocity ratio (U_2/U_1) increases.

3.3 Streamwise Velocity Profile

Streamwise velocity profiles of co-axial jets ($A_2/A_1 = 3.57$) for different velocity ratios (U_2/U_1) are presented in Figures [10] for $Re = 3.72 \times 10^4$. From these figures it is obvious that, as the velocity ratio increases, the influence of annular jet on the streamwise velocity profiles of overall jet field increases. For co-axial jets ($0.56 < A_2/A_1 < 2.61$) Begum [5] found that due to the intermixing between the two jets no separate existence of the jets could be identified beyond axial distance $x/d = 2.0$ for all velocity ratios.. But in the current investigation with $A_2/A_1 = 3.57$, the existence of annular jet is quite evident up to $x/d = 7.0$ for velocity ratio $U_2/U_1 = 0.25$ (figure 10.a) and up to $x/d > 7.0$ for $U_2/U_1 = 0.75$ (figure 10.b). After these respective positions, the velocity profiles of the co-axial jets attain the form of a unified jet confirming the completion of mixing of these two jet flows. Thus at higher area ratio (A_2/A_1), the annular jet of co-axial jets plays a vital role in shaping the overall jet flow field of co-axial jets even though at lower velocity ratio (U_2/U_1).

Figures [11-12] show the effect of velocity ratio on the streamwise velocity profiles of co-axial jets having area ratio 3.57 and 6.6 respectively at $Re = 3.72 \times 10^4$. In each figure, three groups of curves for three axial locations ($x/d = 1.0, 5.0$ and 9.0) are shown. A strong influence of annular jet on the overall velocity profile of the jet is observed and the degree of influence increases with the increase in velocity ratio as well as area ratio. In case of the co-axial jets ($A_2/A_1 = 3.57$), the flow field becomes just like a unified jet within axial distance $x/d = 9.0$, for all the velocity ratios ($U_2/U_1 = 0.25, 0.50$ and 0.75) as shown in Figure [11]. But for high area ratio of co-axial jets ($A_2/A_1 = 6.6$), this condition is achieved only for velocity ratio $U_2/U_1 = 0.25$ within $x/d = 9.0$ as found in Figure [12]. It means the location of the unification of co-axial jets moves downstream with the increase of both velocity and area ratios. Increase in both velocity and area ratios of co-axial jets result in increased momentum flux through the annular jet which in turn increases the influence of the annular jet on the central jet. For this reason a co-axial jet with high velocity and area ratio takes long time to present a flow field similar to a unified jet.

4. CONCLUSION

Thus it can be inferred from this experimental work regarding co-axial jets that

- i. Momentum transfer amongst the fluid streams in the developed region of co-axial jets takes place more rapidly at lower velocity and area ratios of co-axial jets.
- ii. At higher area ratios of co-axial jets, effect of area ratio on potential core length gradually become insignificant but its effect on velocity decay in the developed region of jet flow field remains prominent.
- iii. The virtual origin of co-axial jets moves in upstream locations as both the velocity and area ratio increases.
- iv. The dominancy of annular jet on the overall jet field of co-axial jets is observed even at lower velocity ratios (U_2/U_1) for higher annular to central area ratios of the jets. Moreover, the unification of the inner jet and annular jet occurs in further downstream locations as compared to that of co-axial jets with lower area ratios (A_2/A_1).

5. NOMENCLATURE

Symbol	Meaning
d	Diameter of inner nozzle
d_o	Diameter of outer nozzle
Re	Reynolds number
U_1	Mean velocity of central jet
U_2	Mean velocity of annular jet
U_{co}	Centerline velocity at nozzle exit
U	Local velocity
U/U_{co}	Non-dimensional velocity
$A_1 = \pi d^2/4$	Area of the inner nozzle
$A_2 = \pi (d_o^2 - d^2)/4$	Area of the annular nozzle
L_p	Length of potential core
$Y_{0.5}$	Jet half width

6. REFERENCE

1. Frostall, W. and Shapiro, A. H., "Momentum and Mass Transfer in Co-axial Gas Jets", Trans. ASME Vol. 73, pp. 219, 1951.
2. Stark, S. B., "Mixing of Gas Stream in a Flame", Zh Tech Vol. 23, pp.1802-1819
3. Chigier, N. A. and Beer, J. M., "The Flow Region near the Nozzle in Double Concentric Jets", Journal of Basic Engineering, pp. 797-804, 1964.
4. Champagne, F. H., and Wygnanski, I. J., "An Experimental Study of Co-axial Turbulent Jet", International Journal of Heat and Mass Transfer, Vol. 14, pp. 1445-1464, 1971.
5. Ko, N. W. M and Kwan A. S. H "The Initial Regions of Subsonic Co-axial Jets", Journal of Fluid Mechanics, Vol. 73, pp. 305-322, 1976.
6. Ko, N. W. M and Au. H., "The Initial Regions of Subsonic Co-axial Jets of High Mean Velocity Ratio", Journal of Fluid Mechanics, Vol. 73, pp. 305-322, 1976.
7. Ribeiro, M. M. and Whitelaw, J. H., H "Co-axial Jets with or without Swirl", Journal of Fluid Mechanics, Vol. 96 Part 4, pp. 769-795, 1980.
8. Rehab, H., Villermaux, E. and Hopfinger, E. J., "Flow Regimes of Large Velocity Ratio Co-axial Jet", Journal of Fluid Mechanics, Vol. 345, pp. 357-381, 1997.
9. Ali, M. A., Begum, R. and Hasan, M. N., "Effect of Velocity and Area Ratio on Mixing of Co-axial Jets", 7th International Conference on Mechanical Engineering, Paper No. ICME2007-FL-30, BUET, Dhaka, Bangladesh, December 29-31, 2007.
10. Chowdhury, R., T., "Experimental Study of Swirling Co-axial Jets", M.Sc. Thesis, Mechanical Engineering Department, BUET- Dhaka, 2004.
11. Begum, R., "Experimental Study of Co-axial Free Jets", M.Sc. Thesis, Mechanical Engineering Department, BUET- Dhaka, 2004.

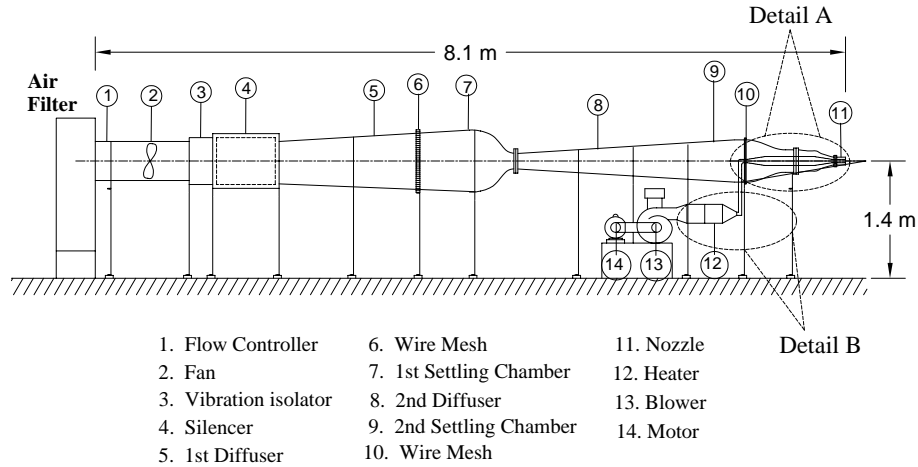


Figure 1: Schematic Diagram of the Jet Flow Facility

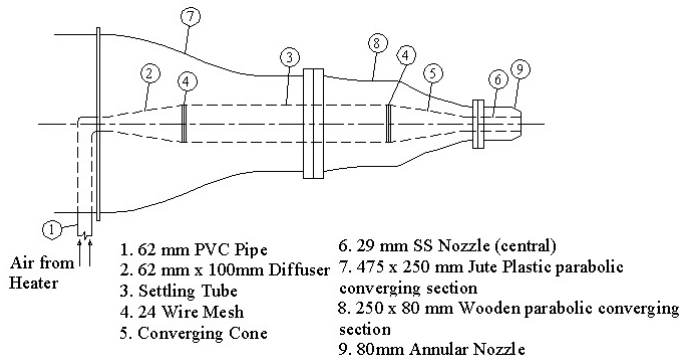


Figure 2: Enlarged View of Co-axial Flow System

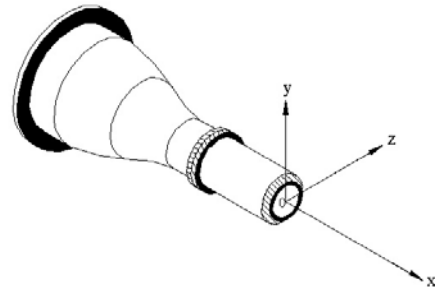


Figure 3: Co-ordinate System of Nozzle

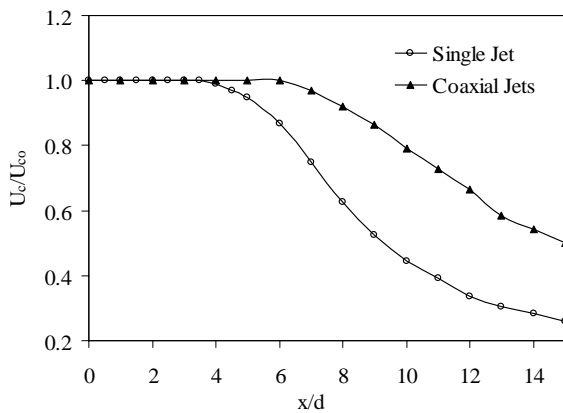


Figure 4: Centerline Velocity Profiles of Single Jet and Co-axial Jets ($A_2/A_1 = 3.57$, $U_2/U_1 = 0.25$) at $Re = 3.72 \times 10^4$.

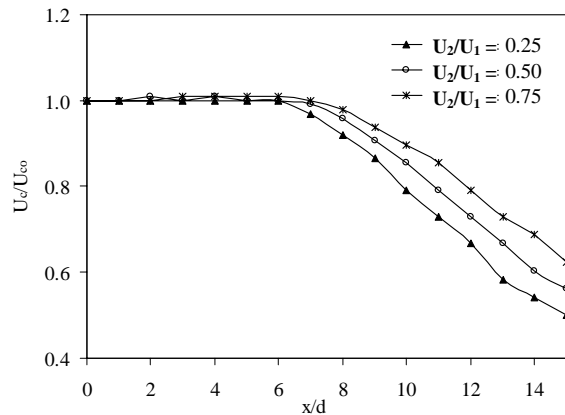


Figure 5: Effect of Velocity Ratio on Centerline Velocity Profile of Co-axial Jets ($A_2/A_1 = 3.57$) at $Re = 3.72 \times 10^4$.

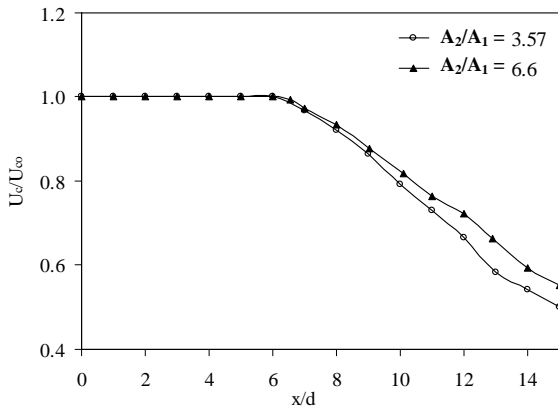


Figure 6: Effect of Area Ratio on Centerline Velocity Profile of Co-axial Jets at $Re = 3.72 \times 10^4$ and $U_2/U_1 = 0.25$.

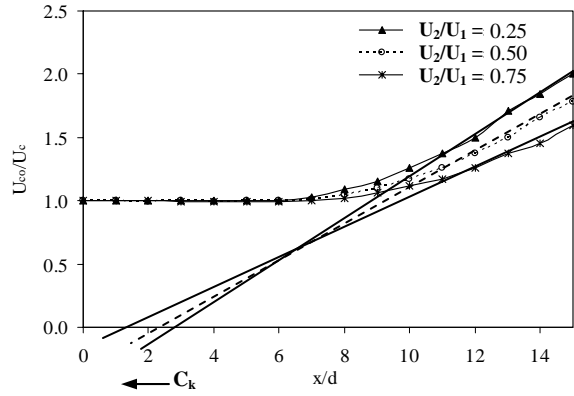


Figure 7: Effect of Velocity Ratio on the Location of Kinematic Virtual Origin (C_k) of Co-axial Jets ($A_2/A_1 = 3.57$) at $Re = 3.72 \times 10^4$.

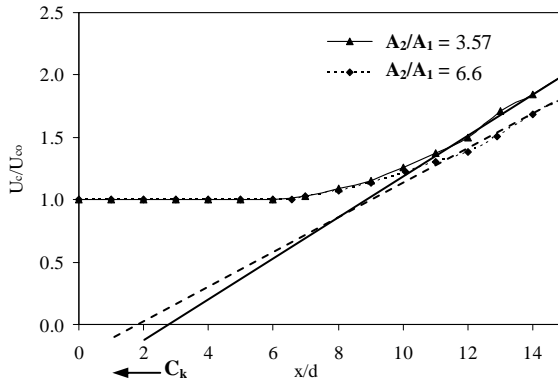


Figure 8: Effect of Area Ratio on the Location of Kinematic Virtual Origin (C_k) of Co-axial Jets with $U_2/U_1 = 0.25$ at $Re = 3.72 \times 10^4$.

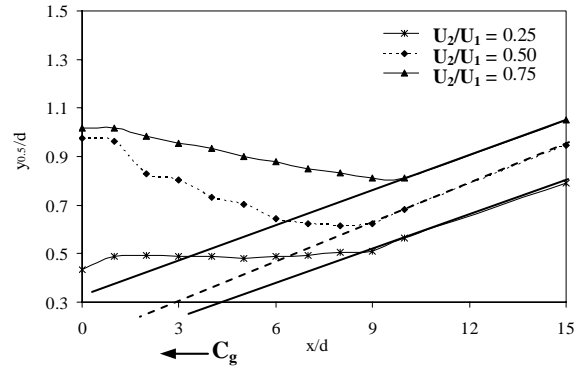
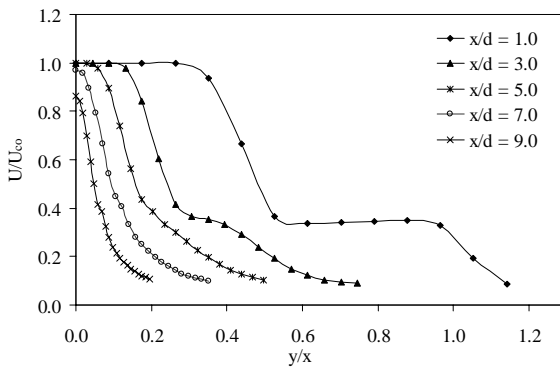
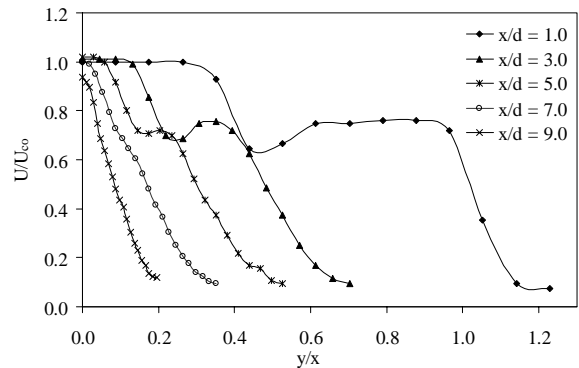


Figure 9: Effect of Velocity Ratio on the Location of Geometric Virtual Origin (C_g) of Co-axial Jets ($A_2/A_1 = 3.57$) at $Re = 3.72 \times 10^4$.



(a)



(b)

Figure 10: Evolution of Streamwise Velocity Profiles of Co-axial Jets ($A_2/A_1 = 3.57$) at $Re = 3.72 \times 10^4$. (a) $U_2/U_1 = 0.25$ and (b) $U_2/U_1 = 0.75$

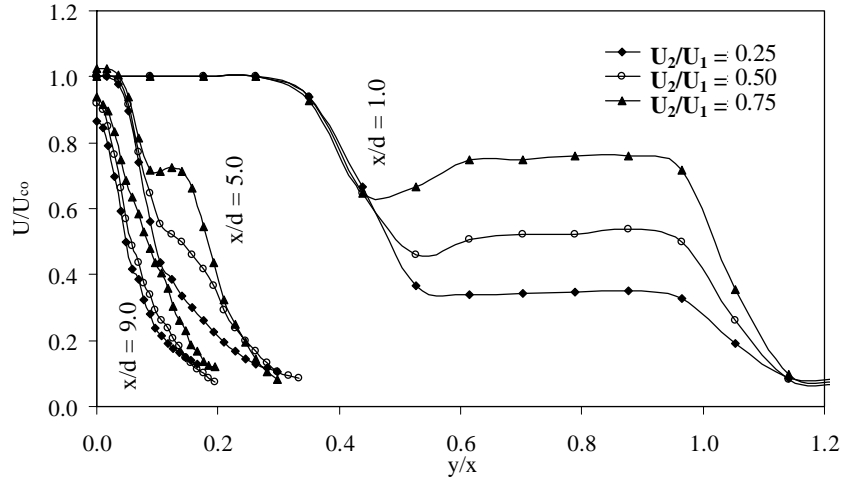


Figure 11: Effect of Velocity Ratios on Streamwise Evolution of Velocity Profiles of Co-axial Jets ($A_2/A_1 = 3.57$) at $Re = 3.72 \times 10^4$.

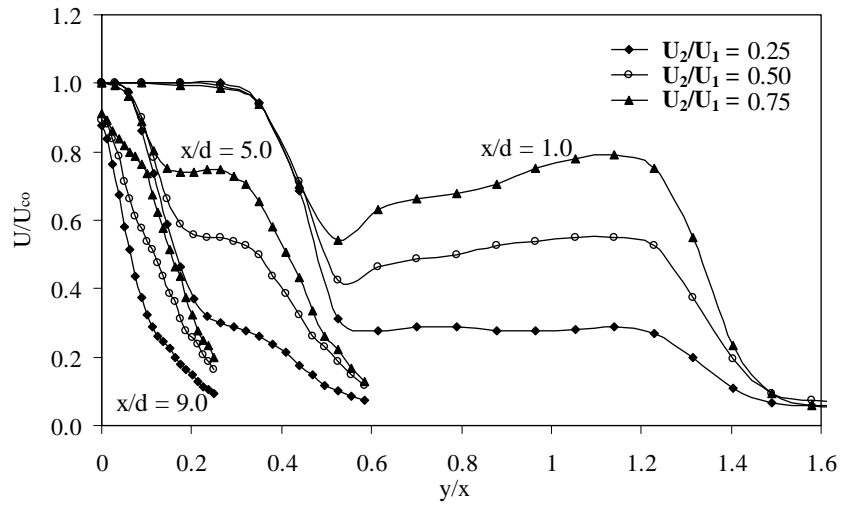


Figure 12: Effect of Velocity Ratios on Streamwise Evolution of Velocity Profiles of Co-axial Jets ($A_2/A_1 = 6.6$) at $Re = 3.72 \times 10^4$.

Numerical Prediction of Buffeting and Calculation of Transient Boundary Layer Separation over Airfoils

Mehran Shahryari¹, Foad Farhani²

¹Iranian Space Agency, Tehran, Iran.

²Department of Mechanical Engineering

Iranian Research Organization for Science and Technology (I.R.O.S.T),

P.O. Box 15815 – 3538, Tehran, Iran.

e-mail: a_mshahryari@yahoo.com

ABSTRACT

In transonic flow conditions, the shock wave/turbulent boundary layer interaction and the flow separation on the upper surface of an aircraft wing induce flow instabilities, “buffet”, and then structural vibrations, “buffeting”. Buffeting phenomenon occurs when the aircraft's Mach number or the incidence edge angle increases, and greatly affects the aerodynamic behavior, limiting the aircraft's flight envelope. The transient boundary layer separation is computed numerically using fully time-consistent viscous compressible method. This method differentiates between the steady solutions and the transient “buffet” generated by transonic shock induced separation over a lifting airfoil with smooth surfaces. We have studied two types of airfoils namely 18% circular arc airfoil and RA16SC1 airfoil. The results indicate that transient pressure distributions display time-histories and spectral properties as functions of Mach number and incidence angle. The prediction of self-induced transient separated flows is obtained at non-lifting conditions over asymmetrical circular arc airfoil. This work differentiates between steady flows and transient buffeting flows over RA16SC1 airfoil, depending on the incidence angle and Mach number, at transonic speed and lifting conditions. Several calculations have been performed for a Mach number of 0.724, and incidence angles between 0° and 4°. The time-histories of the lift coefficient, show that the steady solutions which are predicted for the lowest incidence angles, are progressively transformed into unsteady solutions when the incidence angle is increased. From final results, details of time fluctuations display the small variations of the distributions of pressure over the airfoil. The numerical results show good agreement with buffet experiments in two dimensions, which will be used for further buffeting predictions.

KEYWORDS: Buffeting, Boundary layer, Shock wave, Airfoil, Incidence angle

1. INTRODUCTION

There has been much progress in calculating the boundary layer separation using viscous–inviscid interaction methods [1-9]. However, computation of steady separation in three-dimensions requires more research. Similarly, calculation transient boundary layer separation over geometries with smooth surfaces seems to be an important area from the theoretical and practical point of view, if for example, we attempt to understand how far the separation is connected with buffet and buffeting phenomena. In this research fully

compressible Navier–Stokes equations have been used to investigate steady and unsteady boundary layer interactions. Using this method, we have attempted to predict the self induced buffeting separation over steady airfoils, at lifting condition, with transient transonic shock wave-boundary layer interaction. Some of our calculation results have been compared with available experimental data.

2. GEOMETRY AND GRID GENERATION

2.1 Symmetrical Airfoil

In order to model buffeting phenomena on a symmetrical airfoil, the 18% circular arc airfoil geometry has been used. Flow field has been selected such that the distance from leading edge to the front boundary is 20 chord lengths. Downstream boundary has been located at 10 chord lengths from the trailing edge. The top and bottom boundaries have been located at ± 40 chord lengths. Structured network has been used to solve the flow field so that network becomes dense toward the airfoil surface.

2.2 Lifting Airfoil

Geometry of RA16SC1 has been used as a lifting airfoil. Boundaries in the flow direction (X-direction) have been located at ± 20 chord lengths. The top and bottom boundaries have been located at ± 40 chord lengths. The computation has been carried out on a structured grid, with 100 nodes on each side of the airfoil. Network grids are denser near the surface of the airfoil.

3. GOVERNING EQUATIONS

The interaction between the boundary layer and shock wave results in the buffeting phenomena. Therefore, compressible full Navier-Stokes equations in two dimensions have been solved in transient. Continuity and energy equations have been solved together with Navier-Stokes equations. Since this turbulence model presents good results for boundary layers subjected to adverse pressure gradients, we have selected Spalart-Allmaras [8] for modeling the flow turbulence.

4. NUMERICAL RESULTS

Figure 1 shows the iso-Mach number contours near the symmetrical airfoil under steady flow condition. At the distance of about 75 percent of a chord length, a normal shock has been formed, which interacts with the boundary layer on both sides of the airfoil. This interaction causes a jump in pressure distribution on airfoil, as shown in Fig. 2. Experimental data, obtained at the same boundary conditions [9], have been presented in Fig. 2. This figure also shows good agreement between experimental data and numerical results. However, a little difference exists near the shock boundary layer interaction and the separated region.

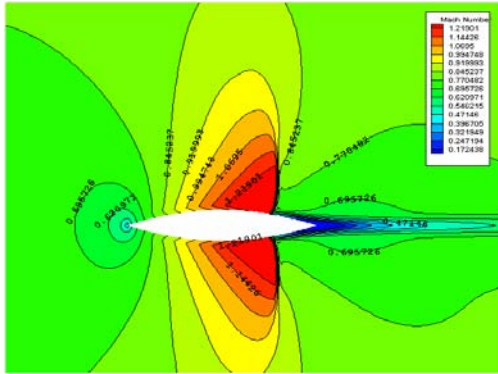


Fig.1 Mach number contours near symmetrical airfoil in steady flow, $M_\infty=0.788$, $\alpha = 0^\circ$

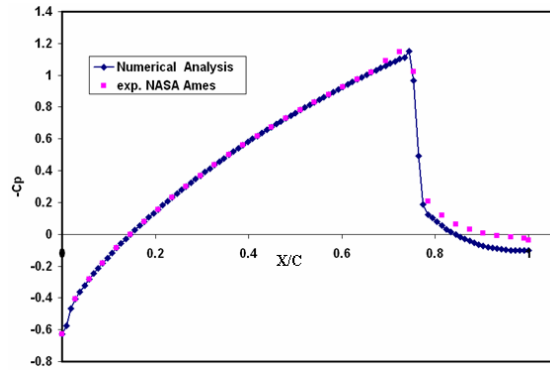


Fig.2 Pressure coefficient on symmetrical airfoil in steady flow, $M_\infty=0.788$, $\alpha = 0^\circ$

Figure 3 shows iso-Mach number near the symmetrical airfoil at different intervals. A normal shock is configured near the 70 percent of a chord length from the leading edge, and its location oscillates in a small domain with frequency of about 20 Hz. This shock wave causes a great jump in pressure distribution on the airfoil which is shown in Fig. 4.

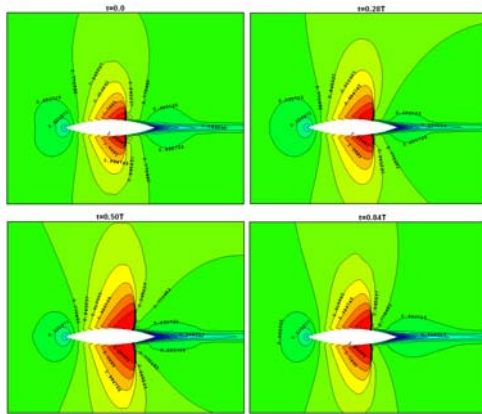


Fig.3 Mach number contours near symmetrical airfoil in transient flow, $M_\infty=0.788$, $\alpha = 0^\circ$

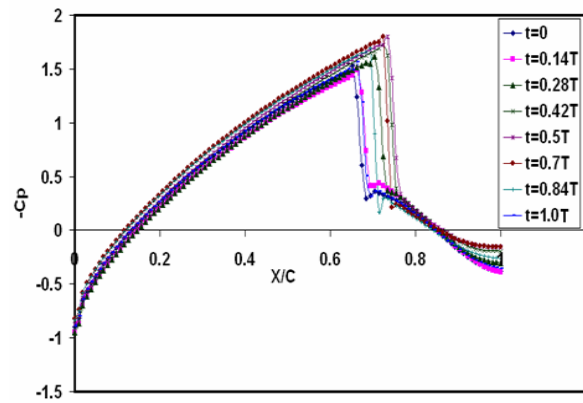


Fig.4 Pressure coefficient on the symmetrical airfoil in the transient flow, $M_\infty=0.788$, $\alpha = 0^\circ$

Variation in the location of the shock boundary layer interaction over a period is shown in Fig. 5. During half of the period, the shock-boundary layer interaction occurs at the farthest point from the leading edge. This phenomenon is limited in the distance between 66.5 to 74.5 percent of the chord length from the leading edge.

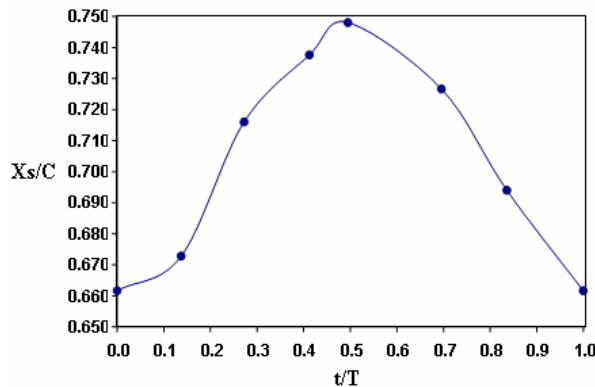


Fig.5 Position of shock-boundary layer interaction on symmetrical airfoil

Calculations have been performed for Mach number, $M_\infty=0.724$, and incidence angles between $\alpha=0^\circ$ and $\alpha=4^\circ$. Figures 6 through 9 show the iso-Mach number contours near the lifting airfoils at different periods and various incidence angles. The contours have been obtained after stabilization. Each of these figures shows that during a period, small changes occur in the flow field, resulting in small oscillations in the flow field. A normal shock interacts with the boundary layer of the suction side of the blade. As shown in Fig. 9, increase in the incidence angle results in a shift in the location of the shock boundary layer interaction, towards the leading edge of the airfoil.

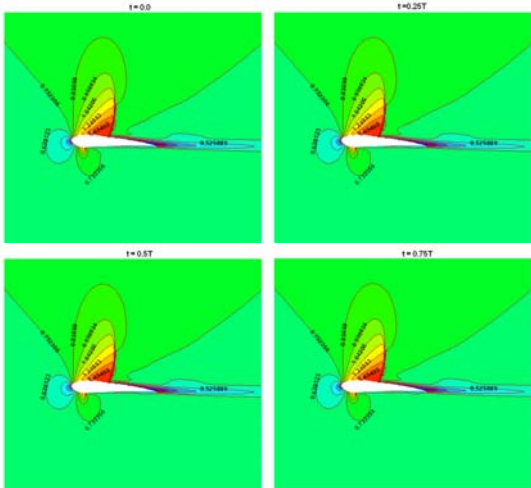


Fig.6 Mach number contours near lifting airfoil in transient flow, $M_\infty=0.724$, $\alpha = 0^\circ$

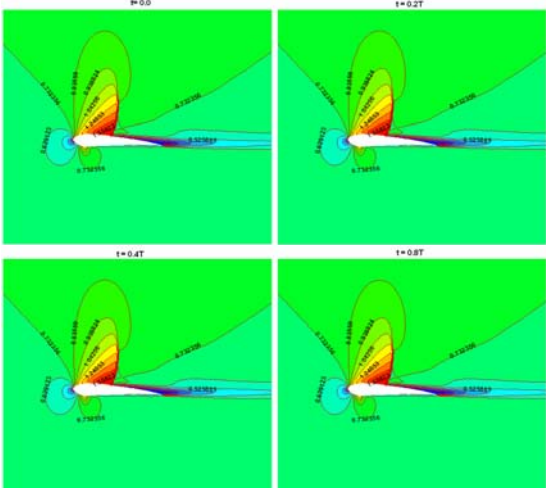


Fig.7 Mach number contours near lifting airfoil in transient flow, $M_\infty=0.724$, $\alpha = 1^\circ$

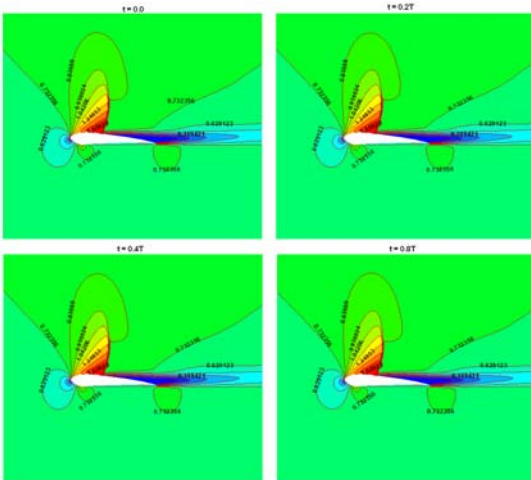


Fig.8 Mach number contours near lifting airfoil in transient flow, $M_\infty=0.724$, $\alpha = 3^\circ$

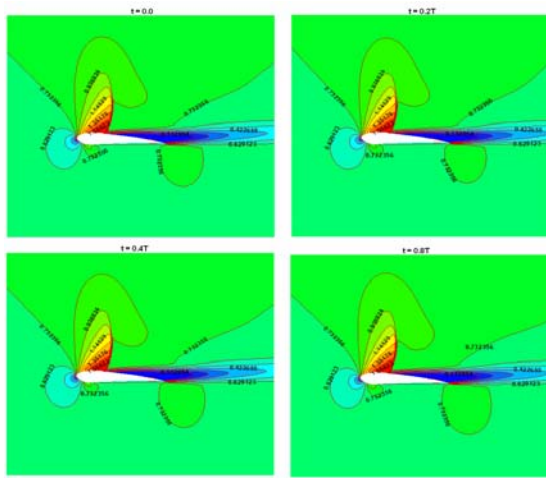


Fig.9 Mach number contours near lifting airfoil in transient flow, $M_\infty=0.724$, $\alpha = 4^\circ$

Transient pressure distributions, on both sides of the airfoil at various incidence angles, are shown in Figs. 10 through 13. As shown, the pressure distributions during a period change very slightly. Hence, it can be concluded that buffeting phenomena occurs in a very small region.

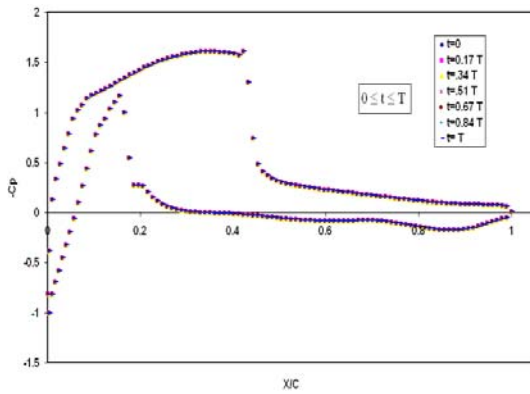


Fig.10 pressure coefficient on lifting airfoil in transient flow, $M_\infty=0.724$, $\alpha = 0^\circ$

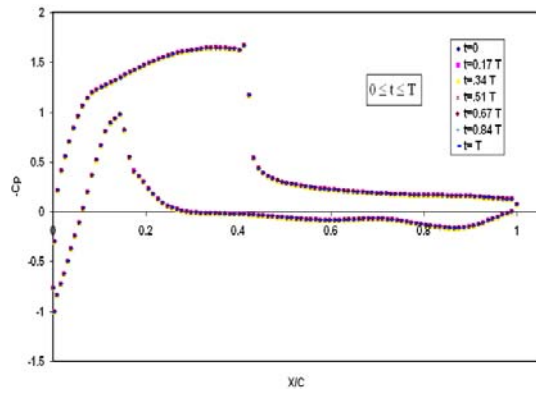


Fig.11 pressure coefficient on lifting airfoil in transient flow, $M_\infty=0.724$, $\alpha = 1^\circ$

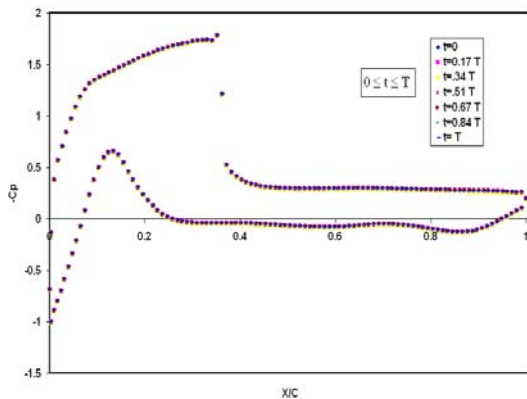


Fig.12 Pressure coefficient on lifting airfoil in transient flow, $M_\infty=0.724$, $\alpha = 3^\circ$

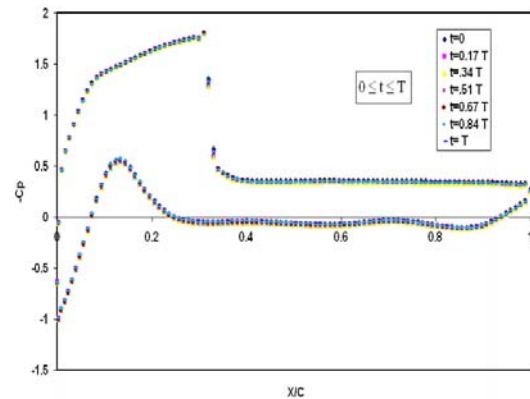


Fig.13 Pressure coefficient on lifting airfoil in transient flow, $M_\infty=0.724$, $\alpha = 4^\circ$

Time histories of lift coefficients at various incidence angles are shown in Figs. 14 through 17. The first part of all figures shows the airfoil subjected to high amplitude lifting forces. This amplitude gradually decreases, so that the lift coefficient approaches its steady value. These figures show that for low incidence angles, the transient lift coefficient approaches its steady value faster than for the case of high incidence angles.

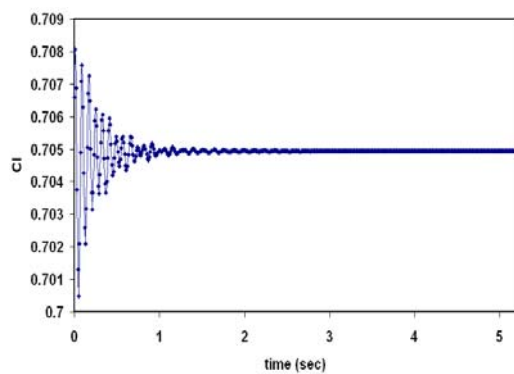


Fig.14 Time history of lift coefficient on lifting airfoil in transient flow, $M_\infty=0.724$, $\alpha = 0^\circ$

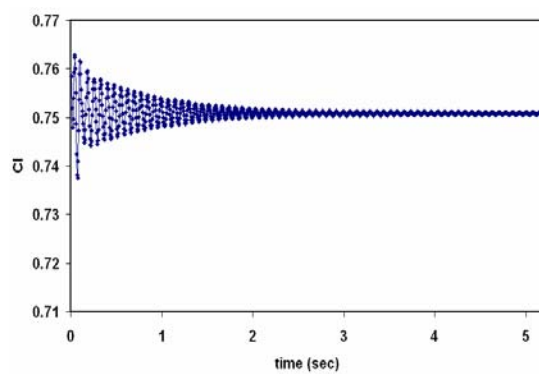


Fig.15 Time history of lift coefficient on lifting airfoil in transient flow, $M_\infty=0.724$, $\alpha = 1^\circ$

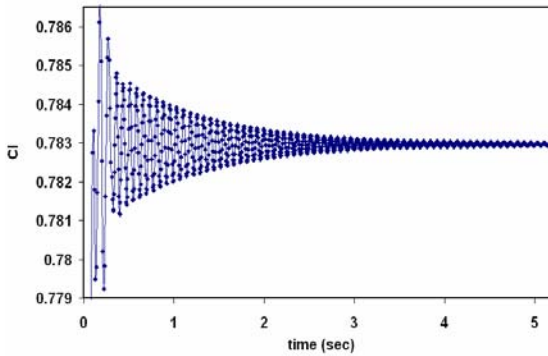


Fig.16 Time history of lift coefficient on lifting airfoil in transient flow, $M_{\infty}=0.724$, $\alpha = 3^{\circ}$

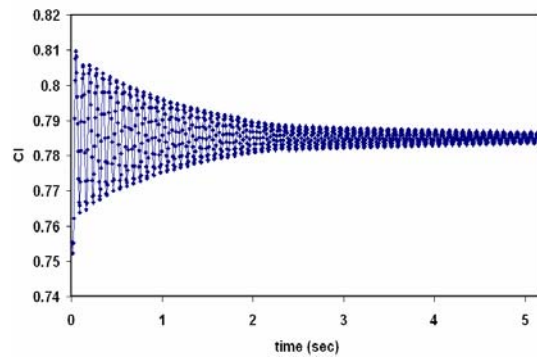


Fig.17 Time history of lift coefficient on lifting airfoil in transient flow, $M_{\infty}=0.724$, $\alpha = 4^{\circ}$

Figure 18 shows the oscillation frequency of the applied forces on the lifting airfoil. An increase in the angle of incidence from 0° to 1° initially results in an appreciable change in the oscillation of the applied forces. However, on further increase, this change becomes negligible.

Figure 19 shows the change in the location of boundary layer separation on the suction side of the lifting airfoil with change in leading edge angle. As shown, the location of boundary separation has moved closer to the front edge of the airfoil with increasing angle of incidence.

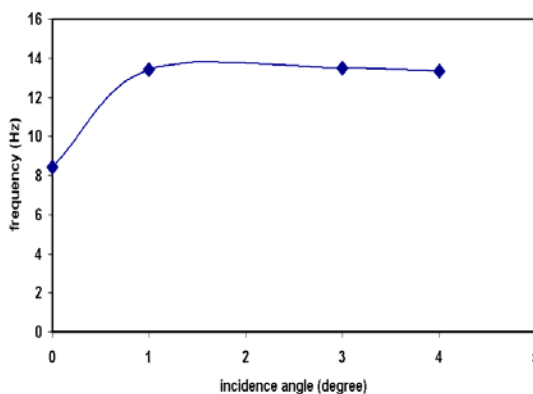


Fig.18 Frequency variation of lift coefficient with incidence angle (transient flow over lifting airfoil, $M_{\infty}=0.788$, $\alpha = 0^{\circ}$)

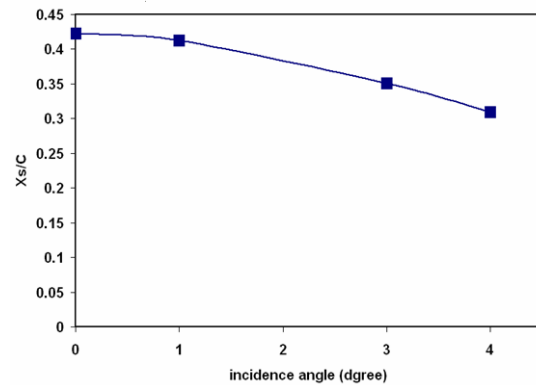


Fig.19 Time-average position of shock-boundary layer interaction on suction side of lifting airfoil (transient flow at different incidence angles, $M_{\infty}=0.788$)

5. CONCLUSIONS

- Numerical predictions show good agreement with experimental data.
- Interaction of shock wave and boundary layer results in separation of the boundary layer for all the cases considered in this study.
- During the interaction of shock wave and boundary layer on a symmetrical airfoil, the location, where separation of the boundary layer takes place, oscillates in a small domain and with a particular time period. Due to the airfoil symmetry, location of interaction of the shock wave and boundary layer and the boundary layer separation on both sides of the airfoil surface, lies at an equal distance from the airfoil leading edge.
- Interaction of shock wave and boundary layer in the direction of the suction side of the lifting airfoil, results in very rapid growth of the boundary layer and its ultimate separation.

- The increase in the incidence edge angle results in the interaction of the shock wave, and the boundary layer and its ultimate separation, at a smaller distance from the leading edge.

6. REFERENCES

- [1] Melnik, R.E., and Brook, J.W., The computation of Viscid/Inviscid Interaction on airfoils with separated flow, Proceed. 3rd Symp. Numerical and Physical Aspects of Aerodynamic Flows. Long Beach, T. Cebeci ed., Springer Verlag, 1986.
- [2] Carter, J.E., Edward, D.E., Davis, R.L., and Hafez, M.M., Analysis of Strongly Interacting Of viscid and inviscid Flows including separation, Proceed. 9th ICNMF, Saclay Lecture Notes in Physics, 218, Springer Verlag, 1985
- [3] Smith, F.T., Papageorgiou, D., and Elliot, J.W., An alternative approach to linear and nonlinear stability calculations at finite Reynolds numbers, *J. Fluid Mech.*, (1984).
- [4] Lock, R.C., and Firmin, M.C.P., Survey of techniques for estimating viscous effects in external aerodynamics, RAE Tech. Memo Aero 1900, 1981.
- [5] Veldman, A.E.P., New quasi simultaneous method to calculate interacting boundary layers”, *AIAA J.*, 19(1) (1981), pp.79-85.
- [6] Yoshihara, H., and Wai, J., “Transonic turbulent separation on swept wings – A return to direct formulation...”, AIAA paper No. 84-0265, Reno, 1985.
- [7] Cebeci, T., Clark, R.W., Chang, K.C., Halsey N.D., and Lee, K., Airfoil with separation and resulting wake, Proceed. 3rd Symp. Numerical and Physical Aspects of Aerodynamic Flows, Long Beach, T. Cebeci ed, Springer –Verlag, 1986.
- [8] André Bakker, Applied Computational Fluid Dynamics, Fluent.INC., 2006.
- [9] Le Belleur, J.C., Viscous-inviscid interaction for transonic separated Flows, Proceed. of ICASE workshop on Vortex Dominated Flows NASA Langly Field, USA, Springer Verlag, 1986.